New Methods for the Study of Intramolecular and Solvent Dynamics

Thesis by

Aseem Mehta

In Partial Fulfillment of the Requirements

for the Degree of

Doctor of Philosophy

California Institute of Technology

Pasadena, California

1997

(Submitted March 15, 1997)

Acknowledgements

After a very fruitful, personally and professionally, five years at Caltech that have, I believe, prepared me well for future challanges, I wish to thank a number of individuals without whom the Ph. D. experience would have been much less rewarding.

I have been enormously fortunate in having Prof. Rudy Marcus as research advisor. He has always been available for consultations and guidance. His penetrating physical insights, when I may have been liable to get lost in the minutiae of the calculations, have been invaluable. I believe that I will always carry with me his exhortations to focus on problems that have some real-life (experimental, in the academic context) relevance.

I immensely enjoyed my interactions with Prof. Alexei Stuchebrukhov on the IVR problem. He was a fount of knowledge and always willing to help and listen to the ramblings of a junior graduate student.

Dr. Xueyu Song has been a good friend, patiently listening to the (rare) gripes, and an enormously complementary research associate in solvation dynamics, always exhorting me to do the best. I will remember with pleasure our discussions on topics all and sundry.

Despite our being relative fermions (who did not occupy the same space at the same time), Bryan Hathorn has been a wonderful office-mate, always willing to lend his mathematical tools and always ready with novel ideas.

Other members of the Marcus group, including Prabha Sidharth, Chao-Ping Hsu and Shachi Gosavi have been most helpful and friendly. It has been my distinct pleasure to make their acquaintance.

Lastly, but most importantly, I wish to thank my grandmother and my parents for inculcating in me those values that have allowed me to succeed in my goals and for always giving me the freedom to follow my muse.

Abstract

Some of the fastest processes of relevance to chemical physicists occur on pico to femtosecond timescales. In the following chapters two of such fast processes are investigated with novel theoretical methods to obtain insight into experimental observations at the molecular level.

One of the major topics of interest in chemical physics has been about energy localization in polyatomic molecules. The "golden rule" formula states that the rate for the intramolecular relaxation of energy (IVR) that is initially localized in one part of the molecule is proportional to the density of states at that energy. Here, a general mechanism of the energy redistribution out of an initially populated "light" or "bright" state is elucidated. It is shown that, for a family of acetylenic molecules, the relaxation is due to a sequence of weak off-resonant directly coupled states rather than all the available states. This mechanism shows how the rates of IVR can be significantly slower than those predicted by a naïve application of the "golden rule," since mainly only the initial weak off-resonant couplings govern the rate of IVR.

Another topic that has attracted substantial interest in the chemical physics community is that of solvation. Various heavily applied theories of reaction rates, such as the electron transfer theory, have viewed the solvent as a dielectric continuum. Recent experiments and simulations have shown that the very fast solvation response provides interesting information on the molecular nature of the solvent. Here, a new method for doing molecular dynamics (MD) calculations for solvation is developed. This method uses the reaction field method to obtain the long range potential for a small cluster of molecules rather than using the usual Ewald sum technique with periodic boundary conditions (PBC). It is shown, here, that this method may be used successfully for solvent dynamics simulations. This method may prove superior for such calculations as compared to the PBC approach, since it does not impose an artificial isotropy on the problem as is the case with the PBC calculations.

Table Of Contents

Chapter 1

Vibrational Superexchange Mechanism of
Intramolecular Vibrational Relaxation in $(CH_3)_3CCCH$ Molecules
(Appeared in : J. Phys. Chem. **97**, 12491 (1993))

Reprinted from The Journal of Physical Chemistry, 1993, 97.

Vibrational Superexchange Mechanism of Intramolecular Vibrational Relaxation in $(CH_3)_3CCCH$ Molecules

A. A. Stuchebrukhov, A. Mehta, and R. A. Marcus*

Arthur Amos Noyes Laboratory of Chemical Physics,† 127-72, California Institute of Technology, Pasadena, California 91125

Received: June 24, 1993; In Final Form: August 17, 1993•

Quantum calculations are reported for the dynamics of intramolecular vibrational energy redistribution of the acetylenic CH stretch in $(CH_3)_3CCCH$ molecules. This paper is an extension of our previous publication (*J. Chem. Phys.* 1993, *98*, 6044) where the line widths of the CH overtone transitions were calculated in several molecules of a general class $(CX_3)_3YCCH$, and it was found that the relaxation is due to a sequence of many weak off-resonance vibrational transitions between tiers of directly coupled states. The coupling of the CH stretch to a manifold of quasi-resonant states resembles the superexchange mechanism of coupling between donor and acceptor states in long-distance electron-transfer reactions. An analysis based on total population in each tier is introduced. The very rapid decrease of this population in the intermediate tiers with tier index provides evidence that the relaxation dynamics occurs via tunneling (vibrational superexchange) under a dynamic barrier in the tier space of the system. Details of the time evolution of the population under the dynamic barrier in the course of relaxation are described. "Dead end" states, their effect on the time-evolution and on spectra, their removal via inclusion of additional anharmonicities, and, thereby, their probable artificial nature in the present case are discussed.

I. Introduction

In the previous paper[1] of this series, quantum calculations of homogeneous line widths of the acetylenic CH vibrational states in $(CX_3)_3YCCH$ molecules, where X = H, D and Y = C, Si, were reported. The line widths, which provide a measure of the rate of intramolecular vibrational relaxation (IVR), result from the vibrational coupling of the acetylenic CH stretch to the rest of the molecular vibrational degrees of freedom. The study was motivated by the recent experimental results of Scoles, Lehmann, and collaborators.[2,3] For these molecules extremely narrow vibrational lines, fwhm $\approx 10^{-1}$–10^{-2} cm^{-1}, have been observed. In the present paper the relaxation dynamics of the acetylenic CH stretch in $(CH_3)_3CCCH$ is explicitly studied in real time.

We summarize first some deductions of the previous study. In ref 1 it was found that the unusually slow relaxation (of the order of a hundred picoseconds), corresponding to the extremely narrow line widths in those molecules, is due to the absence of direct low-order Fermi resonances. Very high order resonances are available, but the direct coupling to such states was argued to play a negligible role: In those high-order quasi-resonant states many vibrational quanta of low-frequency modes are excited, and they can be qualitatively thought of as being separated a large distance from the light state in the state space, or classical action space, of the system. Instead of that direct coupling mechanism, the relaxation was assumed to occur in a sequence of many virtual transitions between tiers of directly coupled states, whereby the system uses the best "resonances" available, i.e., resonances typically with large detunings, to reach the final quasi-resonant states. These detuned, or virtual, resonances play the role of a bridge between the initially excited state and the quasi-continuum of well resonant states. The number of sequential virtual transitions required can be as large as 10 or more in this treatment.

Such a coupling scheme resembles the superexchange mechanism of the coupling of electronic states in long-distance electron transfer in biological systems.[4] For this reason it can be called vibrational superexchange. The very idea of superexchange as a mechanism of indirect quantum mechanical coupling is very general and has been discussed in the literature for a long time.[5] The difference between the usual electronic superexchange and vibrational superexchange is that in the former case the quasi-resonant electronic states of donor and acceptor, coupled indirectly via many virtual transitions, are separated by barriers in coordinate space while in the latter case the CH vibration and the quasi-resonant states, where many vibrational quanta of low frequency modes are excited, are separated in the action space, or in the zeroth-order quantum number space, of the system.

A tier of states is defined by the total number of quanta that each state in the tier differs from the light state, as described below. (The light state constitutes the $n = 0$ tier.) The population of the nth tier, $P_n(t)$, is a sum of the population of all states belonging to that tier. In many cases, the relaxation dynamics of the light state, the so-called survival probability, is studied.[6-8] This function can be most easily calculated and experimentally probed. In the present case such a strategy would correspond to the calculation of population of only the CH vibration, $P_0(t)$ in our notation. In addition to $P_0(t)$, the populations of other tiers $P_n(t)$, $n = 1, 2, \ldots$, are also studied in this paper. The population of each of the higher tiers provides, in fact, the main insight into the relaxation process. We consider not only how the relaxation of excitation of the CH stretch occurs but also how this excitation spreads over the other vibrational states in the molecule. Several authors in the past have recognized the importance of the analysis of the population of the dark states.[6,7,9-11]

Two limiting quantum mechanical forms of intramolecular vibrational relaxation (IVR) can be envisaged, using a zeroth-order basis set description: In one of these there would be a successive set of vibrational energy transfers, each governed by a kinetic expression, to near-resonant states, and so the overall transfer would be governed by a master equation. Any coherence would be completely lost at each step. In a second limiting mechanism the energy transfer would proceed from the initial zeroth-order state to a final near-continuum set of quasi-resonant states via a series of transitions over off-resonant states. These states are the virtual states mentioned above. This latter mechanism can appropriately be called vibrational superexchange, as noted above. In the present paper we describe results for the

† Contribution no. 8815.
• Abstract published in *Advance ACS Abstracts*, December 1, 1993.

0022-3654/93/2097-12491$04.00/0

IVR of the $(CH_3)_3CCCH$ molecule in which the acetylenic CH is prepared in its first excited vibrational state.

There are certain analogies to a classical, or really to a semiclassical description,[12,13] in that the off-resonant superexchange mechanism could correspond to a "dynamical tunneling": In the molecule, invariant tori in phase space are associated with the zeroth-order classical action variables and correspond semiclassically to the zeroth-order quantum states all in a many-dimensional, nearly parabolic energy well. If the introduction of the perturbation resulted only in the distortion of these tori but not their destruction, then extensive IVR could occur by a "dynamical tunneling" from one torus to the next, as described by Davis and Heller.[14] ("Tunneling" between tori has been extensively investigated, in one way or another, by a number of researchers since the early seventies.[15]) In an actual classical mechanical system with many coordinates, such as the present one, one can expect that the invariant tori will be at least partially ruptured and that another mechanism involving the chaotic-like passage through these fragments can occur classically and has been discussed by various authors.[16]

For this reason, we believe that the simplest quantitative description of the IVR process in these many-dimensional systems is the quantum mechanical one, though there will be an analogy between the vibrational superexchange mechanism and a tunneling between the zeroth-order invariant tori.

In the present paper the concept of tier population is introduced, converting the results of the many-coordinate IVR problem to a one-dimensional visualization. The presence of "dead-end" states, their effect, and their possible removal when higher order anharmonicities are introduced, are also discussed. A comparison is made with crude phenomenological descriptions of the successive incoherent steps mechanism and of the vibrational superexchange mechanism, using the long-time behavior.

The structure of the paper is as follows. In section II some theoretical aspects of the tier model are discussed and in section III dynamics of the tier system of $(CH_3)_3CCCH$ molecule is studied. In section IV, the results are discussed.

II. Tier Model

Statistical IVR is usually understood as the relaxation of the state that is directly accessible from the ground state through a transition moment, the "light state", into a large number of anharmonically coupled "dark" states which are inaccessible from the ground state. This coupling arises from the deviation of the potential surface, written in normal mode or normal mode/local mode coordinates,[17] from harmonic behavior. A refinement of this model divides the dark states into various tiers.[1] Each state in a given (nth) tier is coupled through third-order anharmonic couplings to states in the $n-1$ or $n+1$ tiers. If fourth-order couplings are being taken into consideration, then the states in the nth tier are coupled to states in the $n-2$ and $n+2$ tiers. Once the light state is specified, the tiers are then created sequentially. The cubic (or quartic) anharmonicity operator is written in terms of creation and annihilation operators which act on the light state to generate the first tier, on the first tier to generate the second tier and so on until some specified criterion (usually, the number of states) is met. Care is taken to avoid duplication of states in different tiers in this scheme, a scheme which is implemented naturally in C language with dynamic memory management and the use of pointers.[1] The first six tiers for $(CH_3)_3CCCH$, generated in this way with a model potential anharmonic field developed in ref 1, are shown in Figure 1.

Once the tier structure is complete then the complete $N \times N$ vibrational Hamiltonian is formed within this basis set and analyzed. The Hamiltonian is diagonalized using the standard algorithms for complete diagonalization of large, sparse symmetric matrices. Upon diagonalization the eigenvectors are normalized. This procedure of exact and complete diagonalization has a built-in limitation on the size of the matrix. For example, with access

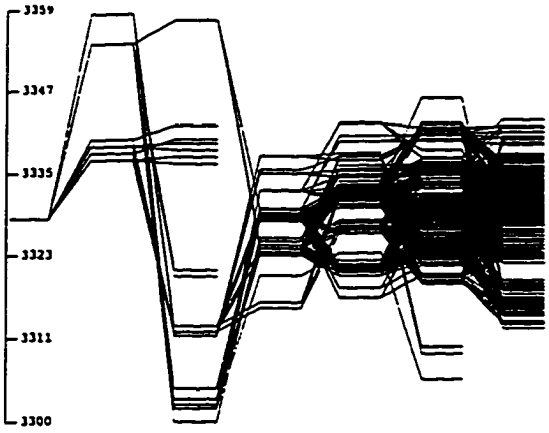

Figure 1. First six tiers of sequentially coupled zero-order states in $(CH_3)_3CCCH$. The first state on the left is the acetylenic CH vibration $v = 1$.

to 10 Mwords = 80 Mb of memory on our computer, memory constraints limit the dimension of the matrix to ≈2000. Use of Lanczos-type ideas for diagonalization may be useful in dealing with larger matrices. Further details on the generation of the tier structure and the associated computational details are given in the previous paper in this series.[1]

Having calculated the eigenvalues, E_i, and the eigenvectors, $|\psi_i\rangle$, it is possible to perform the dynamics calculations on all the zeroth-order states. The transition intensities of different lines in the absorption spectra can also be obtained. The spectrum shows how the single line of the transition to the light state splits into a broadened band of transitions in the presence of the anharmonically coupled dark states. The absorption spectrum is related to the amplitude of survival probability of the light state ($|\phi_0\rangle$), which is defined as

$$p_0(t) = |\langle\phi_0|\phi(t)\rangle|^2 = |\langle\phi_0|e^{-iHt}|\phi_0\rangle|^2 \qquad (1)$$

where $|\phi(t)\rangle$ is the state evolving in time from the prepared state $|\phi_0\rangle$. The Fourier transform of $\langle\phi_0|\phi(t)\rangle$ is given by

$$I(\omega) = (1/2\pi)\int_{-\infty}^{\infty}\langle\phi_0|\phi(t)\rangle e^{-i\omega t}\,dt \qquad (2)$$

Here, $I(\omega)$ is proportional to the actual absorption spectral lineshape, as defined in ref 18. One factor in the proportionality constant is the square of the dipole transition moment. Inserting the resolution of the identity

$$1 = \sum_{i=1}^{N}|\psi_i\rangle\langle\psi_i| \qquad (3)$$

(the $\{\psi_i\}$ form a complete set of orthonormal eigenvectors within this basis) and using $\hat{H}|\psi_i\rangle = E_i|\psi_i\rangle$, we have

$$p_0(t) = |\sum_{i=1}^{N}|\langle\phi_0|\psi_i\rangle|^2 e^{-iE_it}|^2 \qquad (4)$$

$$I(\omega) = \sum_i |\langle\phi_0|\psi_i\rangle|^2\delta(\omega - E_i) \qquad (5)$$

Similarly, the population of any other zeroth-order state ϕ_j is given by

$$p_j(t) = |\langle\phi_j|\phi(t)\rangle|^2 = |\langle\phi_j|e^{-iHt}|\phi_0\rangle|^2 = |\sum_{i=1}^{N}\langle\phi_j|\psi_i\rangle\langle\psi_i|\phi_0\rangle e^{-iE_it}|^2 \qquad (6)$$

To obtain insight into the mechanism of IVR the actual dynamics of each of the invidual zeroth-order states has been calculated.

Since the total number of states is so large, a global picture of the dynamical behavior of the molecule was obtained from the dynamical behavior of each state by calculating the total population in a given tier as a function of time:

$$P_n(t) = \sum_{k=1}^{N_n} p_k \qquad (7)$$

where N_n is the number of states in the nth tier and the $\{|\phi_k\rangle\}$ belong to the nth tier. P_n is the total population in the nth tier. In the zeroth-tier there is only one state, the light state, making $p_0(t) = P_0(t)$. With these tools available for the analysis, the dynamical behavior of the tier model can be examined in detail.

III. Dynamics of the Tier System

3.1. Reduced Dynamics with a Quasi-continuum Tier. The detailed analysis of the relaxation mechanism in $(CH_3)_3CCCH$ is presented next. For this molecule a total of about 30 000 states, sequentially coupled to the light state, were identified in an artificial intelligence search procedure using a perturbation theory based criterion.[1] Only those states that are expected to contribute significantly to the relaxation process are included in the calculation. The first six tiers of this system are shown in Figure 1. The whole structure contains detailed information about the relaxation pathways.

To study the dynamics of such a huge system some simplification has been adopted, because the total system cannot be diagonalized exactly. For this reason, only 10 tiers of the real system which contain 624 states are included in the present calculation. Then, to stimulate the presence of the quasi-continuum of other states in the later (>10) tiers and yet to stay within the limits of possible complete diagonalization, an eleventh tier is added within a narrow resonant energy window taking the total number of states to 2000, the energy of each state in the eleventh tier being random within a prescribed window. This number is the maximum number of states that can be diagonalized directly in the computer being used, due to memory constraints.

This eleventh tier phenomenologically describes the prediagonalized states from all the actual tiers with numbers $n > 10$. The energy window for this, the eleventh, tier was chosen to be 0.5 cm^{-1} around the major peak in the spectrum of the 10-tier system. This major peak is slightly shifted from the energy of the light state due to its interaction with the other states. The additional states in the eleventh tier are coupled randomly with states in the tenth tier. The matrix elements between states in tier 10 and tier 11 form a Gaussian distribution centered at the energy of the main eigenstate of the 10-tier system, such that any edge effects from the additional tier may be minimized. The density in the eleventh tier was chosen in such a way as to make the total density of states roughly equal to the total density of dark states for the fundamental transition of the CH stretch in the 42-dimensional oscillator model described in detail in ref 1. Although it is reasonable to expect that this last tier may impose some artifacts on the dynamics, we believe from the results below that this simplified approach, where a light state is coupled through intermediate tiers to a quasi-continuum of states, provides a realistic model of the process of IVR in $(CH_3)_3CCCH$. Before considering the details of the mechanism, it is useful to comment on the effect of the addition of this eleventh quasi-continuum tier on the dynamics and spectra.

In Figure 2 the population dynamics of the light state $p_0(t)$, i.e., the survival probability, is shown with and without the quasi-continuum (eleventh) tier. It is seen that while the initial (≤200 ps) relaxation of the light state is identical for the two systems, recurrences of population for the light state are present for the 10-tier system. This observation shows that during the decay in the first 200ps the higher tiers of states are irrelevant and, therefore, the initial decay is completely a local phenomenon. The same conclusion can be reached from the sum rule for the

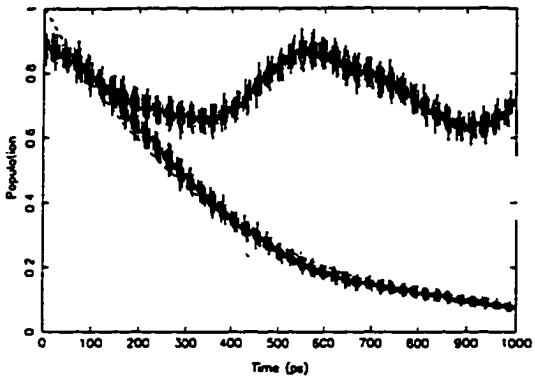

Figure 2. Top curve: survival probability of the acetylenic CH stretch in the 10-tier system without the addition of a tier to simulate the presence of a quasi-continuum. Bottom curve: survival probability of the acetylenic CH stretch when the quasi-continuum tier is present. Dashed line is the least-squares exponential fit to the bottom curve.

width of the absorption spectrum.[1] This width is the inverse relaxation time for the short-time behavior.

The addition of the eleventh tier, however, changes the long-time behavior of the survival probability, significantly curtailing the long-time recurrences (Figure 2). After some initial transient behavior, the decay of the light state is exponential, as expected in a statistical limit. That $P_0(t)$ in the two curves does not *appear* to approach 1.0 as $t \to 0$ reflects a very rapid (almost instantaneous on our time scale) dilution of the light state by far off resonant interactions. Thus, we conclude that the presence of the quasi-continuum tier is essential and that more than 10 tiers are needed to describe the irreversible decay of the CH stretch.

Similar dramatic effects are observed in the absorption spectra when the quasi-continuum tier is added. For the 10-tier system, i.e., for the system without a quasi-continuum, the spectrum is shown in Figure 3a. It essentially consists of one major peak. The addition of the 11th tier with a high density of resonant states produces an effect shown in Figure 3b. It is seen that a broad distribution of peaks is formed with about the same full width at half maximum as predicted by the Golden Rule.[1] Since the statistical decay of the population requires the presence of a high density of well resonant states, the addition of this last tier is absolutely essential.

While the addition of the eleventh (quasi-continuum) tier has transformed the spectrum from a few separated eigenstates into a well-defined band of absorption lines, the density of lines in the spectrum is still smaller than its actual value in real molecule. In our multidimensional oscillator model we have not taken into account the possibility of methyl groups tunneling between equivalent torsional positions. The tunneling events transform the C_{3v} point-group symmetry of our oscillator model into G_{162} molecular symmetry group,[19] significantly increasing the number of possible anharmonic couplings of the light state to the dark states. This effect was argued to increase the density of actual spectral lines: possibly by a factor[2,3] as large as 24.

To see what can happen with the spectrum if the density of available dark states is increased further from its present value in the quasi-continuum tier, model calculations were performed. In these calculations a single light state is randomly coupled to a tier with density of states 705 and 20000/cm^{-1}, respectively. The former density corresponds to our oscillator model while the latter corresponds to the breaking down of the C_{3v} symmetry. The spectrum of such a model system is shown in Figure 4. The absolute energy position of the light state is not critical in this model calculation. As the density of states (ρ) is increased while ρb^2 is kept constant (b^2 is the mean square matrix element), the spectrum is transformed from a series of disconnected peaks into a Lorentzian. In Figure 4, $\Gamma = 2\pi\rho b^2$ is kept constant and the

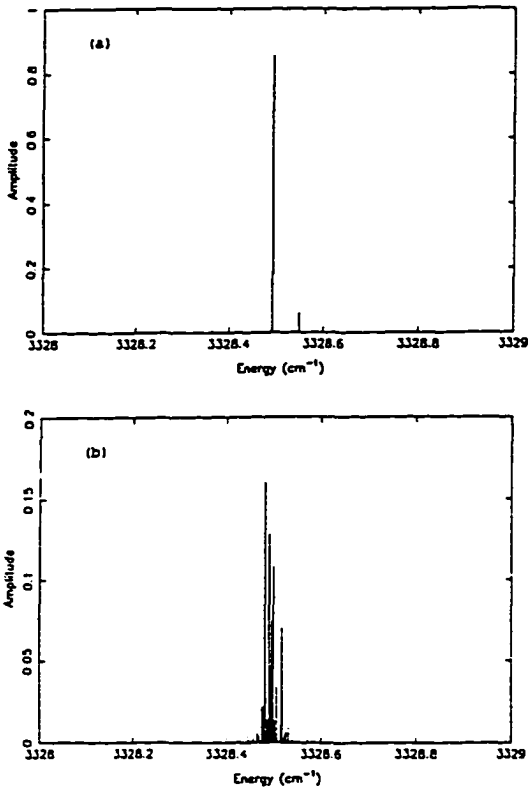

Figure 3. Absorption spectra corresponding to the (a) 10- and (b) 11-tier systems that simulate the acetylenic CH stretch in $(CH_3)_3CCCH$.

simulated curve is compared to an idealized curve of Lorentzian shape with this Γ, this idealized curve being given by

$$I(\omega) = \frac{1}{\pi} \frac{\Gamma/2}{(\omega - \omega_0)^2 + (\Gamma/2)^2} \qquad (8)$$

where $I(\omega)$ is the spectral absorption lineshape.

Thus, we infer that the spectrum of our model, Figure 3b, will continuously evolve into the Lorentzian envelope, observed experimentally, when the density of states in the quasi-continuum tier reaches its actual value and when account is taken of the possible experimental broadening of each individual eigenstate. Once the statistical limit is reached, any further increase in the density of states simply fills in the remaining spaces within the individual eigenstates.

We focus next on the characteristics of the dynamics of populations of tiers with tier numbers $n \geq 1$, i.e., on the dynamics of the accumulating population of states other than the light state.

3.2. Long-Time Dynamics of the Tier System. Dead-End States. The main qualitative feature of the dynamics of the tier system on the time-scale of decay of the light state is shown in Figures 5 and 6. For each tier n we again are interested in the evolution of the population of the whole tier, P_n. The time evolution of P_n shows that the population of the intermediate tiers is always very small (<0.1, Figure 5), never building up significantly. At the same time, the population of the light state decays (Figure 2) and the population of the eleventh, or quasi-continuum tier rises, apparently as a result of this decay (Figure 6). Qualitatively, it appears as if the population flows directly to the distant eleventh tier, largely bypassing the intermediate tiers. This type of behavior is typical for a superexchange mechanism. There is also an analogy to a tunneling dynamics which we discuss in the later sections in the paper.

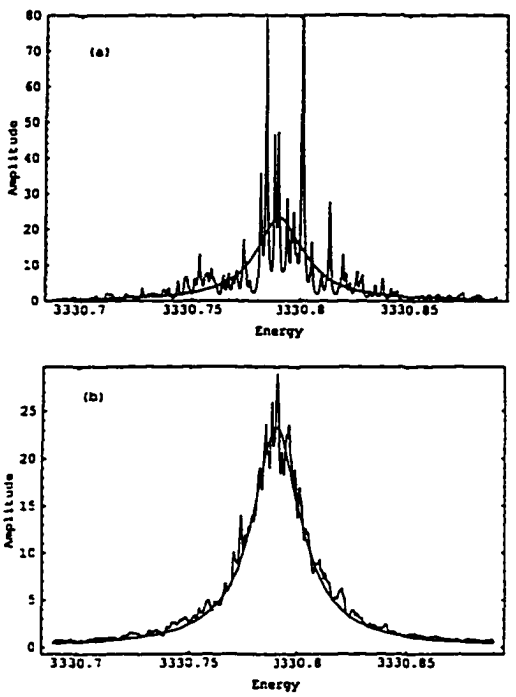

Figure 4. Spectrum of a light state *directly* coupled to a dense manifold (density = ρ) of dark states: (a) $\rho = 705/cm^{-1}$; (b) $\rho = 20000/cm^{-1}$.

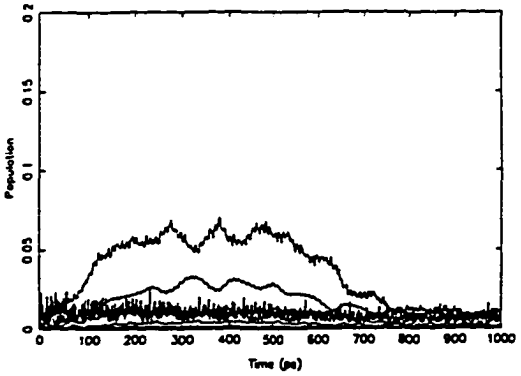

Figure 5. Population of tiers 3–10 as a function of time in the presence of the eleventh tier. The top curve is tier 5, the next is tier 9, a cluster of tiers 3, 4, and 7 are next, tier 8 is next, and a pair of tiers 6 and 10 are lowest.

The off-resonant states are virtual states, and for this reason preclude a buildup of population within the intermediate tiers (Figure 5). However, some buildup of the population is possible if by accident there is a good resonant state in a distant tier and that state is not coupled by cubic terms to further tiers in the system. We call such states dead-end resonant states. Such states are of a somewhat artificial nature, because there are always higher order anharmonic couplings. However, in calculations with a model anharmonic field, like the present one, after selecting states with an artifcial intelligence search procedure in the tier system and using only third-order anharmonicities there can be such states as described above. Their effect is considered next.

It has been noticed that there are several such dead-end states in our tier system. Of such states, only two states in the third tier were found to have a significant effect on dynamics and spectra. One of these states is more resonant with the position of the absorption band than the other one and, therefore, has a

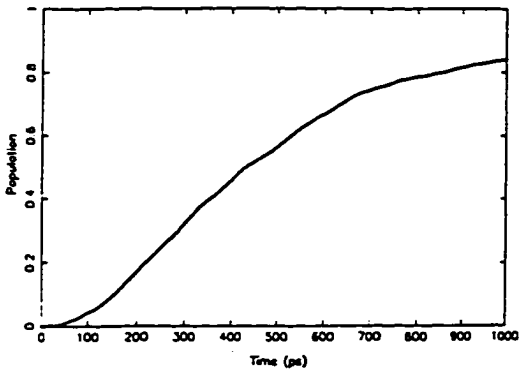

Figure 6. Time-evolution of the quasi-continuum tier in $(CH_3)_3CCCH$.

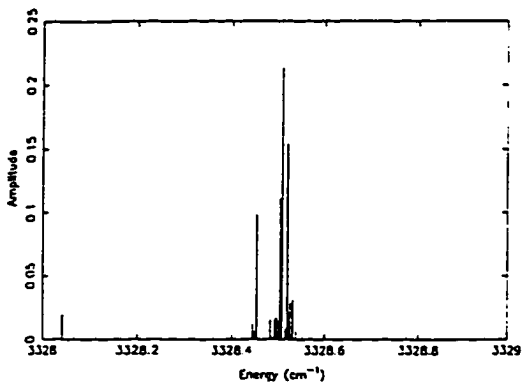

Figure 7. Spectrum when the dead-end states are added. Compare with Figure 3b.

larger effect. We also noticed (calculations given below) that the effect of these two states is considerably reduced when small quartic terms coupling them to further $(n+2)$ tiers are introduced. Because of their artificial nature, these states have been removed from the calculations described in section 3.1. In the absence of further couplings, the removal of the dead-end states does not effect the overall IVR process dramatically, especially on a long-time scale. The calculations have also been performed in a system where such resonant dead-end states are present. These calculations are described next.

In Figure 7 the spectrum of the system with resonant dead-end states is shown. Comparison with Figure 3b shows that the dead-end states produce additional components in the spectrum. These separate peaks are due to the absence of couplings of the dead-end states to states in further tiers. The overall dynamics of the tier system, however, does not change qualitatively when the dead-end states are present. The dynamics of the light state and the quasi-continuum tier are shown in Figure 8. As a result of a single strong resonance in the third tier, in the time evolution of the light state there is a tendency now for a coherent quantum beat to occur. There also exist fast oscillations of smaller amplitude due to the off-resonant dead-end state.

In Figure 9 the population of the third tier and the population of the resonant dead-end state is shown. It is seen that practically all the population of the tier is due to a single state. The population of the third tier is in this case significantly larger than the population in other tiers of the system because of the direct resonance.

The nearly resonant state in the third tier is not coupled further via cubic terms in the Hamiltonian, as we have already noted. Its removal does not affect the overall dynamics significantly, but it does destroy the coherence between the light state and the third tier as seen from the comparison of Figures 2 and 8. A

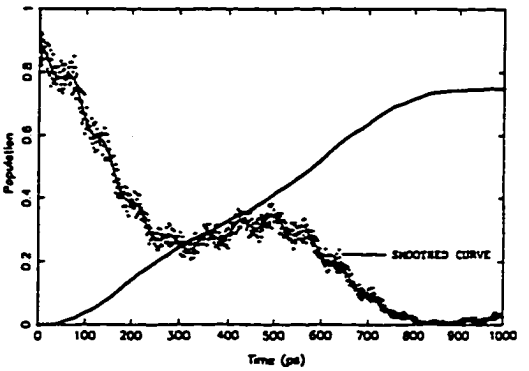

Figure 8. Survival probability (of light state) and the dynamics of the quasi-continuum tier when the two dead-end states are included. Compare with Figures 2 and 6.

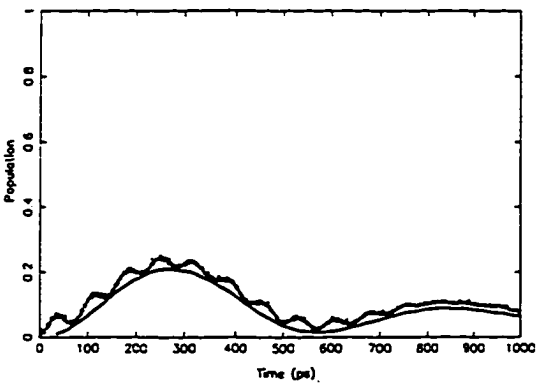

Figure 9. Dynamics of the third tier (upper curve) and the nearly resonant dead-end state (lower curve).

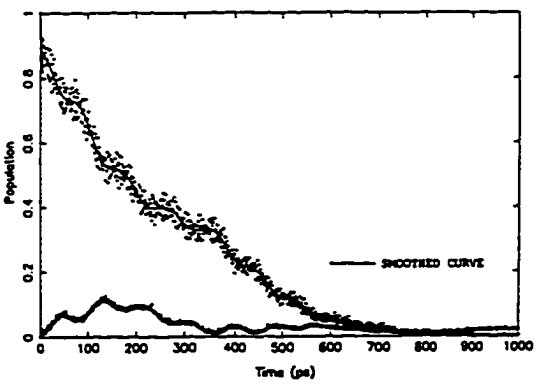

Figure 10. Survival probability of the light state (upper curve) and the dynamics of the third tier (lower curve) when the dead-end states are further coupled through quartic anharmonicities.

similar effect to this actual removal of the dead-end states can be achieved by adding higher anharmonic couplings (quartic and quintic) that have not been taken into account. To gauge the effect of additional higher order couplings, the two dead-end states (in the third tier) were coupled to a few states in the fifth tier with a quartic matrix element of 0.5 cm^{-1}. The result is shown in Figure 10. The quantum beat behavior is significantly reduced, the coherence being destroyed by the further coupling of these two (one of them nearly resonant) dead-end states. It is, therefore, reasonable to anticipate on this basis that the states which are not coupled to further tiers by cubic terms and act in a beatlike manner with the light state will often not show such

TABLE I: Average Matrix Element β, Density of States ρ and Window Size for Each Tier of the Model System (Total States = 2024)

tier	window, cm^{-1}	ρ	β, cm^{-1}	tier	window, cm^{-1}	ρ	β, cm^{-1}
1	0.2	10	0.03	6	0.2	270	0.07
2	0.2	25	0.04	7	0.2	470	0.07
3	0.2	90	0.05	8	0.2	740	0.07
4	0.2	140	0.06	9	0.2	1395	0.07
5	0.2	200	0.06	10	0.2	6775	0.07

behavior when higher-order couplings are taken into account. This result also points out that our calculations reflect accurately the gross features of the IVR dynamics and that they may contain artificial details which are sensitive to the individual positions, couplings of the states and their matrix elements in the model. Such is the case when an apparent dead-end state, arbitrarily uncoupled to further tiers, is present. The Lorentzian nature of the experimentally observed spectrum[2] shows the absence of such states in the actual molecule. It should be noted that in smaller molecules where there is no statistical decay, onset of IVR is denoted by splittings of individual J, K peaks and presence of quentum beats in the dynamics.

3.3. Short-Time Dynamics of Intermediate Tiers. In the tier system of the $(CH_3)_3CCCH$ molecule the population of the intermediate tiers is extremely small during the relaxation process. However, those tiers provide the bridge for the population flow from the light state into the quasi-continuum of states in higher tiers. A closer examination of the dynamics of tiers reveals that the population in tiers shows an intriguing behavior at short times, providing an interesting detail of the relaxation process.

To explore further some details of the dynamics of intermediate tiers, calculations were performed on a model tier system. In this system the coupling to the light state as well as the number of states in the intermediate tiers were increased in order to make population of the intermediate tiers somewhat larger and less "noisy". Otherwise this model system qualitatively resembled the real one whose tier structure is shown in Figure 1. The population of each intermediate tier was still sufficiently small to correspond to the superexchange type of coupling rather than the overlapped resonances case: The population of tiers 2–9 never exceeded 0.2. Also, for each intermediate tier, the product of β, the average coupling matrix element between successive tiers, and ρ_{eff}, the effective density of directly coupled states, was smaller than unity (≈0.5). In other words, the average detuning of two coupled states was larger than the coupling matrix element. These facts confirm that the relaxation mechanism corresponds to the superexchange type of coupling behavior. The exact parameters of the model system are given in Table I.

The short-time dynamics of the first four tiers of this model system is shown in Figure 11. It is seen that at short times the population displays an interesting threshold behavior. The same kind of behavior is common to all intermediate tiers. For any given tier n, the population remains near zero before suddenly increasing. This time, when the front of the population distribution reaches tier n is denoted by t_c^n. In Figure 12 the initial population evolution for the first eight tiers is shown in greater detail. Figure 12 shows that the population distribution front moves with constant velocity along the tier coordinate. In other words, t_c^n increases linearly with tier number n, Figure 13. It may be surmised that for some initial time the bulk of the population remains localized in the initial tiers while a small portion leaks out into the intermediate tiers. The distribution function of the population in the initial stage of relaxation, when the population of the light state has not decayed significantly, develops a very thin tail in the region of the intermediate tiers. At short times this tail has a sharp front that moves with constant velocity and appears as a threshold when the dynamics of each tier is analyzed. Statistical decay occurs once this front reaches the quasi-continuum. The population then leaks from the light state into the quasi-continuum through the formed "tunnel" with a near steady state population in each intermediate tier at some intermediate times. Of course, once the population of the bright state has decayed the population in the intermediate tiers will decrease also.

Addition of fourth-order anharmonicities may scramble the constant velocity of the sharp transition, but we may still expect a residual effect. Within the model systems it was also observed that the initial tiers become saturated very soon and for this reason probably have a different velocity than the intermediate and later tiers (Figure 13).

3.4. Superexchange or Overlapping Resonances? In principle two different limiting mechanisms could be envisaged for the dynamics of the energy flow through the sequence of tiers. In one of these there would be a successive set of real vibrational energy transfers—from the light state to the first tier, from first tier to the second one, and so forth until the quasi-continuum tier is reached. The overall transfer would be governed by a kinetic master equation. In this scheme the coherence is lost in each step of energy transfer. This type of IVR occurs when in a classical description, there is a sequence of many overlapping resonances, as described in a series of papers by Sibert et al.[20]

In the second type of mechanism the energy transfer would proceed from the initial state to a final near-continuum set of quasi-resonant states via a series of off-resonant transitions, with no classical overlap. This mechanism does not require a sequence of classical overlapping resonances between the light state and other states in the molecule. The intermediate off-resonance states can be only weakly coupled to a light state. This latter mechanism corresponds to superexchange.

Rigorously speaking, from the smallness of the population of the intermediate tiers one cannot distinguish between the two IVR schemes described above. Thus, although the low population in the intermediate tiers suggests that the energy transfer might be due to superexchange, the kinetic type of equations could, in principle, give a very low population distribution in the intermediate tiers. This situation can happen, for example, due to a high rate of energy transfer into quasi-continuum tier from the previous one and a small rate of transfer from the light state into the first tier. One can, however, distinguish between the two mechanisms in a different way, considered next.

To distinguish between the mechanisms and then to establish that the relaxation dynamics in the intermediate tiers indeed corresponds to a coherent superexchange mechanism, as opposed to a possible incoherent kinetic type of transitions between tiers, the quasi-stationary population (at $t = 1000$ ps) of the intermediate tiers is compared in Figure 14 with density of states in the tiers. (The calculation is for the "real" system rather than the model system that was employed to determine the transient behavior in section 3.3.) If the dynamics in the intermediate tiers were governed by a kinetic type of equation, the quasi-stationary population in each of the tiers would be approximately proportional to the density of states in that tier, and so would increase with tier index. Instead, as is seen from Figure 14, the quasi-stationary population decreases with tier number, as if there were a barrier separating the light state from quasi-resonant states in the distant tiers (Appendix).

From Figure 14 it is clear that, apart from some local fluctuations, the population decreases significantly with tier number. Also, (not shown) the population ratio P_l/P_{11} is continually decreasing for each tier with time. The marked decrease of population with tier number reinforces our belief that the overall mechanism of relaxation is tunnelling-like and not kinetic. If the kinetic behavior was being followed, then the population distribution should have paralleled that of the density of states and so would have increased with tier number.

IV. Discussion

The tier system of the $(CH_3)_3CCCH$ molecule shows an interesting dynamical behavior. The population in the intermediate tiers never builds up significantly, and the population

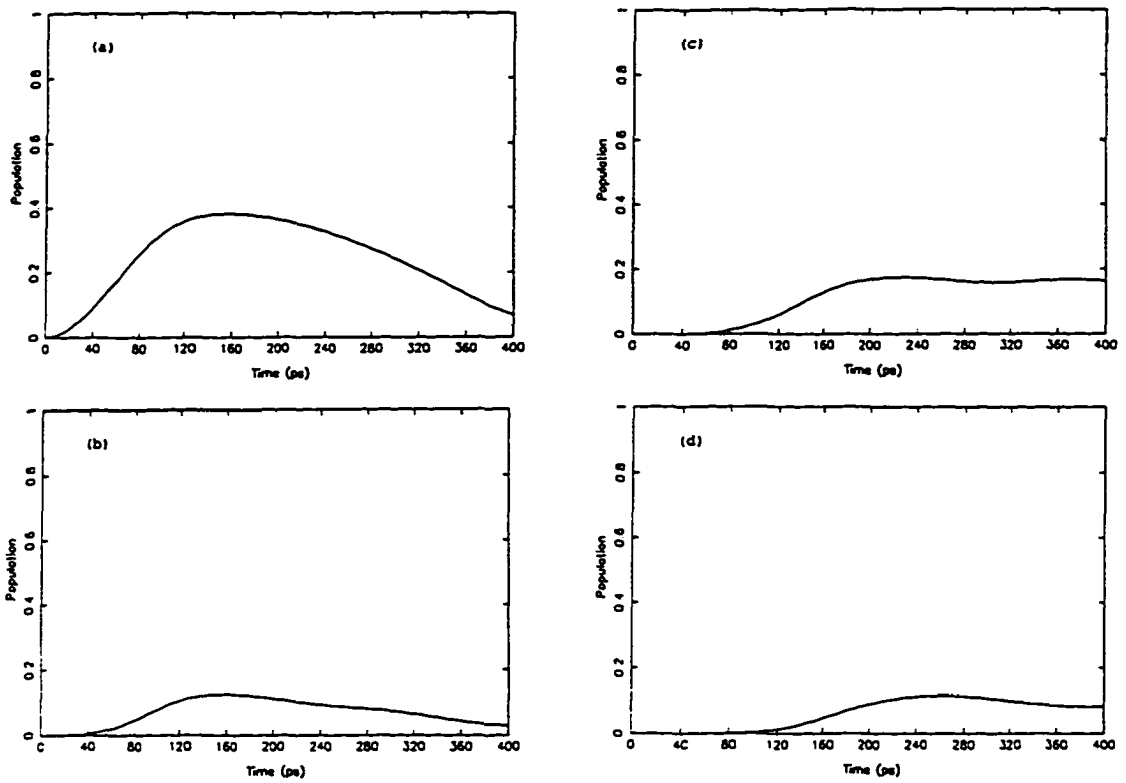

Figure 11. Population dynamics of first four tiers in a model system showing the threshold behavior: (a) first tier; (b) second tier; (c) third tier; (d) fourth tier. See text for details about the model system.

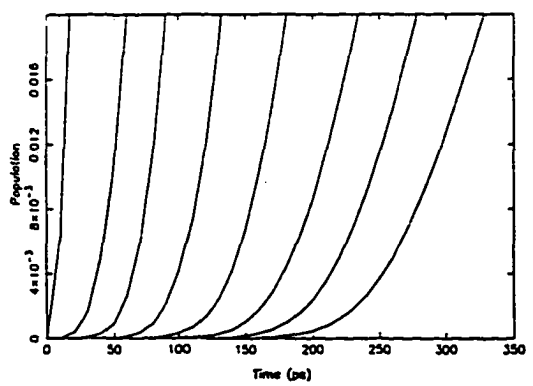

Figure 12. Short-time threshold behavior of first eight tiers of model system.

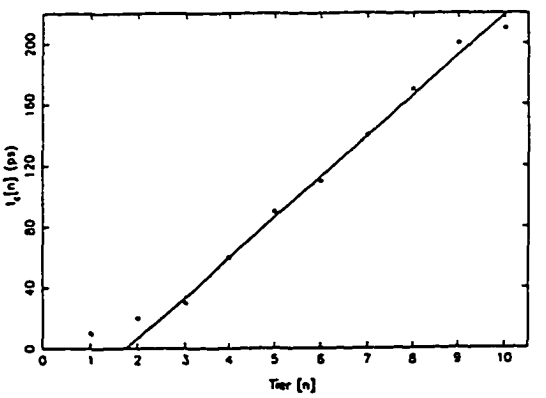

Figure 13. Threshold t_c^* as a linear function of tier number (n).

from the light state flows directly into a quasi-continuum tier, largely bypassing the intermediate tiers. The mechanism of the transfer was established to be a coherent superexchange. If the probability of finding a real particle at some discrete points along the coordinate axis was being calculated (those points correspond to the tier numbers n), this type of behavior (small and approximately exponentially decreasing population with the coordinate) could correspond to tunneling along the given coordinate axis. Hence, it can be said that the type of relaxation in our system is tunneling (or tunneling-like) along the tier coordinate.

It is relevant to comment on this behavior and to justify its being termed tunneling. This tunneling is not tunneling in its usual sense where the particle tunnels through a real potential energy barrier in coordinate space. The potential energy function for our system is a multidimensional anharmonically distorted parabola, and there are no potential barriers separating different regions of the configuration space. The light state is, however, separated from the quasi-continuum of resonant states, in which the population ultimately flows, by many intermediate states which are well off-resonance. These states sequentially couple the light state and the quasi-continuum states.

This situation is much the same as in a superexchange model of the long distance electron transfer problem. The off-resonant states are the best resonances available in a given order of interaction (on the average, the frequency mismatch is much larger than the coupling). In classical mechanics those resonances cannot be used directly, and so the population can be locked into the initial CH state. One can say, hence, that the intermediate off-resonant states create a dynamical barrier for decay of the

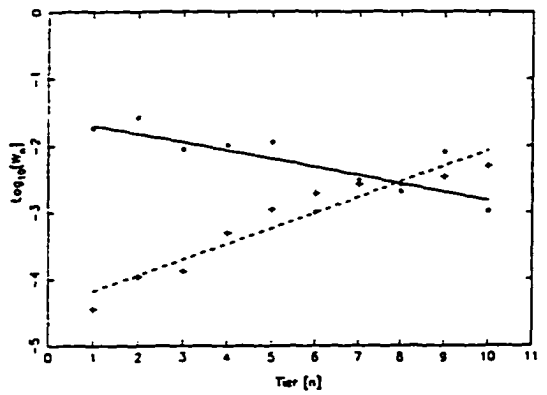

Figure 14. Quasi-stationary populations (circles) and density of states (crosses) in intermediate tiers. Exponential approximation (linear curves in log scale) are shown by a solid and broken line, respectively. For the upper curve, $W_n = P_i/P_{11}$ where P_i is the population of the ith tier and for the lower curve $W_n = \rho_i/\rho_{11}$, where ρ_i is the density of states in the ith tier.

CH vibration, even though there is no potential energy barrier. In the actual quantum system the population flows through this barrier in much the same way as usual quantum mechanical particle tunnels through the potential barrier. Thus, the tunneling occurs in our case under a dynamical barrier along the tier coordinate of the system. The connection of the superexchange type of vibrational coupling to dynamic tunneling has been recently discussed in detail by two of the present authors.[21] There are several examples of low-dimensional systems where this type of tunneling occurs. Perhaps, the two best examples of this phenomenon are the asymmetry doublet in the rotational spectra of the asymmetric tops[22] and doublets in the vibrational spectra of water (ref 21 and references therein). It should be added that the picture of tunneling between the invariant tori referred to earlier is only a rough approximation in these many-coordinate systems, since, as noted earlier, the tori are expected to be largely ruptured and other more complex modes of transfer[16] would then occur.

To understand the nature of the tier coordinate, it is useful to compare the results of our quantum calculation with what might be the classical or semiclassical analog of it. Action space is the most convenient representation for the relaxation dynamics in classical and semiclassical analysis. Each of the zeroth-order states of $(CH_3)_3CCCH$ molecule is characterized by $3N - 6 = 42$ vibrational quantum numbers, $|v_1, v_2, ..., v_{42}\rangle$. For example, the light state CH with $v = 1$ is $|1, 0, ..., 0\rangle$. In the semiclassical analysis these quantum numbers correspond to zeroth-order actions divided by Planck's constant. Thus, each of the zeroth-order states is represented by a point in the 42-dimensional action space of the molecule $(I_1, I_2, ..., I_{42})$. In the classical analysis these zeroth-order actions are not constants of the motion but rather are functions of time (only in a completely integrable system[12,13] are actions constants). The evolution of the system can be described as a classical trajectory in action space. In a semiclassical analysis the system is described by a wave function $\psi(I_1,I_2,...,I_{42})$ in the same space. The population of a given zeroth-order state corresponds to $|\psi(I_1,I_2,...,I_{42})|^2$. Initially all population is concentrated at a point corresponding to the light state. A detailed semiclassical description would involve the description of the time evolution of the total wave function $\psi(I_1,I_2,...,I_{42})$, or equivalently, the population of all vibrational states involved in the analysis. Instead, we focused on the total population of the tiers.

Qualitatively, the tier coordinate n is a measure of distance in action space from the light state to an average state belonging to the tier n. (n is exactly the order of coupling, described earlier, of the states in the tier to the light state.) Thus, the population of the nth tier, $P_n(t)$, describes the total population of a particular region in action space, which is some distance away from the light state along the relaxation path. $P_n(t)$ can also be regarded qualitatively as "radial" density of the total multidimensional wave function. Thus, the discussion of the dynamics in the present calculations is reduced to that along a one-dimensional tier coordinate. The qualitative picture that emerges from our calculations is as follows. Along the tier coordinate the initial distribution localized at P_0 is separated from distant tiers by a dynamic barrier, a barrier in action space and not in the coordinate space in this case. The relaxation of the initial distribution can be regarded as due to tunneling through this barrier to regions where the quasi-resonant states are available. The population under the barrier is always very small, as in the usual case of tunneling under a potential barrier in coordinate space. Details of this tunneling relaxation dynamics have been the focus of various sections of this paper.

In many studies of the CH stretch relaxation it was suggested that the stretch–bend interaction plays the key role, because of a good 1:2 stretch–bend resonance[20,23-25] in case CH is attached to a rigid skeleton of a molecule, as, for example, in benzene[20] or in CX_3H.[23,25] In the case of $(CH_3)_3CCCH$ molecule the bend frequency is only of the order of 700 cm^{-1}, because of the "soft" bend nature of the acetylenic part in the molecule. In this case the usual stretch–bend resonance does not play any significant role, at least in the present model where only low-order direct couplings are considered. In such a situation the high-frequency CH stretch is adiabatically separated from the rest of the low-frequency modes of a molecule including the CH bend. Such a situation was discussed in the early eighties by Quack and co-workers.[26] The superexchange type of vibrational couplings and tunneling provide the mechanism of relaxation out of such an adiabatic dynamical well.

V. Conclusions

We have demonstrated the mechanics of energy relaxation from a localized part of the molecule to its complete scrambling into all the available modes in the limit of statistical IVR when the decay is irreversible. This mechanism is explained within the tier formalism of sequential third-order anharmonic couplings that control the decay. The different roles played by the initial tiers when the average spacing between the states is larger than the average matrix elements and the later tiers where the density of states is high enough such that the statistical limit is reached have been demonstrated. We have also demonstrated that although the initial decay rate is a function of initial tiers only, the limit of irreversible decay is reached only in the presence of the quasi-continuum of states in the later tiers. Therefore, the irreversible decay occurs from the light states into the quasi-continuum mediated through the virtual couplings of the intermediate tiers. This mechanism clearly points out the importance of the intermediate tiers in the overall rate of relaxation and how bottlenecks in these tiers can significantly localize the excitation into the light state in spite of a large density of states available in the later tiers. This issue of localization versus statistical decay is discussed somewhere else[10,27] in detail. We have also identified an artifact of the dead-end state type and have indicated how to deal with it.

In this paper we have shown that the presence of virutal couplings in the intermediate tiers lead to superexchange between the light state and quasi-resonant states in the molecule. Dynamics of energy transfer resembles tunneling in tier space where the intermediate tiers never see a significant buildup of population. An intriguing behavior of the dynamics is shown in the threshold behavior. At very short times, when most of the population distribution is localized within the light state, some population moves along the tier coordinate such that the front of this population flow reaches successive tiers with a constant velocity. Once all the tiers have been reached, the irreversible decay out

of the initial tiers into the quasi-continuum can commence. If the tier structure is such that all the tiers cannot be reached then the probability of irreversible decay is substantially reduced.

Acknowledgment. A.A.S. thanks E. J. Heller, R. D. Levine, and M. Quack for helpful discussions and critical comments during the Berlin Conference where part of this work was presented. We are pleased to acknowledge the financial support of the National Science Foundation. This work is supported in part by the Caltech-JPL CRAY Supercomputing project. R.A.M. was asked to contribute to a volume in the *International Journal of Quantum Chemistry* dedicated to Professor I. Hjalmars-Fischer. We were not able to meet that deadline, but it is a pleasure to acknowledge her many important scientific contributions and to dedicate this article to her.

Appendix

The rapid decrease of population in the intermediate tiers with the tier index can be understood by invoking a standard argument from the high-order perturbation theory. The high-order corrections to the light state, $|\phi_0\rangle$, due to couplings to other state in the molecule can be written as

$$|\phi\rangle = |\phi_0\rangle + \sum_{k_1} c_{k_1}|\phi_{k_1}\rangle + \sum_{k_2} c_{k_2}|\phi_{k_2}\rangle + \dots \qquad (A1)$$

where sums are taken over states in the first tier, second tier, etc. From standard perturbation theory arguments one finds

$$c_{k_1} = \left\langle \phi_{k_1} \left| \frac{V}{E_0 - E_{k_1}} \right| \phi_0 \right\rangle \qquad (A2)$$

$$c_{k_2} = \sum_{k_1} \left\langle \phi_{k_2} \left| \frac{V}{E_0 - E_{k_2}} \right| \phi_{k_1} \right\rangle \left\langle \phi_{k_1} \left| \frac{V}{E_0 - E_{k_1}} \right| \phi_0 \right\rangle \qquad (A3)$$

$$\dots$$

$$c_{k_n} = \sum_{k_{n-1}} \left\langle \phi_{k_n} \left| \frac{V}{E_0 - E_{k_n}} \right| \phi_{k_{n-1}} \right\rangle c_{k_{n-1}} \qquad (A4)$$

where V is the anharmonic coupling operator and E_k is the energy of the kth zeroth-order state. If one neglects interference effects and assumes that there are no strong resonances, then the population of a quasi-stationary state is given by

$$|c_{k_n}|^2 = \sum_{k_{n-1}} \left| \left\langle \phi_{k_n} \left| \frac{V}{E_0 - E_{k_n}} \right| \phi_{k_{n-1}} \right\rangle \right|^2 |c_{k_{n-1}}|^2 \qquad (A5)$$

The population of the whole tier then can be written as

$$P_n = \sum_{k_n} |c_{k_n}|^2 = \sum_{k_{n-1}} \left(\sum_{k_n} \left| \frac{V_{k_n k_{n-1}}}{E_0 - E_{k_n}} \right|^2 \right) |c_{k_{n-1}}|^2 \qquad (A6)$$

Thus one can write

$$P_n = \sum_k |c_k|^2 \simeq f P_{n-1} \qquad (A7)$$

if one assumes that the factor f is roughly the same for the intermediate tiers

$$f = \sum_{k_n} \left| \frac{V_{k_n k_{n-1}}}{E_0 - E_{k_n}} \right|^2 \qquad (A8)$$

It is thus seen that, if there are no resonant states in the sequence of tiers, the population decays roughly exponentially. For example

$$P_n = f^{n-3} P_3 \qquad (A9)$$

The same type of mechanism explains the exponential distance dependence of the electronic coupling in long-distance electron-transfer processes.

Of course, the above arguments hold only when there are no resonant states in the tier and the states are distributed in tiers more or less randomly. As the tier index increases, the density of states increases also increasing the chance to have good resonances. The above arguments, then, are not valid.

References and Notes

(1) Stuchebrukhov, A. A.; Marcus, R. A. *J. Chem. Phys.* **1993**, *98*, 6044.

(2) Kerstel, E. R. Th.; Lehmann, K. K.; Mentel, T. F.; Pate, B. H.; Scoles, G. *J. Phys. Chem.* **1991**, *95*, 8282.

(3) Gambogi, J. E.; L'Esperance, R. P.; Lehmann, K. K.; Pate, B. H.; Scoles, G. *J. Chem. Phys.* **1993**, *98*, 1116.

(4) Newton, M. D. *Chem. Rev.* **1991**, *91*, 767. Siddarth, P.; Marcus, R. A. *J. Phys. Chem.* **1992**, *96*, 3213.

(5) Kramers, H. A. *Physica* **1934**, *1*, 182. Anderson, P. W. *Phys. Rev.* **1950**, *79*, 350. McConnell, H. M. *J. Phys. Chem.* **1961**, *35*, 508.

(6) Wyatt, R. E. *Adv. Chem. Phys.* **1989**, *73*, 231.

(7) Wyatt, R. E.; Iung, C.; Leforestier, C. *J. Chem. Phys.* **1992**, *75*, 3458. Wyatt, R. E.; Iung, C.; Leforestier, C. *J. Chem. Phys.* **1992**, *75*, 3477.

(8) Marshall, K. T.; Hutchinson, J. S. *J. Chem. Phys.* **1991**, *95*, 3232.

(9) Luckhaus, D.; Quack, M. *Chem. Phys. Lett.* **1992**, *190*, 511. Quack, M. *Annu. Rev. Phys. Chem.* **1990**, *41*, 839.

(10) Heller, E. J. *Phys. Rev. A* **1987**, *34*, 1360.

(11) Remacle, F.; Levine, R. D. *J. Chem. Phys.* **1993**, *98*, 2144.

(12) Lichtenberg, A. J.; Lieberman, M. A. *Regular and Stochastic Motion*; Springer: New York, 1983.

(13) Uzer, T. *Phys. Rep.* **1991**, *199*, 73.

(14) Davis, M. J.; Heller, E. J. *J. Phys. Chem.* **1981**, *85*, 307.

(15) Miller, W. H.; George, T. F. *J. Chem. Phys.* **1972**, *56*, 5668. George, T. F.; Miller, W. H. *J. Chem. Phys.* **1972**, *57*, 2458. Stine, J.; Marcus, R. A. *Chem. Phys. Lett.* **1972**, *15*, 536. Miller, W. H. *Chem. Phys. Lett.* **1974**, *7*, 431. Stine, J.; Marcus, R. A. *Chem. Phys. Lett.* **1974**, *29*, 575. Miller, W. H. *Adv. Chem. Phys.* **1974**, *25*, 69. Miller, W. H. *Adv. Chem. Phys.* **1975**, *30*, 77. Noid, D. W.; Marcus, R. A. *J. Chem. Phys.* **1977**, *67*, 559. Marcus, R. A.; Coltrin, M. E. *J. Chem. Phys.* **1977**, *67*, 2609. Lawton, R. T.; Child, M. S. *Mol. Phys.* **1979**, *37*, 1799. Babamov, V. K.; Marcus, R. A. *J. Chem. Phys.* **1981**, *74*, 1780. Davis, M. J.; Heller, E. J. *J. Chem. Phys.* **1981**, *75*, 246. Davis, M. J.; Heller, E. J. *J. Chem. Phys.* **1981**, *75*, 3915. Sibert III, E. L.; Reinhardt, W. P.; Hynes, J. T. *J. Chem. Phys.* **1982**, *77*, 3583. Sibert III, E. L.; Hynes, J. T.; Reinhardt, W. P. *J. Chem. Phys.* **1982**, *77*, 3595. Jaffe, C.; Reinhardt, W. P. *J. Chem. Phys.* **1982**, *77*, 5191. Shirts, R. B.; Reinhardt, W. P. *J. Chem. Phys.* **1982**, *77*, 5204. Noid, D. W.; Koszykowski, M. L.; Marcus, R. A. *J. Chem. Phys.* **1983**, *78*, 4018. Uzer, T.; Noid, D. W.; Marcus, R. A. *J. Chem. Phys.* **1983**, *79*, 4412. Conner, J. N. L.; Uzer T.; Marcus, R. A.; Smith, A. D. *J. Chem. Phys.* **1984**, *80*, 5095. Stefanski, K.; Pollak, E. *J. Chem. Phys.* **1987**, *87*, 1079.

(16) Mackay, R. S.; Meiss, J. D.; Percival, J. C. *Physica D* **1984**, *13*, 55. Bensimon, D.; Kadanoff, L. P. *Physica D* **1984**, *13*, 82. Davis, M. J. *J. Chem. Phys.* **1985**, *83*, 1016. Davis, M. J.; Gray, S. K. *J. Chem. Phys.* **1986**, *84*, 5389. Gray, S. K.; Rice, S. A.; Davis, M. J. *J. Phys. Chem.* **1986**, *90*, 3470.

(17) Zhang, Y.-F.; Marcus, R. A. *J. Chem. Phys.* **1992**, *96*, 6065.

(18) Gordon, R. G. *Adv. Magn. Reson.* **1968**, *3*, 1. In eq 19 of this reference one substitutes $\mu = \mu_{eg}|\phi_e\rangle\langle g| + \mu_{eg}|g\rangle\langle\phi_e|$, where $|g\rangle$ is the ground vibrational state. Also $E_g = \langle g|H|g\rangle$ is set equal to zero and $\mu(t) = e^{iHt}\mu e^{-iHt}$.

(19) Lehmann, K. K.; Pate, B. H. *J. Mol. Spectrosc.* **1990**, *144*, 443.

(20) Sibert III, E. L.; Reinhardt, W. P.; Hynes, J. T. *Chem. Phys. Lett.* **1982**, *92*, 455. Sibert III, E. L.; Reinhardt, W. P.; Hynes, J. T. *J. Phys. Chem.* **1984**, *81*, 1115. Sibert III, E. L.; Hynes, J. T.; Reinhardt, W. P. *J. Phys. Chem.* **1984**, *81*, 1135.

(21) Stuchebrukhov, A. A.; Marcus, R. A. *J. Chem. Phys.* **1993**, *98*, 8443.

(22) Harter, W. G.; Patterson, C. W. *J. Chem. Phys.* **1984**, *80*, 4241. Harter, W. G. *J. Chem. Phys.* **1985**, *85*, 5560.

(23) Dübal, H.-R.; Quack, M. *J. Chem. Phys.* **1984**, *81*, 3779.

(24) Halonen, L. *J. Phys. Chem.* **1988**, *93*, 3386.

(25) Voth, G. A.; Marcus, R. A.; Zewail, A. H. *J. Chem. Phys.* **1984**, *81*, 5494.

(26) von Puttkamer, K.; Dübal, H.-R.; Quack, M. *Faraday Discuss. Chem. Soc.* **1983**, *75*, 197.

(27) Mehta, A.; Stuchebrukhov, A. A. Manuscript in preparation.

Chapter 2

Superexchange Mechanism of Intramolecular Vibrational Relaxation : Localization Properties

Superexchange Mechanism of Intramolecular Vibrational Relaxation : Localization Properties

Aseem Mehta and Alexei A. Stuchebrukhov

Arthur Amos Noyes Laboratory of Chemical Physics,
California Institute of Technology,
Pasadena, CA, 91125

Abstract

The intramolecular vibrational relaxation of the acetylenic CH stretch in polyatomic molecules $(CH_3)_3YCCH$, where Y = C or Si, is due to a sequence of many weak off-resonant vibrational transitions between tiers of directly coupled (by low-order anharmonic terms) states. The energy flow from the initially populated light state to the high density of states in the later tiers is mediated by the off-resonant virtual transitions to the intermediate tiers. In this tier model, the relaxation can be thought of as occurring via tunneling (vibrational superexchange) through a dynamic barrier which separates the light state and the quasiresonant states. Randomness of the couplings and dynamic barriers may cause a localization of the vibrational excitation in the action space of the system similar to the localization of electronic wavefunctions in random solids. In the present paper these localization properties of the tier system of $(CH_3)_3YCCH$ molecules are studied with a method originally developed for random solids by Skinner and co-workers. The connectivity of the vibrational states along the tier coordinate of the molecule is calculated. The observed absence of relaxation in Si- compound in numerical simulation and the unusually slow rate that has been observed experimentally are discussed in relation to the localization phenomenon.

2.1 Introduction

In recent experimental studies of the acetylenic CH stretch in $(CX_3)_3YCCH$ molecules, X = H, D; Y = C or Si, Scoles, Lehmann, and collaborators[1, 2] have observed extremely narrow, FWHM = $10^{-1} - 10^{-3}cm^{-1}$, vibrational lines. The homogenous width of the lines is a measure of the rate of intramolecular relaxation of vibrational excitation (IVR) of the CH stretch. In the first paper of this series[3] it was found that the unusually slow relaxation rate (of the order of hundreds of picoseconds), corresponding to such narrow linewidths, is due to the absence of direct low-order Fermi resonances such as the stretch-bend interactions that exist in CH_3X molecules[4]. The relaxation in this model is assumed to occur in a sequence of many virtual transitions between tiers of directly coupled states, whereby the excitation in the initially populated non-stationary state uses the best resonances available, *i.e.* the resonances with large detunings, to reach the quasiresonant states that may exist in higher tiers. The number of sequential virtual transitions (number of tiers) required can be as large as ten or more. The large detunings of available resonances (or the absence of direct resonances) can be regarded as dynamical barriers separating the light state, from which relaxation occurs, from the quasiresonant states. It has been shown that the relaxation dynamics in tier system occurs via a tunneling like mechanism ("vibrational superexchange") under these dynamical barriers[5].

The randomness of couplings, tunneling barriers, and the very scheme of sequential coupling of vibrational states in IVR resembles, in many respects, the situation in random solids. Wolynes and co-workers[6, 7, 8] have recently argued that effects similar to localization phenomena in random solids[9, 10] can be expected in IVR. By localization, (absence of relaxation) it is essentially meant that the initial state is effectively mixed with only a few states, at best. In the opposite case of delocalization (exponential relaxation) the light state is strongly mixed with almost all states of the same energy and the density of the bath states is high enough for irreversible relaxation to occur out of the initially populated state.

Upon localization, only a finite few of the zeroth-order states contribute signifi-

cantly to each of the eigenstates of the diagonalized system. In this case, instead of an exponential decay of the initially prepared state, at best quantum beats would be expected in the dynamics of that state. The absorption spectrum would contain only one or a few sharp lines instead of the Lorentzian-like contour that would occur when all the isoenergetic states are mixed.

The cumulative density of states, ρ_n^{eff}, increases rapidly with the number of tiers. The average effective coupling of the light state to levels in the nth tier, V_n^{eff} is of the nth order and in the case of weak coupling between tiers is an exponentially decreasing function of n. For relaxation to occur, the density of coupled states should be high enough to ensure the statistical limit, $\rho^{eff}V^{eff} \gg 1$. In the weak coupling case it might happen that the effective interaction, V_n^{eff}, decreases faster with n than the corresponding increase of the density of states, ρ_n^{eff}, decoupling the later tiers. Then the statistical limit, $\rho_n^{eff}V_n^{eff} \gg 1$ will not be reached even when all states are included in the analysis. In this situation localization of vibrational energy into a few modes of the molecule, irrespective of the total high density of states, occurs.

In their experiments, Scoles, Lehmann, and co-workers[1, 2] observed that the linewidth of the acetylenic CH fundamental transition for the Si- compound is an order of magnitude smaller than its C- counterpart, although on the basis of total density of states the opposite result would be expected. Also, recent model calculations[3] have indicated that the transition line for Si- molecule is not homogeneously broadened at all. It was suggested that accidental bottlenecks in relaxation pathways and dynamic barriers can cause virtual localization of the CH stretch vibration. In the light of those results, and following up on the discussion of similarity between random solids and vibrational couplings in polyatomic molecules, it seems reasonable to apply some standard technique from the study of random solids to these molecules in order to investigate the possibility of localization of the vibrational excitation in a more quantitative way.

In the present paper the localization properties of the tier system of $(CH_3)_3YCCH$ molecules, Y = C or Si, are studied with a method originally developed for random solids by Skinner and co-workers[11, 12]. In this method, connectivity of vibrational

states along the tier coordinate of the molecule is calculated. The connectivity may then be used to characterize the strength of the coupling of the dark states along the tier coordinate with the light states. The importance of the connectivity as a function of tiers stems from the fact that the high density of states, necessary for the relaxation to occur, is only available in the higher tiers, or, in other words, a large distance away from the light state in action space of the molecule. To make use of these energetically closely spaced states, there must be appreciable coupling to those states. The connectivity quantitatively describes the strength of this coupling. It is found that for the C- compound this measure of coupling is much larger than that for the Si- molecules for all the tiers. This result is in qualitative agreement with experimental data on the relaxation rates in these compounds[1, 2]. The participation ratio, defined below, for each eigenstate is also calculated to compare the overall coupling between states in the two molecules.

The structure of the paper is as follows. In section 2 the concept of connectivity of vibrational states is introduced. In section 3 the results from the various calculations are stated followed by a short conclusion in section 4.

2.2 Tier system and connectivity of vibrational states

It was shown in previous publications[3, 5] that the CH vibrational states in $(CX_3)_3YCCH$ molecules are coupled to a manifold of background states via a sequence of transitions which result in the tier system, as shown in Fig. 1. Details and discussion about the tier system can be found in the first paper of this series, Ref. 3.

Each level shown in Fig. 1 is described by 42 vibrational quantum numbers, its vibrational energy, which includes anharmonic corrections, and various couplings to previous and the next tiers.

Qualitatively, the tier coordinate n measures the distance in action space from the light state to an average state belonging to the tier n. (Rigorously speaking, n is the order of coupling of the states in the tier to the light state.) If the dynamics of the tier system is studied, as we have done in the second paper of this series[5],

then the total population of the nth tier, $P_n(t)$, describes the total population of the region in action space, which is some distance away from the light state along the relaxation path. $P_n(t)$ can also be regarded qualitatively as "radial" density of the total multidimensional wave function. Thus the complicated dynamics is reduced to an effective one-dimensional problem along the tier coordinate . The qualitative picture that emerged from our previous calculation is the following. Along the tier coordinate, the initial distribution localized at $|0\rangle$, the light state, is separated from the distant tiers by a dynamic barrier, because of the absence of direct resonances. The relaxation of the initial distribution is due to tunneling through this barrier to regions where quasi-resonant states are available. Details of this tunneling relaxation dynamics in $(CH_3)_3CCCH$ were discussed in Ref. 5. The necessary condition for relaxation is that the product of the density of quasiresonant states on the "other side" of the barrier and effective coupling of the light state to those states be larger then unity.

The overall coupling within the Hilbert space of zeroth-order states may be visualized through the concept of the spread of each of the eigenstates within the space defined by the zeroth-order states. This spread is quantitatively studied by calculating

$$P_\mu = \sum_{i=1}^{N} |c_{i\mu}|^4. \tag{2.1}$$

Here,

$$c_{\mu i} = \langle \mu | i \rangle, \tag{2.2}$$

where, $|i\rangle$ belongs to the zeroth-order basis set, $|\mu\rangle$ belongs to the set of eigenstates and N is the dimension of the Hilbert space. The coefficients, $c_{i\mu}$, are simply the values obtained from the eigenvectors after the total diagonalization of the Hamiltonian. For a completely delocalized eigenstate $|c_{i\mu}| = 1/\sqrt{N}$, as in Bloch functions. Thus, for delocalized eigenstates, $P_\mu = 1/N$. Also, when a zeroth-order state is also an eigenstate, complete localization obviously makes $P_\mu = 1$. Values of P_μ between the two limits imply an incomplete spread of the eigenstate. This incomplete spread of each eigenstate, $|\mu\rangle$, may be quantified by $l = 1/P_\mu$, the participation ratio, which may be

regarded as the number of zeroth-order states that span the eigenstate. Determination of l provides a method for measuring the degree to which each eigenstate spreads within the basis set of the zeroth-order states. Also, unless each eigenstate is completely (or nearly completely) spread among all the zeroth-order states, $l \sim O(N)$, most of the participation ratios should be independent of N. Field and coworkers have also used this procedure in their investigation of quantum ergodicity in the SEP spectra of highly vibrationally excited acetylene[13].

As mentioned before, the effective coordinate of interest is the tier coordinate. The localization property along this tier coordinate is another quantitative characteristic that describes the mixing of vibrational states with the light state. This characteristic can be studied with the method developed originally by Skinner and co-workers for random solids[11, 12]. The relevant question here is : How far along the tier coordinate can the excitation spread?

Skinner and co-workers introduced a concept of quantum connectivity as a generalization from percolation theory to describe couplings in random solids. It is qualitatively clear that two states $|i\rangle$ and $|j\rangle$ are coupled if both $c_{\mu i}$ and $c_{\mu j}$ are nonzero for some eigenstate $|\mu\rangle$. Then, the connectivity, Δ_{ij}, between them is defined as

$$\Delta_{ij} = \frac{P_{ij}}{\sqrt{P_{ii}P_{jj}}}, \tag{2.3}$$

where,

$$P_{ij} = \sum_{\mu} |c_{i\mu}|^2 |c_{j\mu}|^2. \tag{2.4}$$

The denominator in Eq. (3) is introduced to "normalize" the quantity P_{ij}.

The appropriate parameter of interest is the average connectivity per state between the light state and the kth tier,

$$\overline{P_k} = \frac{\sum_{j=1}^{N_k} \Delta_{0j}}{N_k}, \tag{2.5}$$

for each tier, where N_k is the number of levels in the kth tier. This average allows the comparison of the degree of connectivity between the light states and an "average"

state in various tiers. $S_k = \sum_{j=1}^{N_k} \Delta_{0j}$ is also a useful quantity that helps in our analysis as it quantifies the degree to which a tier, or equivalently a certain part of the action space (as described in the introduction), is connected to the light state.

Finally, it is very useful to compare the $\overline{P_k}$ and S_k values between different molecules to determine the difference in the degree to which the light state is connected to the other states in different species. For Bloch waves $\overline{P_k} \equiv 1$.

2.3 Results

The localization properties defined as above are now investigated for $(CH_3)_3CCCH$ and $(CH_3)_3SiCCH$. The average quantum connectivity is calculated for each tier of these molecules. In order to do so, 10 tiers of sequentially coupled (through third-order anharmonic matrix elements) states were generated for these two compounds with a computer program described in Ref. 3. The first six tiers for these molecules are shown in Fig. 1. Imposing a perturbation theory based criterion on the selection procedure, it turns out that tert-butylacetylene has about 600 well coupled states in ten tiers. For the Si-compound the criterion for the selection of states was considerably relaxed. Without this, the third tier of the Si molecule would be left without a state, due to a bottleneck discussed in Ref. 3, completely decoupling the further tiers. With this relaxed criterion (as compared to $(CH_3)_3CCCH$) for the Si compound, the total number of states in ten tiers were about 1400, although the overall anharmonic couplings between states for the Si molecule are considerably smaller than those for tert-butylacetylene.

We have also investigated the effect of the addition of fourth-order anharmonic couplings between states. While it is possible to add fourth-order anharmonicities to the model in a manner similar to that for third-order values, we have chosen a more phenomenological approach as only the gross dependencies of $\overline{P_k}$ values on the fourth-order numbers were desired. Because of the presence of other approximations, further refinements for the calculation of fourth-order anharmonic couplings would not provide useful information. With this in mind, the fourth-order values were added

as a constant coupling between each pair of levels from the nth and the $n+2$nd tiers.

The differences between the relaxation mechanisms of the molecules are most apparent when the survival probabilities $|\langle 0|e^{-i\hat{H}t}|0\rangle|^2$ are compared. For $(CH_3)_3SiCCH$, the population of the light state is more that 0.99 for $t \leq 2$ns. The carbon case was exhaustively studied in a previous publication[5]. It was shown that there is significant relaxation of the light state into the 10 tiers. Addition of an 11th tier with a quasicontinuum of resonant states allowed irreversible statistical decay out of the light state. The addition of the quasicontinuum in the silicon molecule makes no difference since there is absolutely no relaxation into the initial tiers. The latter fact is essential as it is the initial tiers that serve as a conduit for statistical decay of the population into the quasicontinuum in the carbon case. It is clear that the structure of the initial tiers is critical (as mentioned previously, the total density of states is significantly greater in the silicon molecule) and is probably the cause of the localization of excitation in the light state of $(CH_3)_3SiCCH$. We now report various aspects of this phenomenon.

The plots of the average quantum connectivity, $\overline{P_k}$, for the carbon and the silicon compound are shown in Fig. 2 and the differences are significant. The most important observation is that the absolute average quantum connectivity (Eq. 5) for $(CH_3)_3CCCH$ is two to four magnitudes higher than its silicon counterpart. Therefore, the capacity of a typical "dark" state in the silicon compound to carry away intensity from the light state is considerably less than that for the carbon compound. This result seems to account for the almost complete lack of statistical IVR decay in the silicon compound. The connectivity of the states in intial tiers is small to begin with and then it falls so fast that the later tiers, where the high density of states exists, are essentially uncoupled to the light state. While Fig. 2 shows a steady and relatively large "quantum connectivity" values for $(CH_3)_3CCCH$, the corresponding values for $(CH_3)_3SiCCH$ are small and drop precipitously. The difference in the "quantum connectivity" values for $(CH_3)_3CCCH$ and $(CH_3)_3SiCCH$ is striking and such difference may indicate the difference between statistical relaxation and long localization. This observation reinforces the results from the dynamics calculations,

allowing the conclusion that the complete lack of well coupled resonant states in the initial tiers results in the virtual localization of the initial excitation in the $\equiv C-H$ stretch in the molecule $(CH_3)_3SiCCH$. As a reference, it is worth mentioning that for perfect Bloch waves, $\log \overline{P_k} \equiv 0$ as all $|c_{i\mu}| = 1/\sqrt{N}$.

The plot of $\log(S_k)$ vs. k also gives similar results. While the S_k values remain constant at a relatively high level for tert-butylacetylene, actually increasing with tier number for later tiers with the increase in the number of states, the same values for the Si substituted molecule drop fast and remain 4-5 orders of magnitude smaller (Fig. 3). The total density of states in the silicon compound is about 30 times higher than that of the the carbon compound. Based on only this factor the number of resonant states should be much higher for the former case. And yet, as is seen from our results, while a large overall density of states may be necessary for IVR to occur in the statistical limit, it is not a sufficient condition. The strength of the coupling, as well as the exact energy difference between the light state the individual dark states, especially for the first few tiers, is also very important. The more or less energetically random composition of the levels may create bottlenecks, as in $(CH_3)_3SiCCH$, which significantly decrease the overall coupling to the background states that, if available, provide the final states for real (as opposed to virtual) transitions with conservation of energy, and eventually can absorb a significant amount of the initial excitation.

To confirm our conjecture about the bottleneck in the third tier, we calculated $l = 1/P_\mu$ for all the eigenstates for both the molecules. The histograms are shown in Fig. 4. The distributions, when the difference in the total number of states in the two simulations are taken in account, are remarkably similar. $\bar{l}$ is 8 and 17 for $(CH_3)_3CCCH$ and $(CH_3)_3SiCCH$, respectively. In Fig. 5, the normalized histogram is shown. In this Fig. the frequency of occurrence of some range of values of l is divided by N, the total number of states. Comparing the normalized curves for the two molecules shows that the nature of overall couplings for the two molecules is quite similar. Therefore, it can be surmised that, within the limits of the calculation (by definition due to the artificial nature of the cutoff used for the AI search, and so, the uncertainty in the total number of states), *on average*, the eigenstates in both the

molecules are spread to a similar degree.

However, the histogram in Fig. 5 reflects the distribution of coupling of *all* the eigenstates. On the other hand, only a few of these eigenstates, the ones that have a non-zero overlap with the light state, can be probed experimentally. So, if only those eigenstates that have $\langle 0|\mu\rangle^2 > 0.01$ are considered, then there are five such eigenstates in $(CH_3)_3CCCH$ with an average l of about 5 while for the Si- counterpart there is only one such state with $l = 1$. Thus, a distinction needs to be made between the overall nature of the interactions and those which can be experimentally probed, *i.e.* the difference between the statistical and the particular nature of the eigenstates.

The most useful method of calculating these particular interactions between the light and dark states has already been presented in Figs. 2 and 3. We, therefore, must interpret two results which on the surface seem contradictory: the difference between the average connectivity between the two molecules (Fig. 2) and the similarity in the distribution of the participation ratios (Fig. 5) This seeming contradiction is just an indication of the above mentioned distinction between the statistical and the particular.

These two results confirm that the cause of localization in the Si- molecule is accidental in nature and that it is the accidental bottleneck in the third tier due to the *local* (not *global*) lack of strong coupling that causes the unusual degree of localization in $(CH_3)_3SiCCH$. From this analysis the following qualitative picture can be drawn. For the Si- compound, the light state, despite an availability of a high density of total states, is unable to utilize them due to the structure of the tiers that disallows good coupling between the first few, *viz.* three, crucial tiers and the later tiers where the well-resonant and dense tiers of states exist, thereby blocking any significant leakage of the light state amplitude. Such fortuitous localization is absent in t-butylacetylene and the high density of states that is be present in the later tiers can participate in IVR. The figures of the tier structure pictorially confirm that in spite of the larger density of states for the Si compound, its tier structure, with a near bottleneck in the third tier and the lack of good resonant states in the earlier tiers, acts as a barrier to IVR.

We find that the $\overline{P_k}$ values for the carbon compound do not change significantly upon the addition of fourth-order anharmonicities. However, the Si compound values change if we add fourth-order anharmonicities of the same magnitude as those put into the carbon simulation. This result is not surprising and indicates that for the carbon case the fourth-order anharmonicities are relatively unimportant, the third-order values being large enough to dwarf any effect that the fourth-order values may have. However, the third-order values are not large enough in $(CH_3)_3SiCCH$ allowing the fourth-order values to significantly change the average quantum connectivities.

In their study, Lehmann *et al.*[3] report a large lifetime of $\approx$ 2ns and conclude from their measurements that the narrow broadening of the silicon compound is a Lorentzian with a long lifetime/small FWHM. For our ten tier simulation for the fundamental stretch we do not see any decay for up to 2ns. Various reasons that may cause this discrepancy are now addressed. A further reduction of the predetermined tolerance for the AI selection of the states may be required so that more virtual couplings are provided in the initial tiers for population relaxation. This may allow the pinning down of the nature of the important initial relaxation. Furthermore, the states arising from the internal rotations of the individual methyl groups around the $(CH_3)_3$-C- bonds that are possible in this molecule have not been incorporated in this calculation. Those rotations should add further states and matrix elements causing further mixing of the states and, therefore, assist in the relaxation of the initial state. Finally, fourth-order anharmonicities may also play an important role for a correct description of this mode as the third-order couplings are so ineffective. Since the weak third-order anharmonic couplings act to localize the excitation, extra relaxation pathways that arise due to the higher anharmonic terms are probably very useful for IVR. While the higher-order terms are not as efficient in promoting IVR as third-order terms, they are capable of facilitating slow relaxation of longer periods of time. This, probably, is cause for the anomalously slow (2ns $\approx 10^6$ vibrational periods) relaxation of $(CH_3)_3SiCCH$.

2.4 Conclusion

Several concepts borrowed from the physics of random solids can be usefully employed for studying vibrational couplings in polyatomic molecules. This approach proves useful when the mechanism of IVR is vibrational superexchange. It provides an additional insight into the IVR problem and allows quantitative comparison of different molecules.

In the present paper we have applied such an approach to study vibrational couplings in $(CH_3)_3YCCH$ molecules, where Y = C, Si, and where we believe that the vibrational coupling scheme resembles the one in random solids. In particular, the unusually large relaxation time of the acetylenic CH stretch vibration in the Si- compound can be explained in terms of the length (localization length) at which vibrational states are strongly coupled to a light state along the tier coordinate. This tier coordinates qualitatively describes the distance from the light state along the relaxation path in the Hilbert space. The calculations show that the localization, rigorously defined as in random solids, does not occur in our molecules in the sense it is understood for random solids (the connectivity does not decay exponentially at large distances.) The fact that the absolute strength of the couplings is always greater for the C- compound by orders of magnitude can be interpreted as follows. The coupling of the light state in the C-compound extends to much longer distances along the tier coordinate than in the Si- compound. The important point to note is that it is at longer distances along the tier coordinate where the higher density of states is available. Thus, for the C- compound the much higher density of states (and, therefore, a larger number of total states) can be utilized for IVR via third-order vibrational couplings unlike the case in the Si- compound. For Si- compound the coupling is limited to about three tiers and so the density and the total number of strongly coupled states are not sufficient for relaxation to occur. This result agrees with our previous finding that for the Si- compound there is a bottleneck for energy flow at the third tier.

The concepts employed in the present paper also allow the of study statistical

properties of vibrational couplings. In particular we find that the bottleneck for relaxation in the Si- compound is of an accidental nature.

From a statistical viewpoint, an average eigenstate in the $(CH_3)_3SiCCH$ molecule is no less spread than one in its carbon counterpart; as is obvious from the distribution of l, the participation ratio for each of the eigenstates of the two molecules. However, when the particular eigenstates that have a non-zero overlap with the light state are considered, their participation ratio is significantly smaller than the average for the Si- molecule when compared to its C- counterpart. Therefore, while the average state is well spread out, the particular light state is localized due to the *local* lack of well resonant states.

We conclude that the faster rate of relaxation in the $(CH_3)_3CCCH$ is due to the fact that the strongest anharmonic couplings (third-order) are large enough for the initially localized wavefunction to penetrate the barrier formed by the off-resonant states in the initial tiers such that the tiers with high density of resonant states that permit the statistical relaxation of the initial excitation can be reached. On the other hand, the initial tier structure in $(CH_3)_3SiCCH$ is such that inspite of the presence of a higher density of states in the later tiers, the initial third-order couplings prevent the access of the later tiers. The slow (lifetime $\approx$2ns) relaxation in $(CH_3)_3SiCCH$ is, therefore, substantially mediated by higher-order (fourth and higher) anharmonic couplings.

2.5 Acknowledgements

We thank Prof. R. A. Marcus for his constructive criticism. The simulations described here were carried out on a CRAY Y-MP2E/116 at the Jet Propulsion Laboratory. The work is part of the JPL/CALTECH supercomputing project.

Bibliography

[1] E. R. Th. Kerstel, K. K. Lehmann, T. F. Mentel, B. H. Pate, and G. Scoles, J. Phys. Chem. **95**, 8282 (1991).

[2] J. E. Gambogi, R. P. L'Esperance, K. K. Lehmann, B. H. Pate, and G.Scoles, J. Chem. Phys. **98**, 1116 (1993).

[3] A. A. Stuchebrukhov and R. A. Marcus, J. Chem. Phys. **98**, 6044 (1993).

[4] E. L. Sibert III, W. P. Reinhardt, and J. T. Hynes, Chem. Phys. Lett. **92**, 455 (1982); E. L. Sibert III, W. P. Reinhardt, and J. T. Hynes, J. Phys. Chem. **81**, 1115 (1984); E. L. Sibert III, J. T. Hynes, and W. P. Reinhardt, J. Phys. Chem. **81**, 1135 (1984); H.-R. Dübal and M. Quack, J. Chem. Phys. **81**, 3779 (1984); L. Halonen, J. Phys. Chem. **93**, 3386 (1988); G. A. Voth, R. A. Marcus, and A. H. Zewail, J. Chem. Phys. **81**, 5494 (1984).

[5] A. A. Stuchebrukhov, A. Mehta, and R. A. Marcus, J. Phys. Chem. **97**, 12491 (1993).

[6] D. E. Logan and P. G. Wolynes, J. Chem. Phys. **93**, 4994 (1990).

[7] P. G. Wolynes, Acc. Chem. Res. **25**, 513 (1992).

[8] S. A. Schofield and P. G. Wolynes, J. Chem. Phys. **98**, 1123 (1993).

[9] P. W. Anderson, Phys. Rev. **109**, 1492 (1958).

[10] P. A. Lee and T. V. Ramakrishnan, Rev. Mod. Phys. **57**, 287 (1985).

[11] T.-M. Chang, J. D. Bauer, and J. L. Skinner, J. Chem. Phys., **93**, 8973 (1990).

[12] L. J. Root, J. D. Bauer, and J. L. Skinner, Phys. Rev. B, **37**, 5518 (1988).

[13] R. L. Sundberg, E. Abramson, J. L. Kinsey, and R. W. Field, J. Chem. Phys., **83**, 466 (1985).

Figure Captions

Fig. 1. First six tiers of sequentially coupled zeroth-order states in $(CH_3)_3CCCH$ and $(CH_3)_3SiCCH$.

Fig. 2. $Log_{10}(\overline{P_k})$ vs. k for the two molecules. See text for details.

Fig. 3. $Log_{10}(S_k)$ vs. k for the two molecules. See text for details.

Fig. 4. Histogram of the Participation ratio, l, for $(CH_3)_3CCCH$.

Fig. 5. Histogram of the Participation ratio, l, for $(CH_3)_3SiCCH$.

Fig. 6. Normalized histogram for the two species, plotted on the same curve. Bin size for l is two. $(CH_3)_3CCCH$ (+) and $(CH_3)_3SiCCH$ (*).

Figure 1

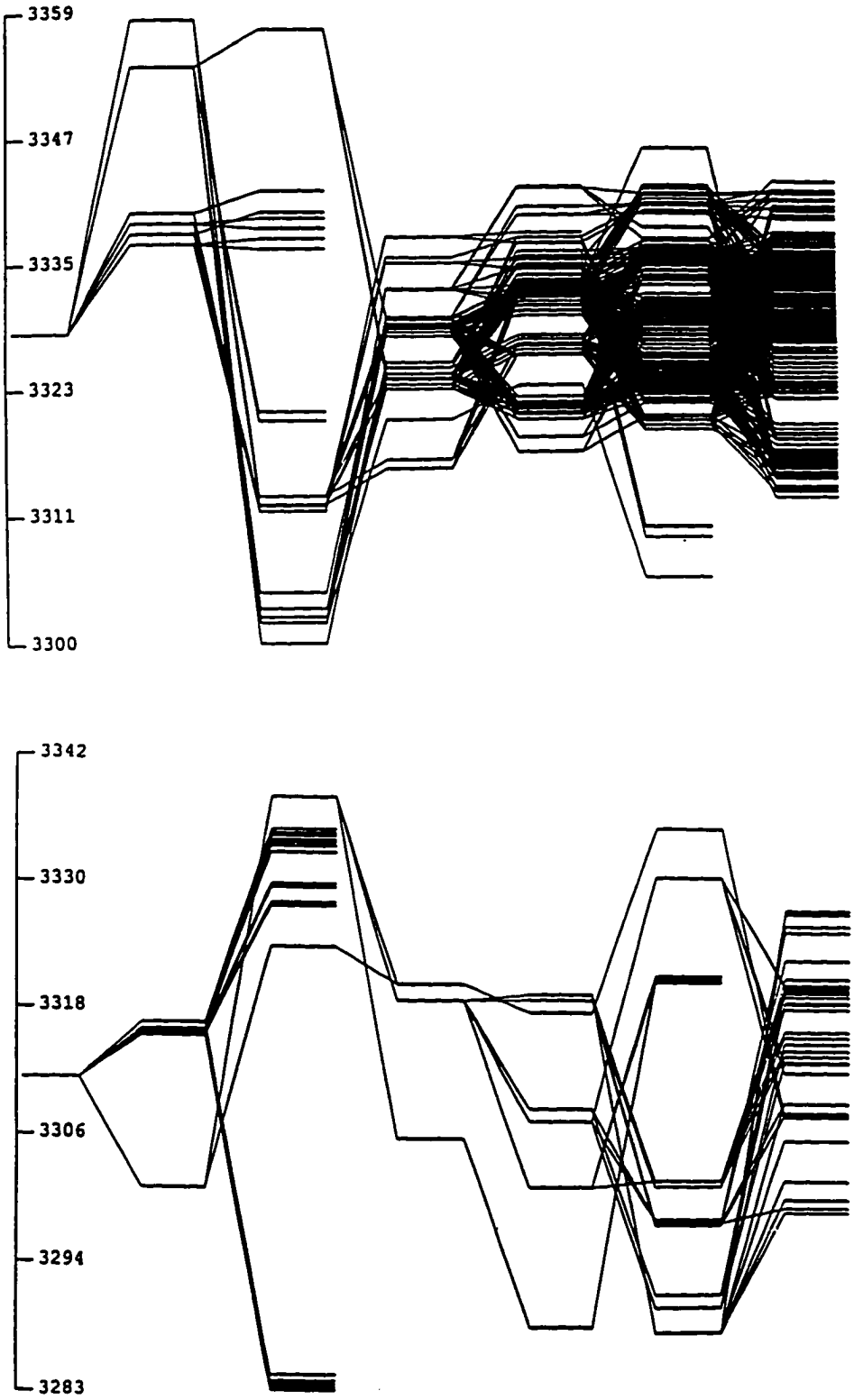

Figure 2

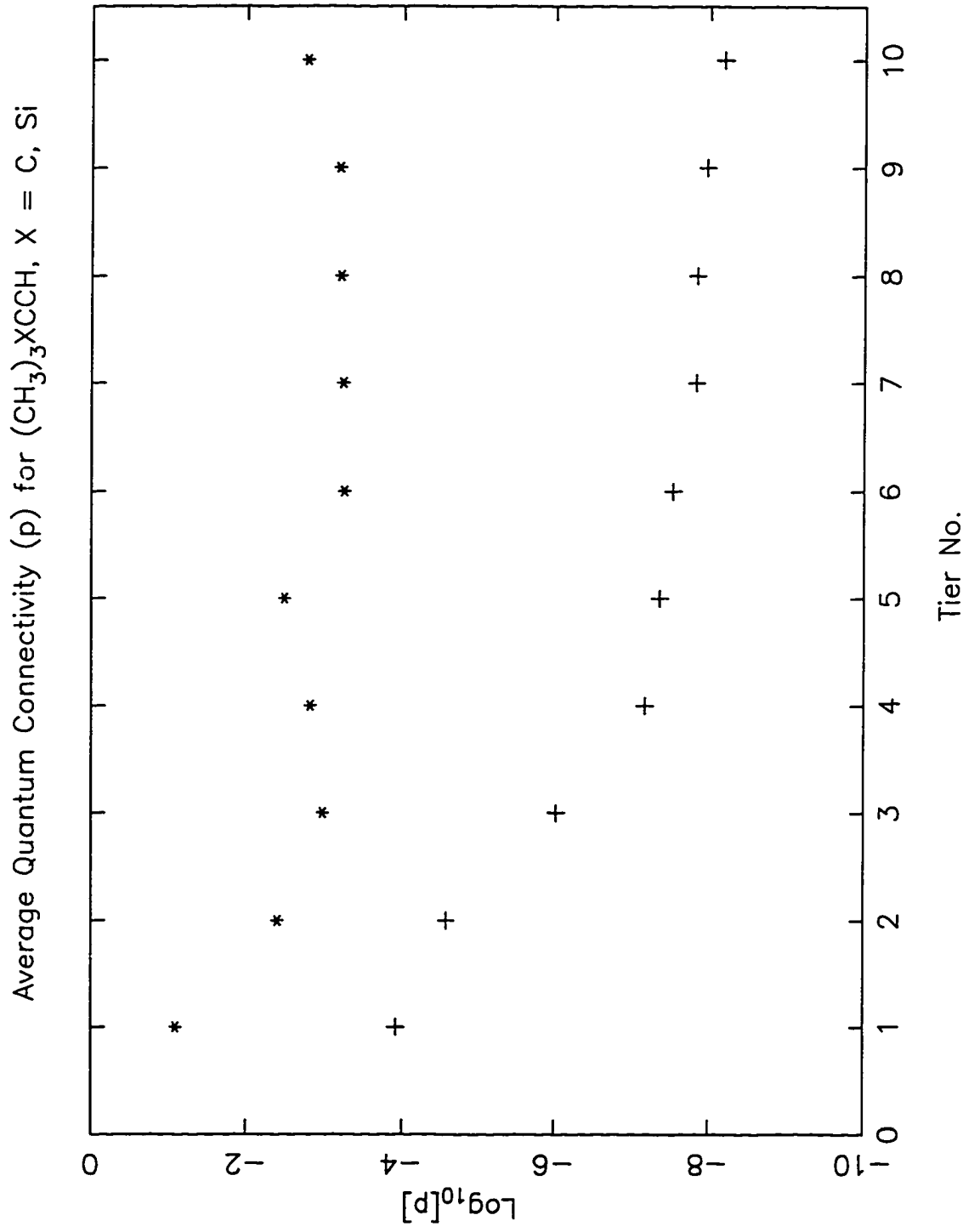
Average Quantum Connectivity (p) for $(CH_3)_3XCCH$, X = C, Si
$Log_{10}[p]$
0
−2
−4
−6
−8
−10
Tier No.
0
1
2
3
4
5
6
7
8
9
10

Figure 3

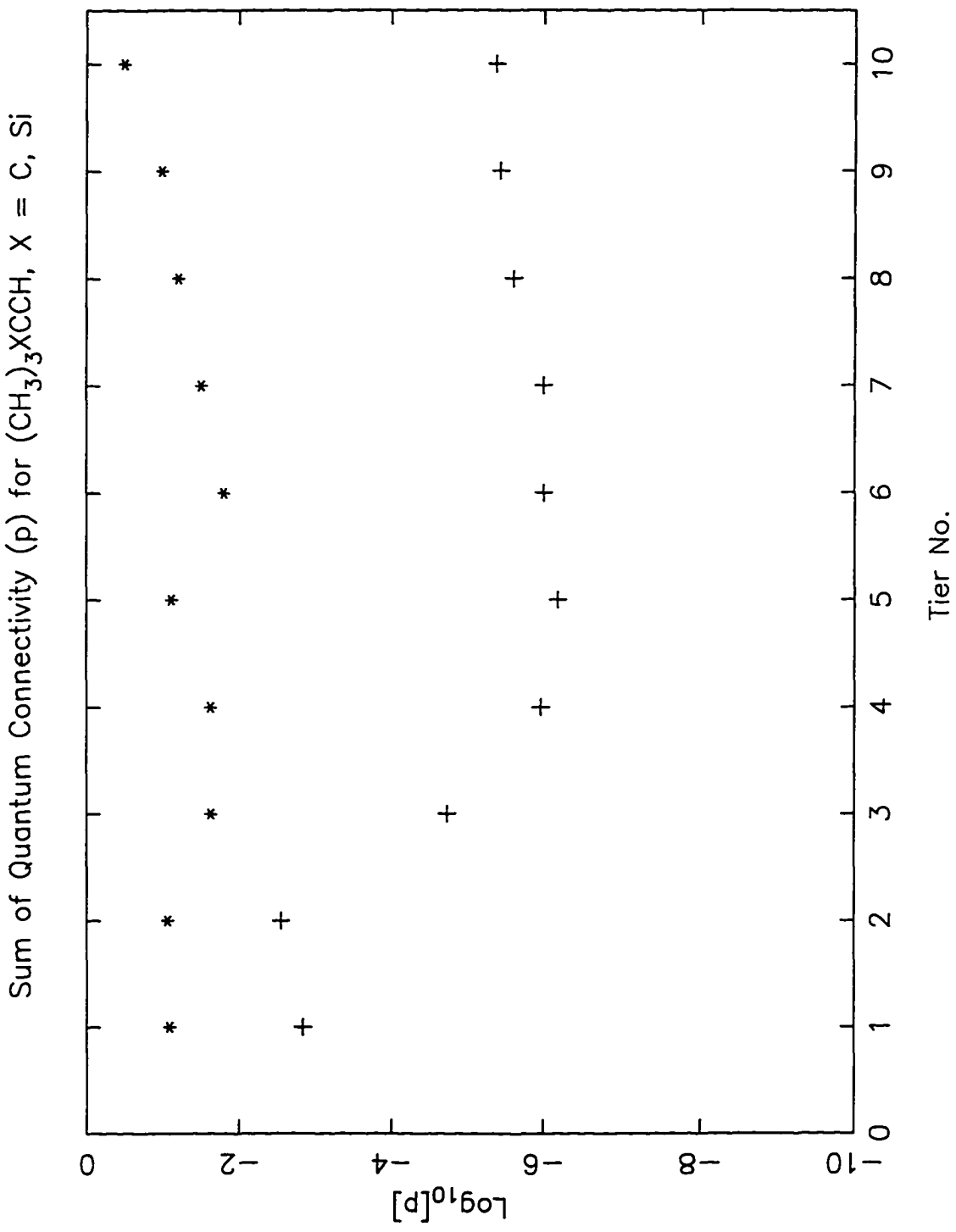
Sum of Quantum Connectivity (p) for $(CH_3)_3XCCH$, X = C, Si
$Log_{10}[p]$
0
−2
−4
−6
−8
−10
0
1
2
3
4
5
6
7
8
9
10
Tier No.

Figure 4

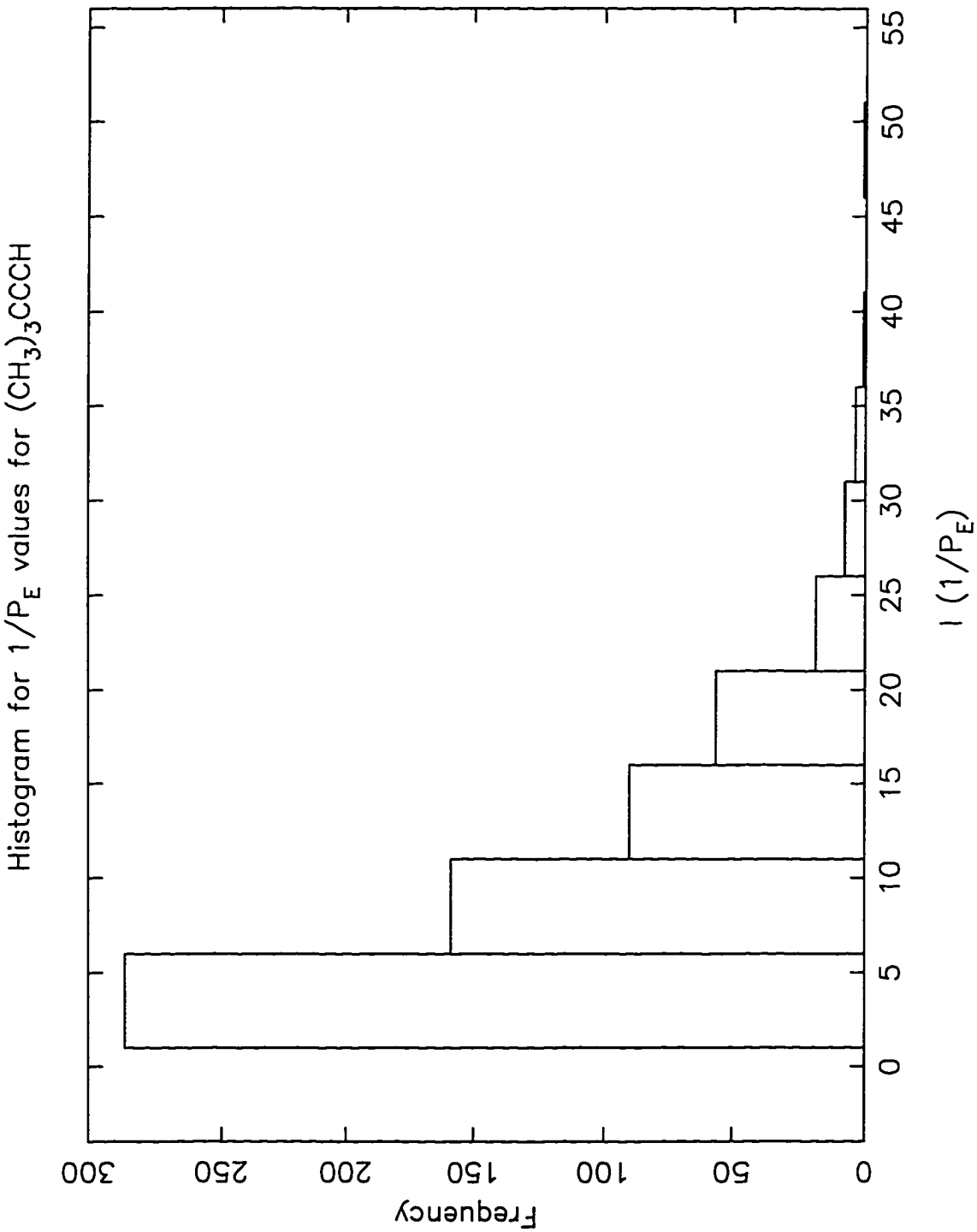
Histogram for 1/P_E values for (CH3)3CCCH
Frequency
0
50
100
150
200
250
300
I (1/P_E)
0
5
10
15
20
25
30
35
40
45
50
55

Figure 5

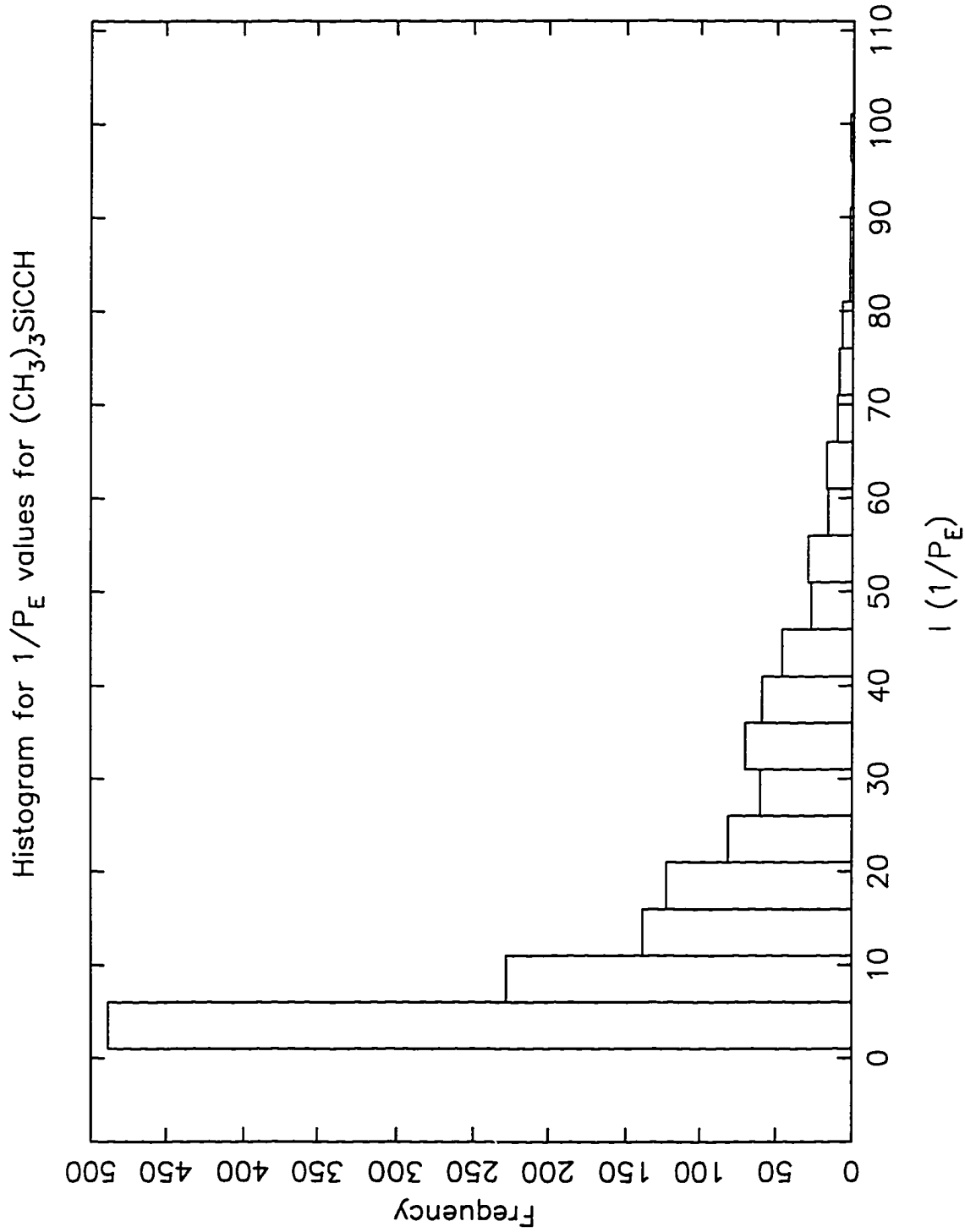
Histogram for 1/P_E values for $(CH_3)_3SiCCH$
Frequency
0
50
100
150
200
250
300
350
400
450
500
I (1/P_E)
0
10
20
30
40
50
60
70
80
90
100
110

Figure 6

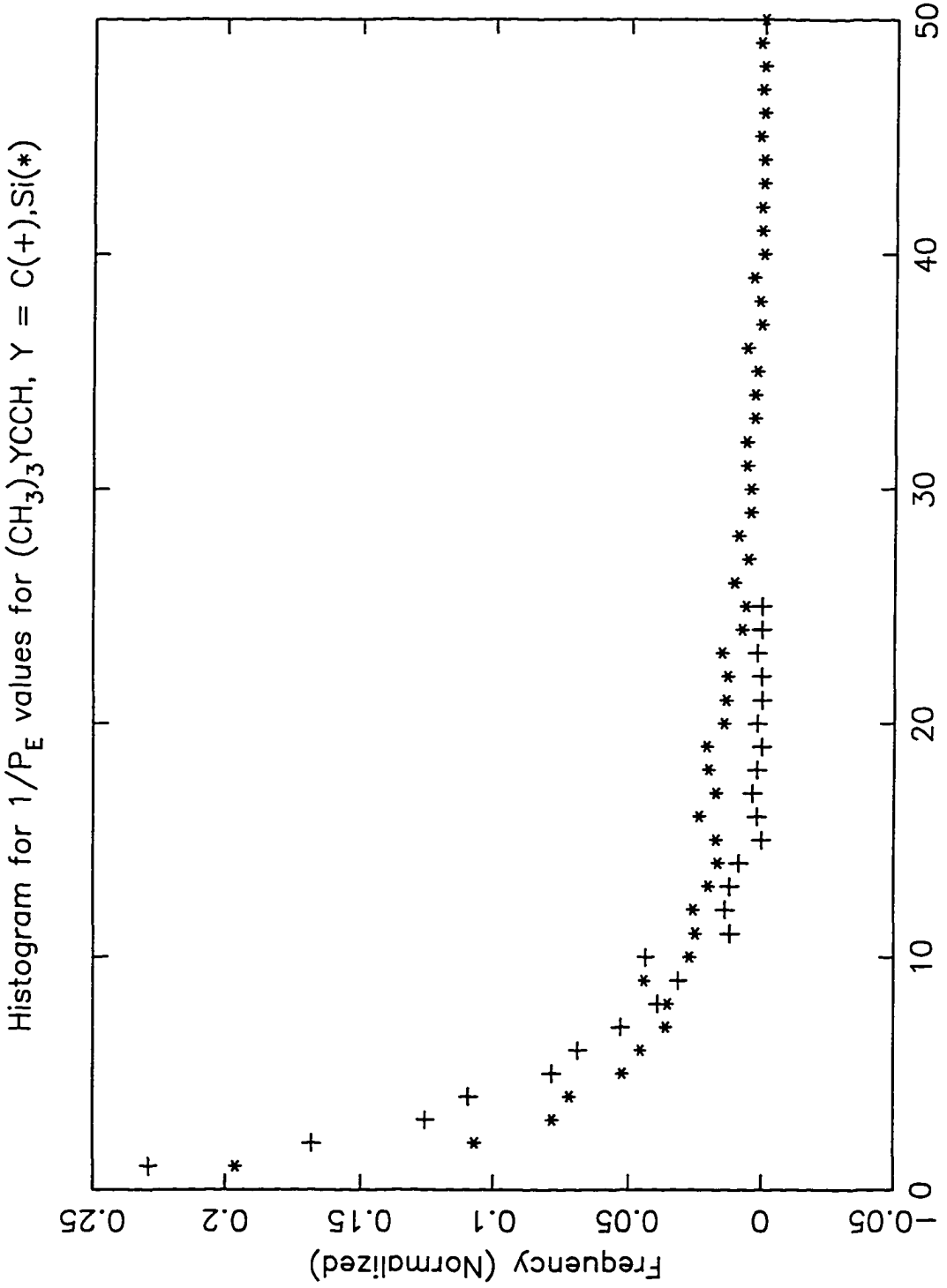
Histogram for 1/P_E values for (CH3)3YCCH, Y = C(+),Si(*)
Frequency (Normalized)
I (1/P_E)
-0.05
0
0.05
0.1
0.15
0.2
0.25
0
10
20
30
40
50

Chapter 3

Inhomogeneous Spectra for the Acetylenic Stretch of $(CH_3)_3SiCCH$

Inhomogeneous spectra for the acetylenic stretch of $(CH_3)_3SiCCH$

Aseem Mehta

Arthur Amos Noyes Laboratory of Chemical Physics,

California Institute of Technology,

Pasadena, CA, 91125

Abstract

Using an assumption of "microcanonical" distribution of energy in an ensemble of vibrationally hot $(CH_3)_3SiCCH$ molecules, the inhomogeneous broadening of these molecules is simulated. This inhomogeneous broadening occurs due to the different values taken by the anharmonic constants x_{ij}. This difference in the x_{ij} values causes the transition frequency for the further excitation of the vibrationally hot molecule to depend on the composition of the vibrationally hot state. Herzberg's formula for the energy levels of symmetric tops is used to calculate a simple approximation of the inhomogeneous broadening.

3.1 Introduction

Broadening of individual lines in vibrational spectra can occur due to homogeneous and inhomogeneous effects. The former term is used to describe the situation when the state formed by the absorption of a short-time light pulse is not an eigenstate of the full Hamiltonian. Anharmonic and other types of couplings can mix this state with other zeroth-order states that are dark as far as the absorption of light from the initial ground state is concerned. Each molecule has the same spectrum. The resulting spectrum can range from a few individual sharp lines to a broad smooth contour where the coupling elements between the states and the density of the coupled states determine the nature of the obtained spectrum. Inhomogeneous effects occur when the molecules have different spectra because of differences in the initial state (there is a thermal distribution at any finite temperature) and due to any differences in the immediate environment. Thus, the initial state is again not a well-defined eigenstate, but is rather a member of an ensemble of states, where the different molecules have their total energy distributed differently among the various modes. In general, absorption spectrum consists of both components – homogeneous and inhomogeneous, depending on the degree of anharmonic mixing (or IVR)[1].

In this communication, we describe the results of simulating the inhomogeneous component of the spectrum in $(CH_3)_3SiCCH$ assuming complete absence of anharmonic mixing that causes IVR. The only intermode interaction was due to x_{ij} anharmonic constants. The experiment that we have tried to simulate is one where some amount of energy E is deposited in the molecule and then the spectrum of the transition of the vibrationally hot molecule is obtained by the excitation of a single mode of the molecule. In this case the distribution of energy in the molecule is assumed to be "microcanonical" with the width of the distribution $\Delta E \ll E$. Such a distribution can be created by saturating the $2\nu_1$ transition as proposed by Lehmann, Scoles and co-workers[2].

3.2 Calculational Details

Using a quadratic force field and some available cubic and quartic force constants in internal coordinates[3], we used the program SPECTRO[4] to nonlinearly transform the internal coordinate force field into one written in terms of normal modes. The anharmonic constants in normal modes ϕ_{ijk} and ϕ_{ijkl} were used in a perturbation theory expression to calculate the x_{ij} values. These values are used in Herzberg's formula[5] for energy levels of symmetric tops. The cubic and quartic values used are given in Table 1. Units for the force constants are consistent with energy being measured in aJ, stretching terms in $\AA$ and bending terms in radians.

Table 3.1: Cubic and quartic terms in internal coordinates used in the generation of x_{ij} values, where, r_1 = ≡C–H; R = C≡C; ρ = Si-C; r_2 = -C–H; β = CCH Force constants are in Å rad units

ijk	f_{ijk}	$ijkl$	f_{ijkl}
$r_1r_1r_1$	-38.0	$r_1r_1r_1r_1$	196.0
RRR	-40.0	RRRR	536.2
$\rho\rho\rho$	-24.5	r_1r_1RR	-1.287
$r_2r_2r_2$	-33.2	$r_1r_1r_1$R	-2.663
r_1r_1R	0.4	r_1RRR	-0.675
r_1RR	-0.193	$r_1r_1\beta\beta$	0.242
$r_1\beta\beta$	-0.202	r_1R$\beta\beta$	-0.025
R$\beta\beta$	-0.802	RR$\beta\beta$	0.137
		$\beta\beta\beta\beta$	1.752

We assumed that molecules in the ensemble had 6050cm^{-1} - 6100cm^{-1} of energy distributed among the various vibrational modes. This energy is the approximate value for $2\nu_1$, the first overtone of the acetylenic C–H stretch transition from the ground state. The inhomogeneous spectrum is then obtained by exciting these molecules with some particular frequencies. For our simulation, the final state was $|v_1+1, v_2, \ldots, v_n\rangle$ where the initial state, $|v_1, v_2, \ldots, v_n\rangle$, is in an energy window of 6050 to 6100cm^{-1}. Using Herzberg's formula for symmetric tops (with l=0), the

transition frequency is

$$\omega_{fi} = \omega_1 + x_{11}(2v_1 + 1 + d_1) + \sum_{k>1} x_{1k}(v_k + \frac{d_k}{2}), \tag{3.1}$$

where, d_i is the degeneracy of the ith mode, and v_i is the number of quanta in the ith mode in the initial state.

Our calculation strategy was as follows. Given all the ω_i values and the x_{ij} matrix, all the different permutations of the quanta in different modes were obtained, such that the state fell within the desired energy window. Once it was established that the state was within the energy window, the transition frequency to the state with one additional quanta in mode ν_1 (acetylenic stretch ≡C–H) was calculated using the above formula. All transitions were given equal transition probabilities and thus the spectrum was obtained by simply plotting the statistical weight of a particular transition against the value of that transition. The spectrum is therefore actually a histogram with bins of 0.1cm^{-1}. The important x_{1k} values are shown in Table 2. Results of the calculations are shown in Figs. 1-5.

Table 3.2: Experimentally[6] and theoretically obtained values for the major x_{1k} constants where ν_1 is the C–H acetylenic stretch

ν_k	x_{1k} theor. (cm^{-1})	x_{1k} experimental (cm^{-1})
C≡C–H bend	21.0	21.0
C≡C stretch	8.0	n/a
Si–C≡C bend	1.68	0.75
Si-C umbrella mode	0.20	0.42

3.3 Analysis of the Spectra

With only a few of the anharmonic constants x_{1j} being large, Table 2, the analysis of the spectrum is quite simple. The peaks that have the highest statistical weight are those which have the initial state without any quanta in the high frequency modes.

This assertion may be proved by simply counting the number of permutations possible. Thus, the peaks with the most statistical weight start from initial states that have $v_1 = 0$. The different peaks in the spectra (given that the number of quanta in ν_1 in the initial state is constant) arise from

$$\Delta\omega_{fi} = \sum_{k>1} x_{1k}\Delta v_k. \tag{3.2}$$

Thus, those modes k which have the largest x_{1k} are responsible for the largest splittings of the inhomogeneous spectra as different numbers of quanta in the kth mode in the initial state lead to different transition frequencies. Most of the x_{1k} values are quite small (0 - 1 cm^{-1}) and they simply serve to broaden each of the peaks. For ν_1 there are only a few modes with substantial x_{1k} values. For example, the value for the interaction of the stretch with the CCH bend is the largest and is $\approx 21cm^{-1}$. This is the origin of the large splittings of about $21cm^{-1}$ that can be seen in the spectrum. Other major off-diagonal terms with mode ν_1 include the C–H stretch/CC stretch ($\approx 8cm^{-1}$), C–H stretch/SiCC bend ($\approx$ 0.75 - 1.6 cm^{-1}) and the C–H stretch/CSiC umbrella mode ($\approx$ 0.2-0.4 cm^{-1}) and are given in Table 1. The inhomogenous spectra obtained with the aforementioned calculational strategy for the experimental and theoretical x_{ij} values are shown in Figs. 1 and 2.

Since there is some uncertainty in the values of the x_{1k}, we have made various calculations with different values for the anharmonic constants. It was interesting to analyze one with the x_{1k} for the C–H stretch/CSiC umbrella mode set equal to zero. The spectra for this calculation are shown in Figs. 3–5. The largest splittings occur for the anharmonic constant of $21cm^{-1}$, as before, with the smaller splittings due the 1.6 cm^{-1} constant. Structure due to quanta in the C≡C stretch can also be seen in Fig. 3 (x_{1k} = 8 cm^{-1}), but the statistical weight here is smaller as this mode is a high frequency mode.

3.4 Concluding Remarks

In this communication, we have described inhomogeneous spectra of absorption of light in the CH acetylenic stretch in $(CH_3)_3SiCCH$ with energy $E \approx 6000cm^{-1}$. Results are shown in Figs. 1-5. In the simulation, a complete absence of anharmonic mixing of anharmonic modes leading to IVR was assumed. We expect that the "real" spectrum will be different due to some effect of intramolecular vibrational energy exchange. It was shown by Stuchbrukhov and co-workers[1] that IVR results in the collapse of the inhomogeneous width by a mechanism similar to "motional narrowing." Thus, we may expect the spectrum to be narrowed by IVR. Perhaps each of the band corresponding to different number of quanta in the CCH bend (bands separated by $21cm^{-1}$) will be narrowed to some extent, however the complete collapse of the whole spectrum into one band is unlikely.

Bibliography

[1] A. A. Stuchebrukhov, S. I. Ionov, and V. S. Letokhov, J. Phys. Chem. **93**, 5357 (1989).

[2] K. K. Lehmann, private communication.

[3] G. A. Crowder, Vibration. Spectrosc. **1**, 317 (1991). G. O. Carlisle, G. A. Crowder, Vibration. Spectrosc. **1**, 389 (1992). V. S. Nikitin, M. V. Polyakova, I. I. Baburina, A. V. Belakov, E. T. Bogoardovskii, and V. S. Zavgorodnii, Spectrochimica Acta **46A**, 1669, (1990). W. Ziel, J. Haase, and M. Dakkouri, Disc. Farad. Soc. **47**, 149 (1969). D. L. Duncan, and M. M. Law, J. Molec. Spectrosc. **140**, 13 (1990). W. D. Allen, Y. Yamaguchi, A. G. Császár, D. A. Clabo Jr., R. B. Remington, and H. F. Schaefer III, Chem. Phys. **145**, 427 (1990). M. Challcombe and J. Cioslowski, J. Chem. Phys. **95**, 1064 (1991). W. Schneider and W. Thiel, Chem. Phys. Lett. **157**, 367 (1989).

[4] J. F. Gaw, A. Willets, W. H. Green, and N. C. Handy, in *Advances in Molecular Vibration and Collision Dynamics*, edited by J. M. Bowman (JAP Press, Greenwich, CT, 1990).

[5] G. Herzberg, *Infrared and Raman Spectra, Vol. II* (D. Van Nostrand and Company, Inc., 1945).

[6] K. von Puttkamer, Ph.D. Thesis, ETH Zurich.

Figure Captions

Fig. 1. Spectrum based on a calculation that utilizes all the experimental values (Table 2) including the one for the C–H stretch/C-Si-C umbrella mode. Since the C–H/C≡C value is not available experimentally, a theoretical value (8.0 cm^{-1}) is used.

Fig. 2. Spectrum based on a calculation similar to that for Fig. 1 obtained by using the theoretical values of x_{ij} (Table 2). The C–H stretch/C-Si-C umbrella mode x_{1k} value has been set to 0.42 cm^{-1}.

Fig. 3. Spectrum obtained from a calculation identical to that for Fig. 2, but the C–H stretch/C-Si-C umbrella mode anharmonic constant has been set to zero. This allows the individual peaks due to different number of quanta in the SiCC bend (separated by 1.6 cm^{-1}, the theoretical value for the C–H stretch/SiCC bend anharmonic constant) to be seen.

Fig. 4. Same as Fig. 3, but rescaled so that the difference in the statistical weights of the peaks that arise from $v_1 = 1$ and $v_1 = 0$ is more easily observed.

Fig. 5 Same as Fig. 3, but both the x and the y axes have been rescaled so that the fine structure can be seen. In this figure, the 1.6cm^{-1} splitting of individual peaks can be seen. Also seen, as shoulders to peaks are the lines that arise from quanta in the $C \equiv C$ stretch.

Figure 1

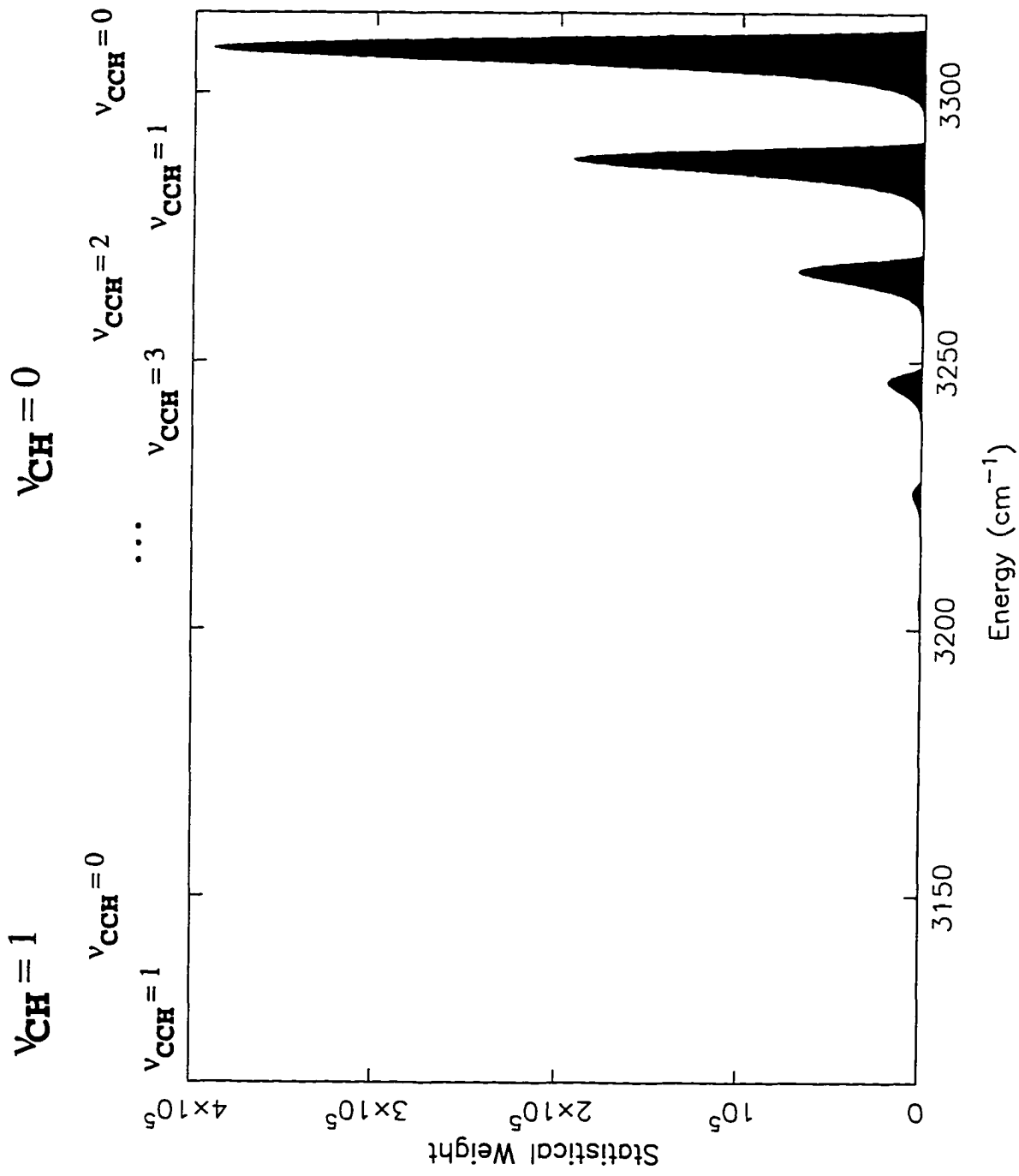
$\nu_{CH} = 1$
$\nu_{CH} = 0$
$\nu_{CCH} = 1$
$\nu_{CCH} = 0$
$\nu_{CCH} = 3$
$\nu_{CCH} = 2$
$\nu_{CCH} = 1$
$\nu_{CCH} = 0$
Statistical Weight
0
10^5
2×10^5
3×10^5
4×10^5
3150
3200
3250
3300
Energy (cm^{-1})

Figure 2

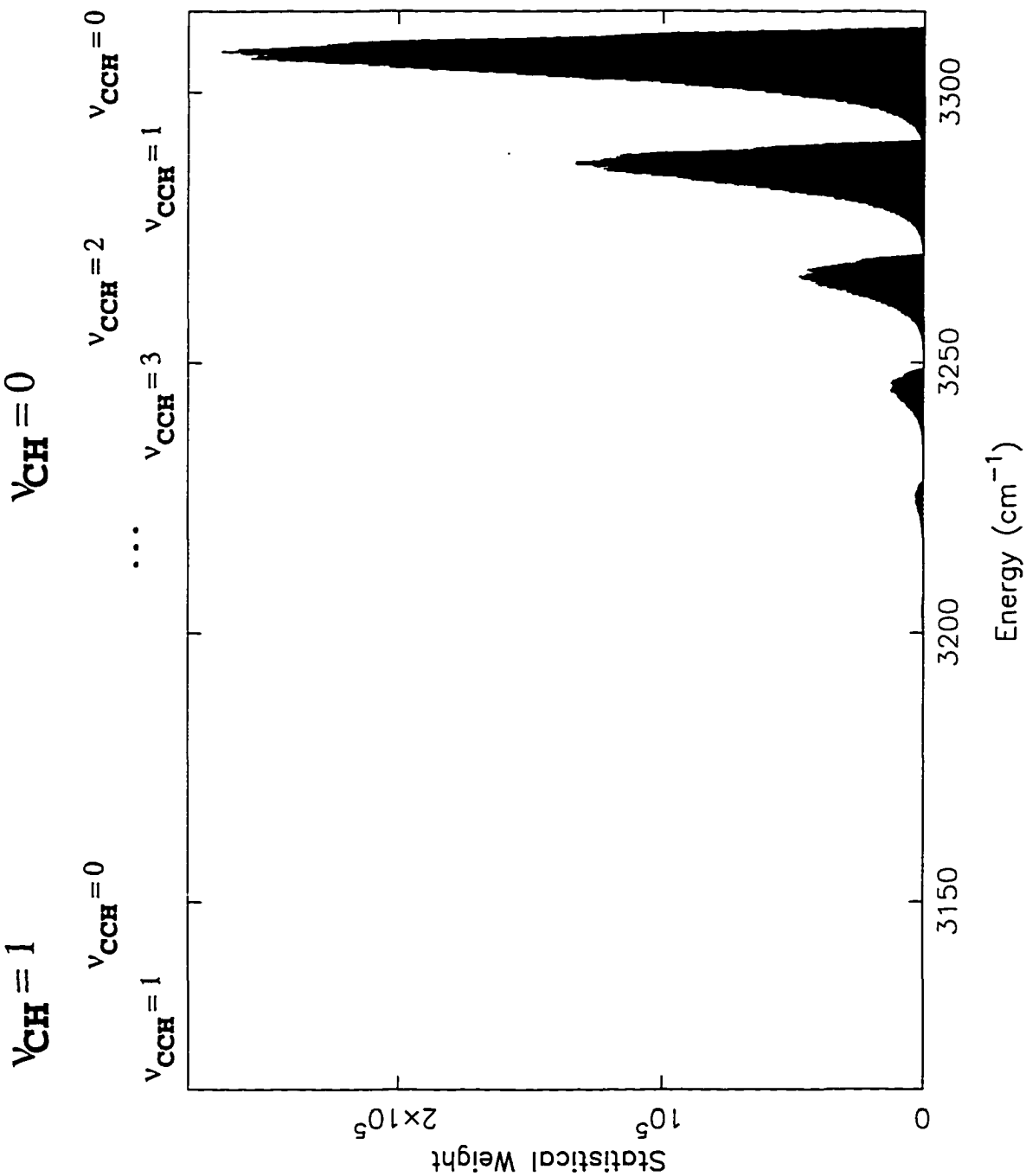
$\nu_{CH} = 1$
$\nu_{CH} = 0$
$\nu_{CCH} = 1$
$\nu_{CCH} = 0$
$\nu_{CCH} = 3$
$\nu_{CCH} = 2$
$\nu_{CCH} = 1$
$\nu_{CCH} = 0$
Statistical Weight
0
10^5
2×10^5
3150
3200
3250
3300
Energy (cm^{-1})

Figure 3

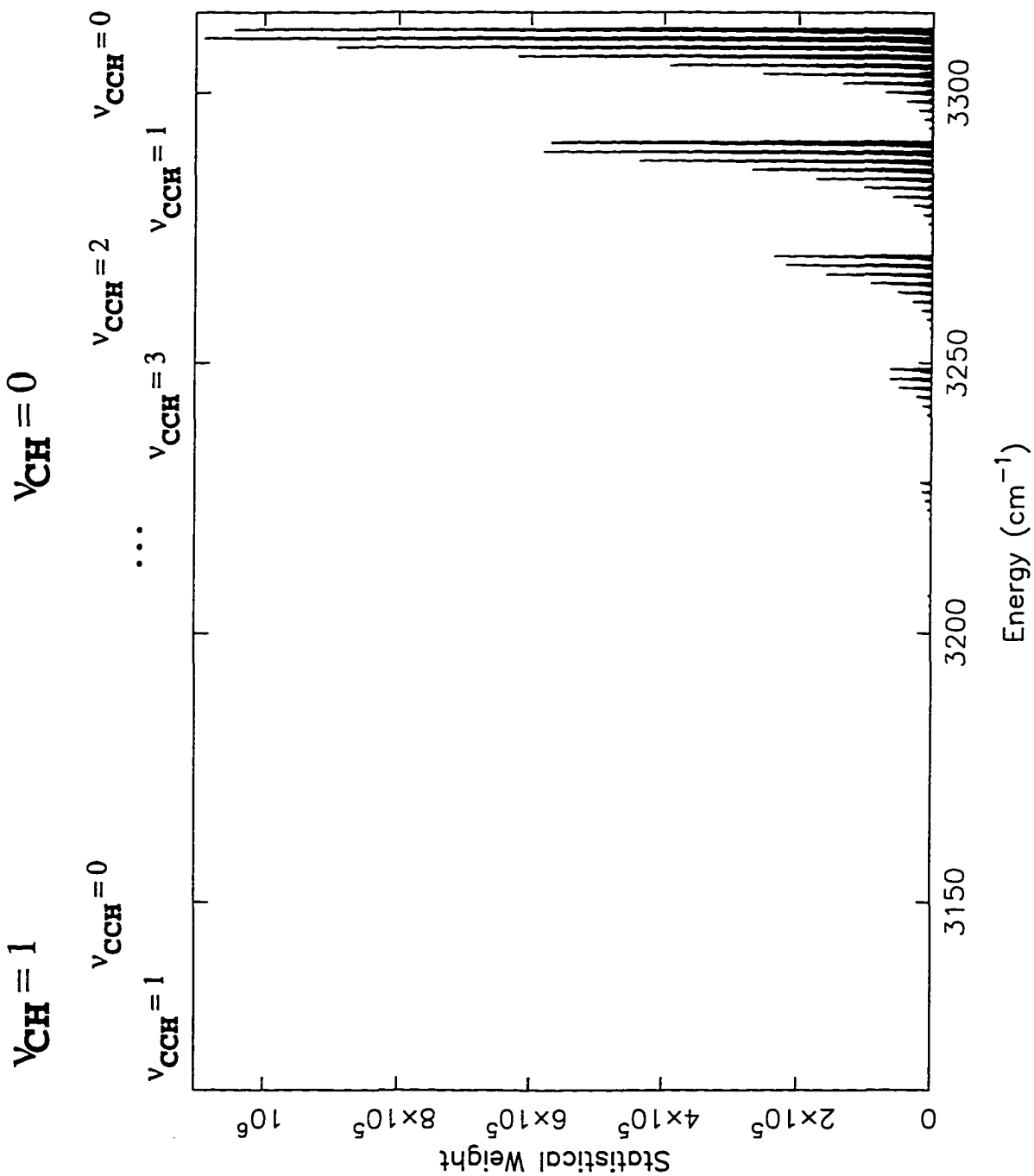
$\nu_{CH} = 1$
$\nu_{CH} = 0$
$\nu_{CCH} = 1$
$\nu_{CCH} = 0$
$\nu_{CCH} = 3$
$\nu_{CCH} = 2$
$\nu_{CCH} = 1$
$\nu_{CCH} = 0$
Statistical Weight
0
2×10^5
4×10^5
6×10^5
8×10^5
10^6
3150
3200
3250
3300
Energy (cm^{-1})

Figure 4

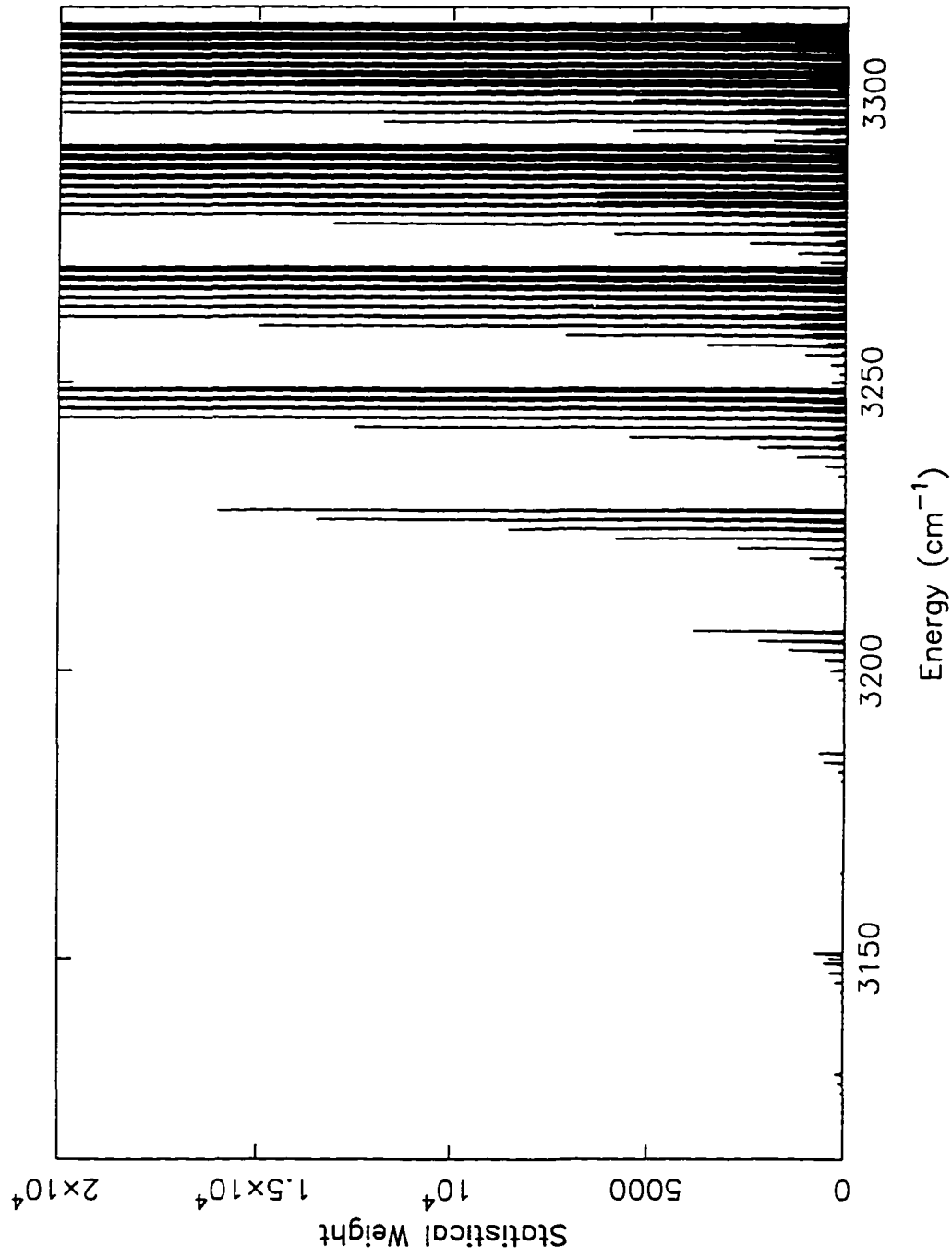
Statistical Weight
0
5000
10^4
1.5×10^4
2×10^4
3150
3200
3250
3300
Energy (cm^{-1})

Figure 5

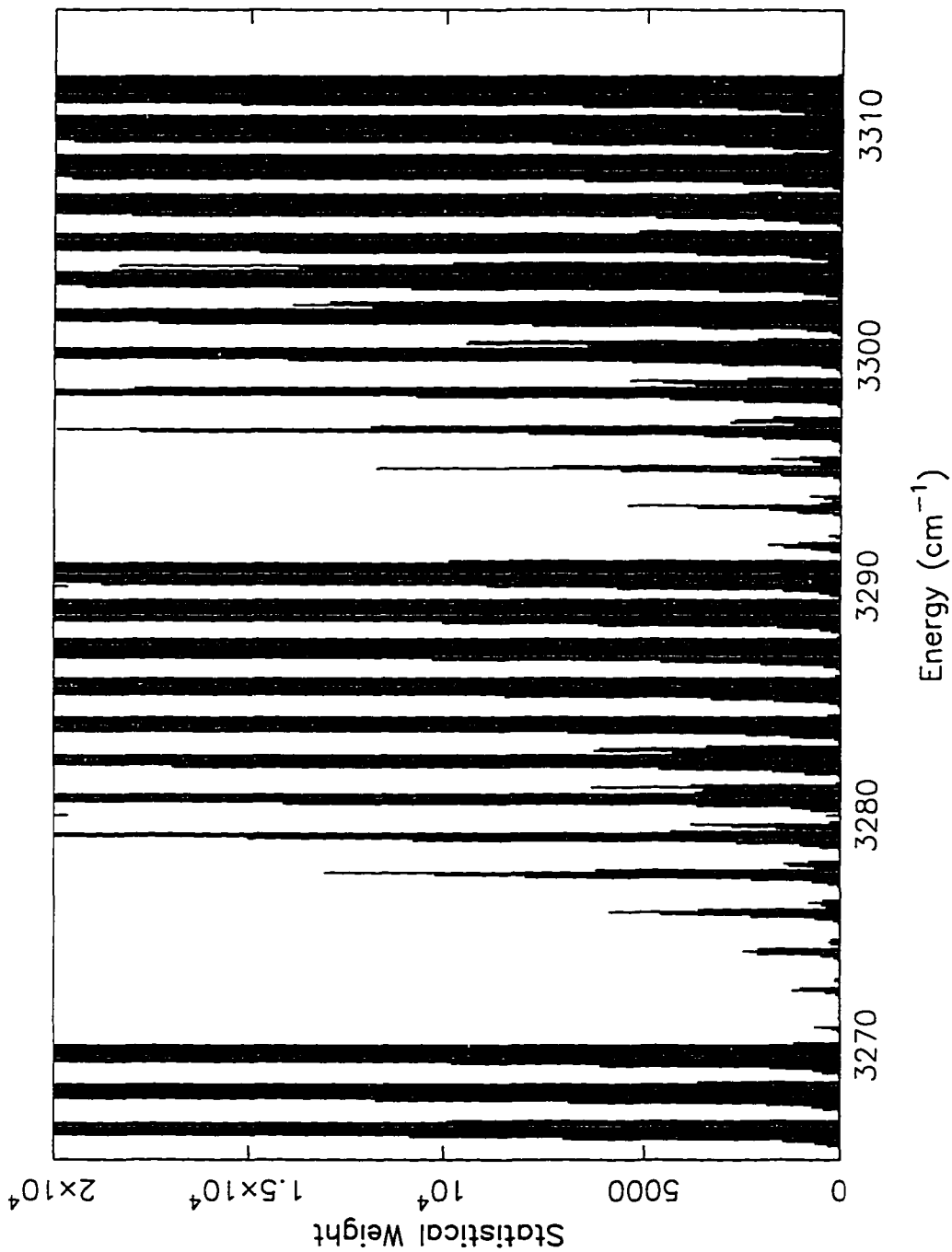
Statistical Weight
0
5000
10^4
1.5×10^4
2×10^4
Energy (cm^{-1})
3270
3280
3290
3300
3310

Chapter 4

IVR in Overtones of the Acetylenic C–H Stretch in Propyne
(Appeared in : J. Phys. Chem. **99**, 2677 (1995))

Reprinted from The Journal of Physical Chemistry, 1995, 99.

IVR in Overtones of the Acetylenic C−H Stretch in Propyne

Aseem Mehta, A. A. Stuchebrukhov,† and R. A. Marcus*

Arthur Amos Noyes Laboratory of Chemical Physics,‡ 127-72, California Institute of Technology, Pasadena, California 91125

Received: October 4, 1994; In Final Form: November 29, 1994®

Quantum calculations are reported for the high-resolution spectra and dynamics of the first and second overtone of the acetylenic C−H stretch (ν_1) in propyne. The calculational method used is similar to that we have used earlier for lower energy states. Lack of low-order Fermi resonances lead to a vibrational superexchange mechanism of decay of the initially populated bright state. The importance of the total density of states and quartic couplings between zeroth-order states is investigated. Comparison with recent experimental results is discussed.

I. Introduction

In previous papers[1,2] we considered the vibrational spectrum and the corresponding intramolecular vibrational relaxation (IVR) of the fundamental and first overtone excitations of the acetylenic C−H stretch in $(CX_3)_3YCCH$ molecules using a tier-structure formalism. In one of the articles,[2] analysis of an approximate molecular Hamiltonian for the acetylenic stretch fundamental excitation in $(CH_3)_3CCCH$ provided a Lorentzian-like line shape, with a fwhm (full width at half-maximum) equal to 0.03 cm^{-1}, in agreement with experimental results. The Fourier transform of the calculated spectrum corresponded to a slow but statistical decay occurring out of the acetylenic stretch fundamental excitation on a time scale of ≈200 ps. The slowness of this decay time might have been considered surprising due to the fact that the density of states for this molecule at the given energy is high.[3] Within the tier formalism with cubic anharmonic couplings in normal coordinates between states in adjacent tiers, the slowness of the relaxation (narrowness of the spectrum) was found to be due to a lack of direct low-order Fermi resonances, leading to a vibrational superexchange (or dynamical tunnelling) mechanism. In the latter the bright state decays into a degenerate vibrational quasicontinuum, mediated by off-resonant virtual transitions. As described in refs 1 and 2, this mechanism may be understood in terms of a tunnelling of trajectories in phase space through a dynamical barrier. In the spectroscopic description, the extensively off-resonant nature of the states directly coupled to the bright state leads to a narrow spectral line.

In the present paper, the methods described in these articles are applied to overtone states in a smaller molecule, propyne (H_3CCCH), prompted by recent experiments.[4,5] Excitations involving the acetylenic C−H (ν_1) stretching modes were studied. The bands analyzed are $2\nu_1$ and $3\nu_1$.

Experimentally, Lehmann, Scoles, and co-workers have investigated the latter of these two bands in a study to explore the spectroscopic differences of nearly pure state $3\nu_1$ and the combination mode $\nu_1 + 2\nu_6$ that has energy already partly distributed.[4] The high-resolution spectra of these bands, incorporating the details of the splitting of a single line due to anharmonic interactions, indicated, in a temporal description, that the rate of relaxation of the $3\nu_1$ state is faster. The difference in the density of states was not considered to be large enough to explain the anomaly, the $3\nu_1$ and $\nu_1 + 2\nu_6$ states being close in energy. The $3\nu_1$ ($J = 0$) state, in a narrow spectral range of 0.1 cm^{-1} studied experimentally, showed several lines, while the $\nu_1 + 2\nu_6$ state in a similar spectral range showed only one line.

Perry and co-workers have investigated the $2\nu_1$ and the nearly isoenergetic $\nu_1 + \nu_6$ bands[5] and found that the spectra of individual J, K states are split. For low K states the splitting is small and the spectrum in each case consists of one major peak surrounded by a few small peaks, each of which has an amplitude of less than 10% of the main peak. The available data hints at a larger number of perturbers for the pure overtone $2\nu_1$ than for the $\nu_1 + \nu_6$ band. In the present paper we present the results for the $2\nu_1$ and the $3\nu_1$ bands.

For the calculated relaxation, our analysis yields a behavior of the $2\nu_1$ and $3\nu_1$ states that follows a vibrational superexchange mechanism, due to the lack of low-order Fermi resonances. The decay is governed, thereby, by the few directly coupled off-resonant states that provide virtual couplings.

The calculated IVR characteristics are quite different at the two energy scales. At the lower energy, about 6000 cm^{-1}, we find the beginnings of some perturbations to the regular spectra due to interactions with bath states. However, the energy is still mainly localized in the bright state. On the other hand, at about 9500 cm^{-1}, there are available to the bright state a large enough number of quasi-resonant states such that real statistical IVR can occur leading to irreversible decay (modulated by some quantum beats) of population out of the bright state.

II. Tier Model

The tier model has been described elsewhere.[1] The Hamiltonian is written in normal mode coordinates as

$$H = \frac{1}{2}\sum_i \omega_i(q_i^2 + p_i^2) + \frac{1}{3!}\sum_{ijk}\phi_{ijk}q_iq_jq_k + \frac{1}{4!}\sum_{ijkl}\phi_{ijkl}q_iq_jq_kq_l + \dots \quad (1)$$

The energy of each of the zeroth-order states in the basis set is calculated using the expression[6]

$$E(v_1,v_2,\dots,v_n) - E_{ZPE} = \sum_i \omega_i v_i + \sum_i\sum_{k\geq i} x_{ik}\left(v_iv_k + \frac{v_kd_i}{2} + \frac{v_id_k}{2}\right) \quad (2)$$

where d_i is the degeneracy of the ith mode. The intermode coupling is due to nondiagonal anharmonic terms in eq 1.

† Permanent address: Department of Chemistry, University of California, Davis, CA 95616.
‡ Contribution No. 8991.
® Abstract published in *Advance ACS Abstracts*, February 1, 1995.

0022-3654/95/2099-2677$09.00/0

TABLE 1: Limited Number of Cubic and Quartic Force Constants in Internal Coordinates for Propyne Included in the Nonlinear Transformation into Normal Coordinates[a]

ijk	f_{ijk}	ref	$ijkl$	f_{ijkl}	ref
$S_3S_3S_3$	−38.35	10	$S_3S_3S_3S_3$	196.0	10
$S_4S_4S_4$	−109.23	10	$S_4S_4S_4S_4$	536.2	10
$S_3S_3S_4$	0.40	10	$S_3S_3S_4S_4$	−1.287	10
$S_3S_4S_4$	−0.193	10	$S_3S_3S_3S_4$	−2.663	10
$S_3S_{10}S_{10}$	−0.202	10	$S_3S_4S_4S_4$	−0.675	10
$S_4S_{10}S_{10}$	−0.802	10	$S_3S_3S_{10}S_{10}$	0.242	10
$S_3S_3S_3$	−26.50	11	$S_3S_4S_{10}S_{10}$	−0.025	10
$S_1S_1S_1$	−18.67	12	$S_4S_4S_{10}S_{10}$	0.137	10
$S_6S_6S_6$	−12.70	12	$S_{10}S_{10}S_{10}S_{10}$	1.752	10
$S_1S_7S_7$	−0.33	12	$S_1S_1S_1S_1$	50.0	12
$S_6S_7S_7$	−0.29	12	$S_6S_6S_6S_6$	75.0	12
$S_7S_7S_7$	−0.18	12	$S_1S_1S_6S_6$	52.0	12
$S_1S_6S_6$	−16.56	12	$S_1S_6S_6S_6$	37.0	12

[a] S_i are symmetric internal coordinates as defined by Duncan in ref. 9. Force constants are in Å rad units.

The nondiagonal anharmonicity terms $q_iq_jq_k$ couple different zeroth-order states in the Hamiltonian and are written in terms of creation and annihilation operators. Starting with the bright state, and with the ϕ_{ijk} values available, the $q_iq_jq_k$ operators are used to generate states in further tiers. The states are kept within specified energy windows, and they are accepted or rejected on the basis of an artificial intelligence (AI) search method. This search method is used to select the states that are important in the relaxation while keeping the problem computationally tractable. States that are highly detuned in energy from the bright state or are coupled with a small matrix element do not contribute to the relaxation and are discarded during the AI search using an evaluation function that has been described in ref 1.

The anharmonic constants ϕ_{ijk} in eq 1 are obtained by the transformation of empirical force fields in internal coordinates[7] into normal coordinates. These empirical force constants (in internal coordinates) are transformed nonlinearly into normal coordinates using the software package due to Handy and coworkers (SPECTRO).[8]

The empirical anharmonic force field used for these calculations is the quartic force field in internal symmetry coordinates from refs 9−12. The quadratic part of the force field from ref 9 was fit to some approximations of the harmonic frequencies (ω_i's) rather than the energies of the fundamental transitions. The quadratic force field and the most important (and available) cubic and quartic force constants (Table 1) were used as input into the routine SPECTRO. The latter nonlinearly transforms the internal coordinate force field into a normal coordinate force field and calculates, by a perturbation theory expression, the (3N-6)(3N-6) anharmonic constant matrix x_{ij}. These constants are used to calculate the energy of each state in eq 2. The calculated ϕ_{ijk} values are used to evaluate the coupling terms between zeroth-order states in adjacent tiers. We note again that the wave functions of the zeroth-order states were those of a multidimensional harmonic oscillator, but their energies were corrected using eq 2.

A Morse oscillator function for the C−H acetylenic stretch has also been used by some investigators in their calculations. We calculated the matrix elements between zeroth-order states using Morse wave function selection rules and found that even at the $3\nu_1$ level (9500 cm^{-1}; D_e(≡C−H) ≈ 35 000 cm^{-1}) the zeroth-order wave function can be well approximated by a harmonic oscillator without the introduction of significant error (≤10%, typically). Therefore, all the calculations reported used harmonic oscillator basis functions. The energies of the zeroth-order states were however, obtained from eq 2.

Due to the tractable size of the molecule, an *ab initio* calculation of propyne was also performed with Gaussian 92.[13] This calculation, with a 6-31G* basis set at the restricted Hartree−Fock level, generated quadratic and cubic force constants in Cartesian coordinates. These constants were transformed linearly into the normal-coordinate-based ϕ_{ijk} values. The latter were, in turn, used to couple the harmonic oscillator zeroth-order states. The cubic force constants obtained from *ab initio* calculations are complete at the given level of theory and can be used as an approximate test of the force field in internal coordinates that (at cubic and higher levels) had been cobbled together from various sources. The latter pieced-together force field is necessarily incomplete since all the cubic internal coordinate force constants are not known. The *ab initio* force field was used only as a qualitative check on the empirical force field. The results presented in this paper are all from the empirical force field.

Due to the higher energy ($E(v)$-E_{ZPE} ≈ 6000 or 9000 cm^{-1}) of the states analyzed, when compared with our study of the fundamental stretch in $(CH_3)_3CCCH$ ($E(v)$-E_{ZPE} ≈ 3000 cm^{-1}), we have found that some quartic couplings have to be included if the model is to realistically model the actual physical process. This point is elaborated upon later. There are numerous unknown or only crudely estimatable quartic force constants ϕ_{ijkl}. We have included their effect in the tier structure in an approximate way by assigning a coupling element, chosen as indicated below, to the coupling of states $|i\rangle$ and $|j\rangle$ in tiers differing by two (e.g., tier n and tier n + 2) if the quantity η_{ij}, defined by

$$\eta_{ij} = \sum_k |v_k^i - v_k^j| \tag{3}$$

is less than or equal to 4. Here, v_k^i is the number of quanta in the kth oscillator of the ith state.

It should be the noted that the terms coupling states in adjacent tiers (also referred to as matrix elements since they are the off-diagonal terms in the vibrational Hamiltonian) differ from the matrix element term used in some of the experimental papers. The latter arise in the Lawrance−Knight[14] deconvolutions of spectra and are approximately related to the superexchange matrix element $\langle 0|V|k\rangle$ in the present formalism via a perturbation-theory-based expression such as

$$\langle 0|V|k\rangle \sim V_{01}\frac{V_{12}}{\Delta E_{12}}\cdots\frac{V_{k-1,k}}{\Delta E_{k-1,k}} \tag{4}$$

there being a sum over the various superexchange paths connecting $|0\rangle$ and $|k\rangle$. There is, of course, a large difference in the magnitude between the superexchange "matrix elements" $\langle 0|V|k\rangle$ when compared with the values of V_{01}, V_{12}, etc.

The importance of including a final tier with a high density of states (when a high density of states exists for the given molecule at the energy in question as in propyne at 9000 cm^{-1}), so as to approximate the real total density of states of the dark states, was established in ref 2. We make the same addition here in the calculations. The total number of added states that model the quasi-continuum vary from 600 to 1000 in an energy window of 3−5 cm^{-1}, such that the total density of states is approximately 200/cm^{-1}. The latter is slightly higher than the density of states estimated for propyne (150/cm^{-1}) with the correct symmetry at the specified energy (≈9000 cm^{-1}). The slightly higher value is used because the interaction of the states in the finite final tier with the previous tiers leads to the repulsion of some of the final tier states into a larger window. The matrix element with which these final tier states are coupled to states

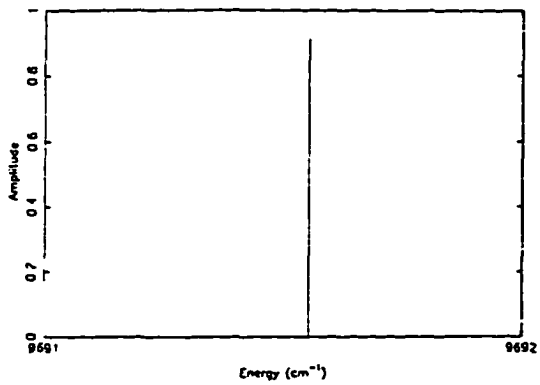

Figure 1. Spectrum corresponding to the $3\nu_1$ band for CH_3CCH. No quartic couplings or final tier of dense states is added.

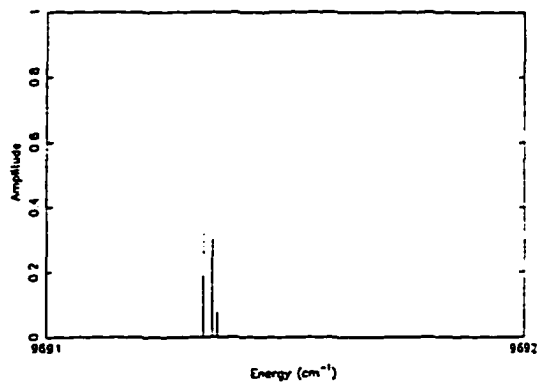

Figure 2. Spectrum corresponding to the $3\nu_1$ band for CH_3CCH showing the transformation (from Figure 1) due to the final tier of resonant states and quartic couplings.

in the previous tier is estimated from the average cubic coupling between states in previous tiers. Each state in the final tier is coupled to a single state in the previous tier.

The states in the final tier are placed randomly, and the robustness of the calculation with respect to this random placement and to the approximate magnitudes of the quartic coupling values is explored below, where some typical results are given.

III. Results

3.1. $3\nu_1$. *a. No Quasi-Continuum.* With the above algorithm for generating the sequentially coupled model with a given bright state, the tier structure was generated with the bright state containing three quanta of energy in the acetylenic C−H stretch. The pure normal mode wave function of the zeroth-order bright state is denoted by $|\phi_0\rangle$, with its energy having been corrected using eq 2. Experimentally, about five peaks were observed in an energy window of approximately 0.1 cm^{-1} (for $J' = 0$). This number corresponds to at least a minimum of 50 states/cm^{-1} coupled well with the bright state, since some peaks may have been in the signal/noise background and so not observed. This density of states of 50/cm^{-1} is on the same order as the calculated total density of vibrational states (150/cm^{-1}) with the correct symmetry.[4] Using the previously described AI search method, a total of 1048 "well-coupled" states in 10 tiers were selected within a large energy window of 500 cm^{-1} for each tier. Diagonalization of this vibrational Hamiltonian with only cubic couplings resulted in a spectrum,

$$\begin{aligned} I(\omega) &= \sum |\langle \psi^{\text{init}} | \mu | \psi_i \rangle|^2 \delta(\omega - E_i) \\ &= \sum |\langle \psi^{\text{init}} | \mu | \phi_0 \rangle|^2 |\langle \phi_0 | \psi_i \rangle|^2 \delta(\omega - E_i) \\ &= c \sum_i^N |\langle \phi_0 | \psi_i \rangle|^2 \delta(\omega - E_i) \end{aligned} \quad (5)$$

dominated by only one peak (Figure 1), for which $\langle \phi_0 | \psi_i \rangle^2 \approx 0.9$, for some i. Here the $|\psi_i\rangle$ form a complete set of eigenfunctions and c is a constant. In deriving eq 5, we have assumed that there is only one zeroth-order state, $|\phi_0\rangle$ (the bright state), that has a nonzero matrix element of the type $\langle \phi_0 | \mu | \psi^{\text{init}} \rangle$, where μ is the dipole moment operator and $|\psi^{\text{init}}\rangle$ is the initial vibrational state (experimentally, it had one quantum in ν_1).

b. Quasi-Continuum Added. To simulate the presence of the high density of nearly degenerate states that are well separated in phase space from the bright state, a single, dense tier of quasi-degenerate states was then added to the final (here, tenth) tier with a density of states such that the total density of states approximates the actual value. One thousand states, randomly placed in a window of size 5 cm^{-1}, were coupled to states in the tenth tier with matrix elements estimated from the average matrix elements in previous tiers. This addition of a quasicontinuum yielded no observable change in the spectrum, *i.e.* yielded a spectrum similar to Figure 1.

c. Addition of Quartic Terms. Upon the inclusion of small quartic terms that couple the states in the manner described above (by the calculation of η_{ij}) and without the addition of the final dense tier of states, the amplitude of the major peak diminished slightly (to 0.75), with the remaining amplitude being distributed over spectral lines in a large energy range (≈100 cm^{-1}). When the final tier of states was added to this cubic- and quartic-coupled Hamiltonian, the spectrum was transformed from one where there is a single dominant peak to a more fractionated type (Figure 2). The single peak of previous calculations split into a few (three to six) "major" peaks within an energy range of 0.07−0.15 cm^{-1}. The details of the calculated spectrum, however, depended upon the particular random choice of the energies and the coupling terms of the states in the final tier.

d. Time-Dependent Behavior. It is useful to compare the autocorrelation functions of the spectra (survival probability $p_0(t)$ of the bright state) with and without the extra tier present and with and without quartic couplings:

$$\begin{aligned} p_0(t) &= |\langle \phi_0 | \phi(t) \rangle|^2 \\ &= |\sum_i^N |\langle \phi_0 | \psi_i \rangle|^2 e^{-iE_i t}|^2 \end{aligned} \quad (6)$$

where $\phi(t)$ is the wave function at time t which evolves from ϕ_0 ($p_0(0)$ is unity). The right-hand side of eq 6 is proportional to $|\int_{-\infty}^{\infty} I(\omega) e^{-i\omega t} d\omega|^2$, where $I(\omega)$ is given by eq 5. As indicated by the spectrum (which is dominated by a single peak of ≈0.9, of which the autocorrelation function is the Fourier transform), $p_0(t)$ remains constant for a time of up to 1 ns at a high value (0.8−0.9) when only cubic couplings are utilized. The same type of result is obtained upon the addition of the final dense tier of states. With the inclusion of quartic couplings but without the extra tier, the survival probability shows instead a rapid oscillatory decay to ≈0.6 on a femtosecond time scale (Figure 3), because of the few well-coupled nonresonant states in the initial tiers, due to direct cubic and quartic couplings. It then remains highly oscillatory and, on average, constant.

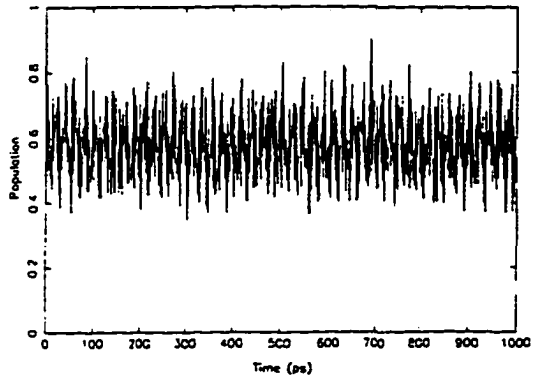

Figure 3. Survival probability (of the bright state) when quartic couplings are utilized without the final tier.

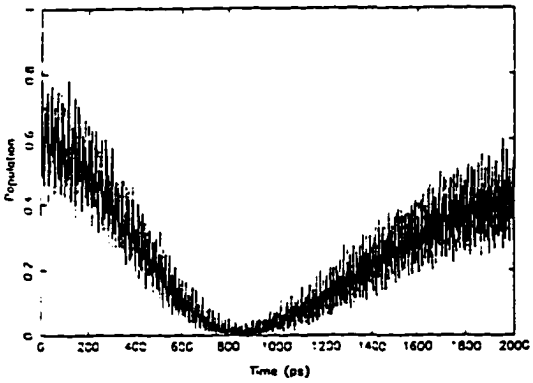

Figure 4. Survival probability corresponding to spectrum in Figure 2.

Upon the addition of the extra tier to simulate the actual presence of the quasi-continuum, the high-frequency oscillatory behavior is accompanied by smooth decay of the population into the quasi-continuum (Figure 4). The time scale of this decay is a few (two to six) hundreds of picoseconds.

Dynamically, therefore, the addition of the quartic couplings, but no quasi-continuum, changes the autocorrelation function from essentially no decay into one where there is fast femtosecond time scale decay of the autocorrelation function to about $\approx$0.6, which then, on average, remains constant but is accompanied by a large number of high-frequency components. Addition of the final tier of dense states causes real decay to occur. This finding confirms our previous conclusion that the fine structure and the irreversible relaxation of the first several overtones are due to the very high-order superexchange anharmonic couplings.

From the spectral viewpoint, the high-frequency components of the autocorrelation function, which dominate the subpicosecond dynamics, appear as small peaks far detuned from the main peak. These spectral components that are detuned from the main peak appear due to the presence of a few nonresonant states in the initial tiers that are well coupled to the bright state, which also cause the subpicosecond decay of the autocorrelation function to $\approx$0.6. Experimentally, they might be very difficult to resolve due to their large distance from the main peaks as well as signal-to-noise limitations. There is, however, no reason for them not to occur. The smooth but not single-exponential decay appears spectrally as the splitting of the main peak into a few reasonably strong peaks within a small energy window.

e. Robustness of the Calculation. We have examined the robustness of the calculation. The quartic coupling constants were added as a random coupling between 0 and some approximate maximum value. In the final dense tier of states, the energies of the states were random within a given energy window. The matrix elements coupling states in the final dense tier with the previous tier were also random between 0 and various maximum values ($V_{max} = 5-30$ cm^{-1}). In Figure 5, results are presented from simulations with different random realizations of these values. The figure shows that while the details of each calculation may differ, the physically relevant picture of splitting of the main peak into a few peaks within an energy range of about 0.1 cm^{-1} remains unchanged. In Table 2, we present some statistics about each of the five spectra that have been presented in Figures 2 and 5. The numbers presented are quite representative. The quantity Γ in Table 2 is defined by

$$\Gamma^2 = \frac{\sum_i p_i(\nu_i - \bar{\nu})^2}{\sum_i p_i} \tag{7}$$

where $\bar{\nu} = \sum p_i\nu_i/\sum p_i$, and $p_i = |\langle\phi_0|\psi_i\rangle|^2$. These statistics have been calculated not over the whole spectrum (in which case the denominator in eq 7 would have been unity) but over a small window that includes just the main clump of peaks in the figures. Also in Table 2, we present the number of major components in the spectra, where a component is considered major if $|\langle\phi_0|\psi_i\rangle|^2 \geq 0.005$, which is about 1–2% of the major peak. The window in Table 2 refers to the energy range in which these major components occur.

These results are qualitatively similar when the statistics of different spectra are compared but there is enough scatter in the data that no quantitative judgements can be made. Γ can be considered to be a rough estimate of the discrete counterpart of the fwhm and the calculated values of a few hundred megahertz are in agreement with experimental values for such molecules.[3]

3.2. $2\nu_1$. The Hamiltonian matrix of the tier structure was generated utilizing the algorithm described above. The energy window for each of the 10 tiers is 500 cm^{-1}, and 437 well-coupled zeroth-order states form the basis set. Diagonalization of this Hamiltonian matrix with only cubic couplings resulted in a spectrum for which the amplitude of one of the peaks was greater than 0.999. Upon relaxing the AI criterion for state selection, a larger Hamiltonian matrix with 1317 basis set states was also analyzed with no change in the spectrum. This result indicates that the scheme of selecting only the most important states has captured all the physically relevant details of the spectrum as far as the cubic couplings are concerned. The complete dominance of a single peak in the spectrum shows that there is no interaction of the bright state with the bath states in the cubic Hamiltonian. Upon the addition of small phenomenological quartic couplings between states separated by one tier as described above and the addition of a final tier of states with the appropriate density of states we find that the main peak split slightly. However, the spectrum was still dominated by a single peak that had an amplitude of 0.9. The rest of the amplitude was distributed in weak daughter peaks around the main peak. Also, there were some peaks detuned more than a tenth of a wavenumber due to the direct quartic couplings. In Figure 6 we give a typical example of the slight splitting that occurs due to the quartic couplings and the final tier (note the considerably expanded, logarithmic, scale).

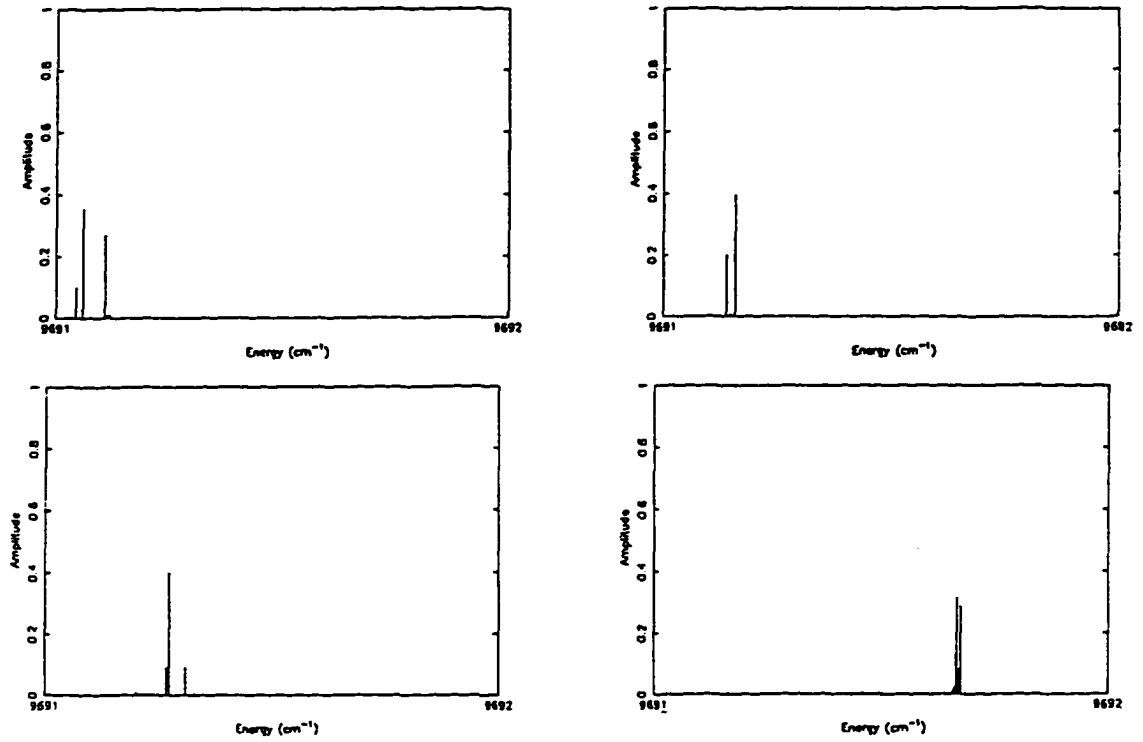

Figure 5. Spectra corresponding to the $3\nu_1$ band for CH_3CCH with different random realizations of the final tier of resonant states and quartic couplings.

TABLE 2: Statistical Properties of the Spectra in Figures 2 and 5

	$\bar{\nu}$	Γ (cm^{-1})	Γ (MHz)	no. of components	window (cm^{-1})
1	9691.33	0.013	402	5	0.07
2	9691.07	0.029	774	9	0.07
3	9691.16	0.009	255	5	0.02
4	9691.27	0.021	639	6	0.13
5	9691.67	0.010	285	6	0.02

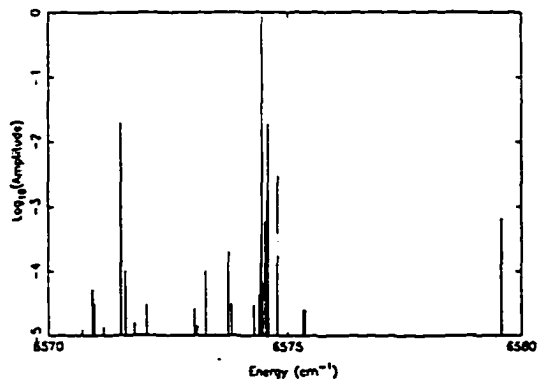

Figure 6. Spectrum typical of the $2\nu_1$ band with quartic couplings. Note the log scale for the ordinate.

IV. Discussion

4.1. $3\nu_1$. The first result to be considered is that the pure cubic Hamiltonian without the final tier does not result in any splitting of the individual spectral line. This result is not surprising since a near degeneracy of two or more states is needed, as a necessary though not sufficient condition, to distribute the intensity of the bright state among two or more major peaks, and the density of states for that calculation is far lower than the real value. For this first result the density of states was approximately 2/cm^{-1}, compared with the actual value of 150/cm^{-1}. Similar results have been obtained for other calculations modeling the excitation of the acetylenic stretch in different molecules.[2] However, unlike the situation in *tert*-butylacetylene where the addition of an extra tier for the fundamental C−H stretch causes the single line to have a Lorentzian line shape,[2] the final tier (with a density of states appropriate to the $3\nu_1$ excitation energy in propyne) did not affect the spectrum. The total superexchange coupling of the bright state to the dense (phenomenological) tier was therefore so small that the states in the dense tier remained, in effect, uncoupled to the bright state.

Indeed, it has been shown previously[2] that while the presence of the total density of states in the tiers is a necessary condition for calculations to correctly simulate statistical or near-statistical IVR behavior, it is not a sufficient condition. Equally important is the correct description of the initial tiers as they govern the overall decay. It may be recalled that the lifetimes of various different initial states can be inferred from the analysis of only a few initial tiers.[1] Here, the above mentioned results regarding the spectrum indicate that a correct description of the IVR of this bright state (at a higher energy than the states previously analyzed) requires the inclusion of terms higher than cubic in the Hamiltonian. In this way the superexchange matrix element to the states separated by a large distance in tier space will be larger. The next higher order of coupling beyond cubic consists of the quartic terms in the Hamiltonian. The procedure used to include such terms was described in a previous section. We note that the basis set initially used for the cubic couplings

remains the same when the quartic couplings are introduced. The states in tier n that can be coupled to states in tiers $n + 2$ via terms of the type $q_l q_l q_k q_l$ are assigned an off-diagonal matrix element.

The importance of including quartic couplings for intramolecular dynamics of overtone states was observed previously by Zhang and Marcus.[15] We next sketch how the inclusion of the quartic terms in the Hamiltonian can significantly increase the total coupling of overtone bright state. If the couplings are limited to third order, then the coupling between the bright state and the first tier is similar for ν_1, $2\nu_1$, and $3\nu_1$ since the *only* cubic coupling terms possible will annihilate one quantum of ν_1 (which is the highest energy oscillator) and create two others such that $\nu_l \approx \nu_i + \nu_j$. The matrix elements that couple the bright state to the first tier for the fundamental as compared to the different overtone bands differ by a small multiplicative constant, due to the selection rules for harmonic oscillator wave functions. However, the number of states in the first tier and the approximate detuning of those states is roughly independent of whether the bright state is the fundamental band or an overtone. Consideration of higher order couplings modifies this picture. For the overtone states, application of the $q_l q_l q_l q_k$ and $q_l q_l q_l q_k q_l$ type of operators upon the bright state creates the additional couplings of fourth and fifth order, respectively, since more than one quantum in the initially excited state is available for annihilation. These quartic and quintic couplings have no effect on the bright state in the fundamental band, but their presence in the overtone bands significantly increases the overall coupling of the bright state to the bath and increases, thereby, also the superexchange matrix elements to the dense tier of states since, at the higher energies, states with some negative Δv's can be coupled. These facts describe one role for quartic couplings in the calculations attempted for states at higher energies. Although a realistic modeling of the fundamentals in other molecules was possible when only the cubic couplings were included,[1,2] the present results show that, when higher energy states are considered, the use of only the cubic couplings underestimates the superexchange coupling of the bright state to the states in distant tiers. The increasing importance with energy of such higher order couplings or, in other words, the poorer pure cubic coupling picture of IVR is, therefore, indicated.

We consider next the small peaks that appear detuned to a relatively larger extent in energy in the spectra upon the addition of these quartic couplings. Upon the addition of the quartic constants, the spectrum dominated by a single peak splits to form some small peaks over a large energy window with most of the amplitude still being in the main peak. This result signifies that the coupling of the bright state to the states in the initial tiers has increased. As mentioned earlier, it is these couplings that control the total coupling of the bright state with the near-degenerate states that are separated in phase space. That the addition of the quartic couplings significantly increases this superexchange coupling is measured directly when a final tier of states is added along with the quartic couplings. Unlike the previous result, where without quartic terms the final tier made no difference, this time the single peak splits into a few peaks (Figures 2 and 5). The small peaks are due to the direct (and weak) coupling of the bright state with states in the initial tiers that are usually highly detuned. Experimentally these peaks have not been identified, since they appear on a energy scale greater than the scale investigated experimentally, 1−2 cm^{-1}, and their calculated intensity is small. Such small peaks in the wings have also been identified in calculations and discussed by Gruebele and co-workers.[16]

Although the approximations inherent in the present model calculations preclude a one-to-one correspondence of the peaks in the experimental and theoretical spectra, there is a qualitative similarity between them, both in the number of peaks and in the approximate energy range (0.1 cm^{-1}) over which they appear. The autocorrelation function shows a lifetime on the order of 300 ps. The mechanism that governs the physical process is again a vibrational superexchange coupling mechanism. This long smooth decay in Figure 4 is typical of the calculated relaxation of acetylenic stretches even though recurrences are not precluded. It may be recalled that one of the features of the acetylenic C−H stretch fundamentals and overtones was the absence of any direct low-order resonance.[1,2] The states in the initial tiers were mostly all off-resonant and provided a virtual state mechanism (superexchange) for transition into the resonant states that were well separated in the phase (or quantum number) space of the molecule.

4.2. Other Spectral Bands. Due to the smaller density of available states at the given energy, the calculated spectra are mainly dominated by a single peak with some small daughter peaks arising due to quartic couplings. The final tier of states does not play a major role in the IVR. This IVR is not statistical and may be considered at the beginning of the intermediate stage. The results for the $\nu_1 + 2\nu_6$ band are not adequately treated by the present formulation, which should be regarded as a first step. For this band, and for $3\nu_1$, a more elaborate treatment would omit the x_{ij} terms and use, instead, a more elaborate force field and, perhaps, include vibration−rotation couplings.

V. Conclusion

We have calculated the spectral features of the first and second overtones of the acetylenic C−H stretch in propyne that arise from the anharmonic coupling between harmonic zeroth-order states. The energy and the couplings of the basis states are calculated from an empirical potential energy function.

We find that due to a lack of direct Fermi resonances, the C−H stretch decays into the dark vibrational states by utilizing the low-order off-resonant states that are available. Our results are qualitatively similar to the experimental ones. We show that the inclusion in the potential of terms higher than cubic is necessary for a correct representation of the spectrum. The calculations show that the initial couplings of the two bright states are both off-resonant in nature and provide the virtual couplings to available near-resonant states. Upon the inclusion of a final tier of states with the appropriate density of states, we find that the first overtone remains spectrally pure with one dominant component, whereas the second overtone spectrum consists of a few major components due to the availability of a higher density of states. In a temporal description, the presence of a higher density of states in the second overtone allows for the initially excited state to decay statistically, whereas the initial excitation remains more localized in the first overtone.

Acknowledgments. It is a pleasure to acknowledge the many insightful contributions of a friend and colleague, Stuart Rice, and to dedicate this article to him. This work is supported in part by the Caltech-JPL CRAY Supercomputing project. The calculations described here have been performed on the JPL-CRAY Y-MP2E/232. We thank Xueyu Song for useful discussions and are pleased to acknowledge the financial support of the National Science Foundation.

References and Notes

(1) Stuchebrukhov, A. A.; Marcus, R. A. *J. Chem. Phys.* **1993**, *98*, 6044.

(2) Stuchebrukhov, A. A.; Mehta A.; Marcus, R. A. *J. Phys. Chem.* **1993**, *97*, 12491.

(3) Kerstel, E. R. Th.; Lehmann, K. K.; Mentel, T. F.; Pate, B. H.; Scoles, G. *J. Phys. Chem.* **1991**, *95*, 8282. Gambogi, J. E.; L'Esperance,R. P.; Lehmann, K. K.; Pate, B. H.; Scoles, G. *J. Chem. Phys.* **1993**, *98*, 1116.

(4) Gambogi, J. E.; Kerstel, E. R. Th.; Lehmann, K. K.; Scoles, G. *J. Chem. Phys.* **1994**, *100*, 2612. Gambogi, J. E.; Lehmann, K. K.; Timmermans, J. H.; Scoles, G. *Abstracts of Papers*, American Chemical Society, **1994**, *207*, 115-PHYS. Gambogi, J. E.; Timmermans, J. H.; Lehmann, K. K.; Scoles, G. *J. Chem. Phys.* **1993**, *99*, 9314.

(5) Go, J. S.; Cronin, T. J.; Perry, D. S. *Chem. Phys.* **1993**, *175*, 127.

(6) Herzberg, G. *Infrared and Raman Spectra*; D. van Nostrand: New York, 1945.

(7) Hoy, A. R.; Mills, I. M.; Strey, G. *Mol. Phys.* **1972**, *24*, 1265.

(8) Gaw, J. F.; Willetts, A.; Green, W. H.; Handy, N. C. In *Advances in Molecular Vibrations and Collision Dynamics*, Bowman, J. M., Ed.; JAI Press: Greenwich, CT, 1990.

(9) Duncan, J. L.; McKean, D. C.; Nivellini, G. D. *J. Mol. Struct.* **1976**, *32*, 255.

(10) Allen, W. D.; Yamaguchi, Y.; Császár, A. G.; Clabo, D. A., Jr.; Remington, R. B.; Schaefer, H. F., III. *Chem. Phys.* **1990**, *145*, 427.

(11) Challacombe, M.; Cioslowski, J. *J. Chem. Phys.* **1991**, *95*, 1064.

(12) Kondo, S.; Koga, Y.; Nakanaga, T. *J. Chem. Phys.* **1984**, *81*, 1951.

(13) Frisch, M. J.; Trucks, G. W.; Head-Gordon, M.; Gill, P. M. W.; Wong, M. W.; Foresman, J. B.; Johnson, B. G.; Schlegel, H. B.; Robb, M. A.; Replogle, E. S.; Gomperts, R.; Andres, J. L.; Raghavachari, K.; Binkley, J. S.; Gonzalez, C.; Martin, R. L.; Fox, D. J.; Defrees, D. J.; Baker, J.; Stewart, J. J. P.; Pople, J. A. *Gaussian 92, Revision D.2*; Gaussian, Inc.: Pittsburgh, PA, 1992.

(14) Lawrance, W. D.; Knight, A. E. W. *J. Phys. Chem.* **1985**, *89*, 917.

(15) Zhang, Y.-F.; Marcus, R. A. *J. Chem. Phys.* **1992**, *97*, 5283.

(16) Gruebele, M. Private communication and preprint.

JP942667B

Chapter 5

A Periodic Boundary Conditions Formulation for Aqueous Solvent Dynamics

A Periodic Boundary Conditions implementation of Solvent Dynamics

Aseem Mehta

Arthur Amos Noyes Laboratory of Chemical Physics,
California Institute of Technology,
Pasadena, CA, 91125

Abstract

In this report a periodic boundary conditions (PBC) implementation of aqueous solvent dynamics is described. The dynamical behavior of TIP4P, rigid water molecules is obtained through the molecular dynamics (MD) calculation for 256 water molecules and a small "atomic" solute confined in a cubic box. The interaction potential consists of a Lennard-Jones part and an electrostatic part that is implemented using the Ewald sum technique. The results obtained compare favorably with previously reported simulations. The structural properties of the solvent are checked using the radial distribution functions and the solvation properties are obtained from the solute-solvent interaction energy from non-equilibrium and equilibrium simulations.

5.1 Introduction

Most chemical processes occur in the condensed phase. With the solvent being ubiquitous, it can and does play a major role in the rate of chemical processes. The nature of the solvent structure and its effect on and response to chemical change is a fundamental problem in chemical physics. The effect of solute-solvent interaction in reactions is made complicated because the reaction coordinate as well as its coupling to the solvent motion have to be well characterized. These complications make both the experimental and theoretical studies of processes in the condensed phase quite involved. From chemists' point of view, the solvent has sometimes been characterized by either its static dielectric constant or by parts of its dielectric response function $\epsilon(\omega)$. Such characterizations, naturally, consider the solvent as a dielectric and ignore its molecular nature. For fast chemical processes in solution the molecular nature of the solvent may be important at small distances from the solute.

The solvent dynamics around a solute may play an important role in the determination of reaction rates in the condensed phase. Recent experiments by Zewail and coworkers regarding the cis-trans isomerization in stilbene surrounded by a variable number of hexane molecules as the bath hint at interesting dynamical and kinetic phenomena[1]. This problem has been investigated via a modified Kramers' type of formulation to obtain reaction rates[2] when the motion along the reaction coordinate is being retarded by a frictional force. Electron transfer reactions in the condensed phase constitute another example where the nature of solvent dynamics is sometimes critical in determining the rate of the overall reaction[3, 4, 5]. In classical electron transfer theory, the expression for the outer-sphere reorganization energy takes the solvent as a dielectric continuum that is defined exclusively by its dielectric constants[6]. The accuracy of this assumption governs, to a large extent, the accuracy of the rate expression as a whole and, here, analysis of the solvent motion can be useful.

Molecular motion being very fast, only very recently have experimentalists been able to study the fast solvent response to a change in the solute's electrical proper-

ties with the availability of fast lasers. Such lasers have spurred the investigation of solvent-solute systems in gas phase (in the form of clusters in molecular beam machines) and in the condensed phase. These new techniques have uncovered the faster time-scale components in solvent dynamics that were previously hidden. Here we refer to the work of Zewail[1], Fleming[7], Yoshihara[8], Maroncelli[9] and Barbara[10].

These experimental advances have been simultaneous with new theoretical approaches to this problem. Analytically, Wolynes has introduced[11] the MSA (mean spherical approximation) and Bagchi and coworkers have used[12] the GLE (Generalized Langevin Equation) approach. Also, the availability of fast desktop workstations has led to good molecular dynamics (MD) calculations that have also shed light on the very short timescale dynamics that is primarily governed by the molecular nature of the solvent. Some recent computational contributions have been made by Warshel[13], Carter and Hynes[14], Maroncelli[15], Jorgensen[16], Rossky[17], Hidalgo[18] and Stratt[19]. These calculations have, generally, implemented molecular dynamics with periodic boundary conditions (PBC) and the Ewald sum[20] has been utilized to approximate the coulombic contribution out to infinity in the case of polar solvents.

Computationally, a handful of techniques have been used for simulating liquids. Some of the initial calculations used clusters of particles with two body Lennard-Jones type of interactions to characterize the solvent. This technique is useful for non-polar molecules such as noble-gas atoms[21]. For polar solvents a more involved formalism is required as the potential function that governs the interactions is long-ranged, decaying slower that r^{-3}. Typically, studies have utilized the Ewald sum to account for the long-range forces by doing the calculation in Fourier or reciprocal space within the PBC formalism[15]. Furthermore, some investigators have modeled the liquid as a large cluster[22, 23]. It is also possible to utilize the reaction field method to account for the long range forces[24, 25]. However, to date this has not been the method of choice.

In the PBC formalism the molecules representing the solute and the solvent are usually confined to a cubic cell and periodic boundary conditions are enforced. For solvent dynamics calculations, we are usually interested in a solute surrounded by

a large number of solvent molecules. Realistically, as the solute imposes its own field on the solvent, the system as a whole is not isotropic. This anisotropy may be particularly important for a charged solute with a polar solvent. However, with periodic boundary conditions a quasi isotropy is artificially enforced. This isotropy occurs because the unit cell is infinitely replicated, causing an unphysical change of sign in the solvent's polarization at the cell edge. Although this isotropy may be correct for simulations of a bulk liquid, where there is no solute to impose its field and so the solvent is not polarized, it could introduce significant error when solutes with specific charge distributions and their interactions with polar solvents are being studied, unless the cell size is sufficiently large.

We have recently implemented a method for solvent dynamics calculations that utilizes a reaction-field (RF) formalism, where a cavity containing the solute and some solvent molecules is surrounded by a dielectric continuum[26]. This method, by definition, does not enforce a quasi-isotropy and utilizes the fact that after some critical distance the solvent's molecular nature may be replaced by a dielectric continuum. Some of the issues that we wish to address are : 1) the range to which the molecular nature of the solvent is important, 2) whether using a non-periodic formalism such as a cavity in a continuum is feasible, and 3) how the calculations using the reaction-field formalism compare with the results from the PBC calculations. To address these questions, we have made molecular dynamics calculations with the PBC system and have developed a formalism for analogous calculations in a reaction field system, where a cavity containing molecular solute and solvent particles is surrounded by a dielectric continuum. Substantial efforts have been required for obtaining a well characterized cavity-continuum interaction, particularly at the surface of interaction.

In this chapter, the PBC calculations on water with an "atomic" solute are described. In the following sections the potential function used, the propagator used for integration of the equations of motion, the structural and dynamical properties obtained from the calculations and the data analysis and results are presented. The results from the reaction field simulations are presented in the next chapter.

5.2 Equations of Motion

The dynamical behavior of any particle in a system with specified initial conditions can be written as

$$x(t+\Delta t) = x(t) + \dot{x}(t)\Delta t + \frac{1}{2}\ddot{x}(t)(\Delta t)^2 + \cdots, \tag{5.1}$$

where, $\dot{x}(t)$ is the time time derivative of the variable x. For a classical system, the second time derivative of the spatial variable or the acceleration can be written in terms of the force experienced by the given coordinate which, in turn can be written in terms of the potential

$$\ddot{x}(t) = \frac{f_x}{m} = -\frac{1}{m}\frac{\partial V}{\partial x}. \tag{5.2}$$

A three-dimensional body, such as a rigid molecule, has orientational degrees of freedom along with the translational degrees of freedom. The translational motion of the center of mass of a rigid body is governed by equation 5.1, where x is one of the translational coordinates and $\ddot{x}(t)$ is obtained from equation 5.2. The rotational motion of a rigid body with inertia tensor I and angular velocity ω is governed by an equation similar to 5.1. The orientational coordinates used are *quaternions*[27] that are functions of the more well known Euler angles. The governing equation for the orientational coordinates is[28]

$$I \cdot \dot{\omega} - \omega \times I \cdot \omega = N, \tag{5.3}$$

where, N is the torque (moment of force) defined (for atom coordinates r_i, center of mass coordinate R and force f_i at atom i) by

$$N = \sum_i (r_i - R) \times f_i. \tag{5.4}$$

Given the force f and the torque (moment of force) N that act upon a body, the position and orientation of the body may be accurately determined for any time by integrating the equations of motion such as equation 5.1 with an appropriate choice for

Δt. For a rigid molecule with n atoms treated as mass points, the forces and torques can be determined from the forces experienced by each atom at every time step. The main technical question that remains is the selection of a physically accurate potential for the interaction between particles and an integrator to propagate the above mentioned equations of motion. Although equation 5.1 is formally correct for use as the propagating equation, other algorithms give more accurate results since appropriate linear combinations of similar equations for $x(t-\Delta t), x(t-2\Delta t), \ldots$ are accurate to a higher order in Δt. This fact is important as it allows for larger values of Δt to be used for the actual calculations.

The public-domain molecular dynamics package MolDy was used for the PBC calculations. For the reaction field calculations, the MolDy package was substantially modified for solving the equations of motion for molecules restricted to a spherical cavity surrounded by a dielectric continuum. The propagating equations used for both type of calculations are a variant of the well known Verlet algorithm[20].

5.3 Experimental Background

Experimentally, solvent dynamics is usually studied through pump-probe spectroscopic experiments on solute-solvent systems in the condensed phase. Solute molecules are placed in an electronically excited state by the pump pulse. The probe pulse is used to study the fluorescence of the excited state to the ground state as a function of a known delay between the pump and the probe pulses. The delay allows the solvent molecules to reorient and become partially equilibrated with the excited state. Experimentally, the solute is usually chosen to be a large organic dye molecule. The physics of this process is schematically shown in Figure 5.1

The normalized quantity usually used to describe the the solvent response is a response function,

$$S(t) = \frac{\nu(t) - \nu(\infty)}{\nu(0) - \nu(\infty)}. \tag{5.5}$$

$\nu(t)$ typically refers to the peak of the fluorescence spectrum obtained after a time-

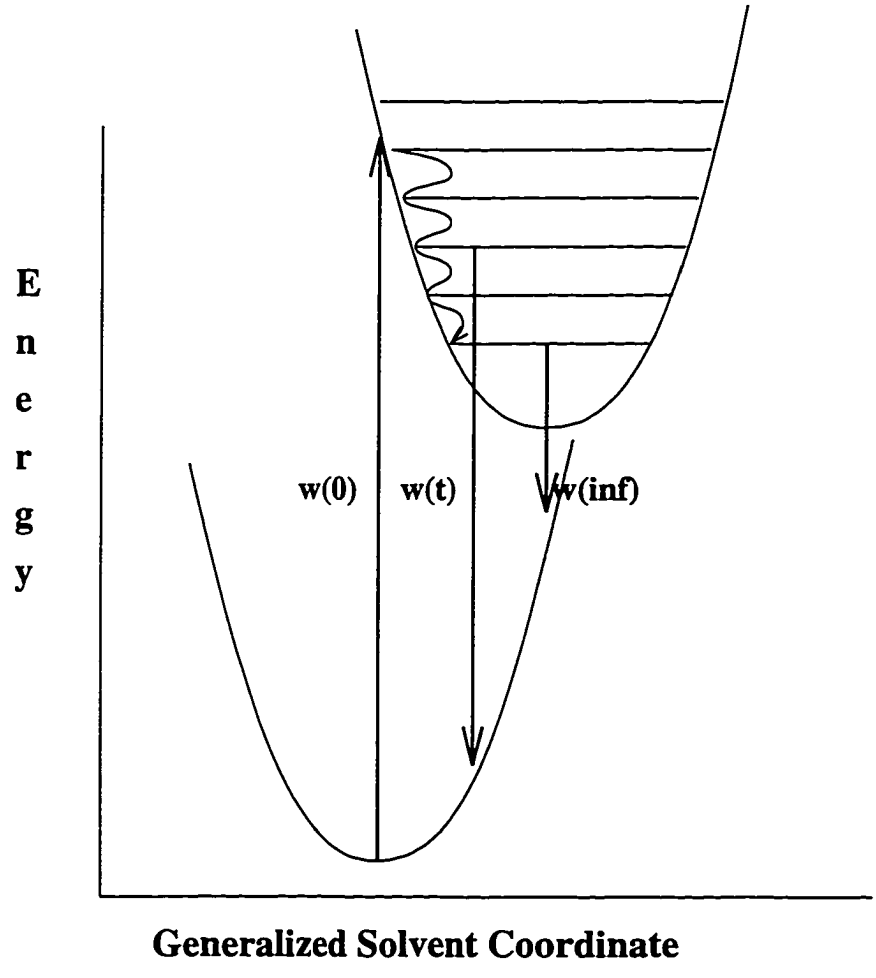

Figure 5.1: Schematic representation of Solvent Dynamics upon electronic excitation of the solute

delay of t following the electronic excitation. The width of the emission at time t may also provide useful information, but has rarely been used in the analysis. (The width usually changes only a little with time.)

The shape of the response function, $S(t)$, has been fairly well characterized. For small "atomic" type solutes with polar solvents, the initial innermost solvation shells are well defined and any instantaneous delta function change in an electrical property of the solute results in a significant impulsive force acting on the solvent molecules of the nearby solvation shells. This impulsive force leads mainly to sharp changes of the orientations of the solvent molecules. Such fast, initial motion preserves the solvent shell structure during a sub 50fs time scale. This type of sharp, jerky motion of the solvent molecules near the solute has been termed the "inertial" response of the solvent. This motion causes a sharp fall from unity of the solvent response function over a 0 to 0.2ps timescale. This sharp decay is sometimes also accompanied by oscillations that may be due to the symmetrical stretching or a symmetrical rotational type of motion of the initial solvation shell. This initial decay in the response function is usually followed by a slower exponential type decay. This slow decay is usually attributed to "polarization diffusion," where the solvent shells rupture and reform, and the solvent generalized coordinate approaches a new equilibrium value around the solute. It should be mentioned that most of the data for the solvent response for "small solutes" comes from computational simulations, most experiments typically using large dye molecules as solutes.

For larger solutes, the solvent response can usually be fit fairly well by a biexponential decay curve with some superimposed peaks. The solvent structure around the larger solute is more diffuse and so the initial decay of the solvation response curve, although still prominent, is smaller. The work of Fleming and coworkers[7] provides an instructive example of this difference of the response for small and large solutes.

5.4 Computational Strategies

5.4.1 Equilibration from Initial Configuration

Before going into the details of how such experiments can be simulated through MD calculations to obtain computationally the solvent response function, a few important technical details are described. Before an attempt may be made to obtain any physical data from an MD trajectory, the system has to be in its equilibrium configuration. The first part of any MD calculation, then, is its equilibration to the minimum free energy state since any arbitrarily chosen initial configuration is not necessarily a probable member of the equilibrium set of configurations. The choice of the initial starting configuration is an important technical point and the initial configuration should be such that non-physical, large and impulsive forces are avoided since the solutions of the MD equations are liable to diverge when the forces are abnormally large.

One technique is to use a crystalline starting configuration. Since such a configuration may be too ordered for liquid phase simulation, in the reported calculations the initial configuration is obtained using a "skew start" method[28] that ensures that there is at least a minimum separation between the molecular centers of mass without placing them at the vertices of a crystalline structure. The initial orientations of the individual molecules are typically chosen to be random and the initial velocities are obtained from a Maxwell-Boltzmann distribution.

Since the initial configuration is unlikely to belong to the set of minimum free energy configurations, propagation of the MD equations in an ensemble at a given N (number of particles), V (volume) and E (energy) (NVE) is going to take the system to, on the average, lower potential energy configurations and thereby increasing its kinetic energy. To maintain a generally constant temperature during the actual simulation, the approach to equilibrium is accompanied by periodic scaling of the translational and rotational velocities[20, p. 171]. The starting configuration is propagated forward in time with the MD equations and every few time-steps the translational and rotational velocities of the molecules are scaled to the predetermined applied

temperature, at which the simulation is desired to occur, using

$$\frac{3}{2}Nk_bT = \frac{1}{2}m\langle v^2\rangle = \frac{1}{2}I\langle\omega^2\rangle. \tag{5.6}$$

This scheme allows for the dissipation of the excess kinetic energy that would build up when the starting configuration does not belong to the set of the minimum energy states. This procedure, when continued for a few thousand time-steps, allows the system to reach thermal equilibrium. This approach has proved successful in practice. One simple measure of the system's being in equilibrium is obtained from monitoring the total potential and kinetic energy of the system after scaling has been stopped. If the potential and kinetic energies remain constant, within some fluctuations, without any systematic deviation, the system may be considered to be at equilibrium.

Once the system has reached equilibrium, the scaling is stopped and the system is then allowed to exclusively follow Newtonian dynamics ($\ddot{x}(t) = -\frac{1}{m}\frac{\partial V}{\partial x}$) within the predetermined ensemble (here, NVE). Since the positions, velocities and orientations are available for all the molecules during the whole trajectory, any physical property of interest may then be calculated.

5.4.2 Solvent Structure

Before any quantities particular to solvent dynamics are calculated, it must be ensured that the potential used and the calculational strategy employed (such as PBC or reaction field methods) result in a good description of the solvent. By a good description it is meant that the MD trajectories yield accurate structural and dynamical information for the solvent. To this end, solvent radial distribution functions (RDFs) are usually calculated and compared to previously known computational or experimental data. The RDF is defined as

$$g_{\alpha\beta}(r) = V\left\langle \delta\left(|\mathbf{r} + \mathbf{r}_{1\alpha} - \mathbf{r}_{2\beta}|\right)\right\rangle, \tag{5.7}$$

where, α and β represent the types of atoms and $\mathbf{r}_{1\alpha}$ and $\mathbf{r}_{2\beta}$ refer to the position of the particle α or β on molecule 1 or 2. The average is taken over all the molecules in the system. The RDF is calculated from the pair distances between atoms for a select number of configurations obtained from the MD trajectory. The radial distribution function is a quantity of central importance in liquids because they provide information about the local short-range order around a central molecule[29]. The histogram of pair distances is normalized to obtain the RDFs. The normalization is such that, for a single component system, if ρ = number density, then

$$4\pi \int_0^{R_c} \rho g(r) r^2 dr = N, \tag{5.8}$$

where, N is the number of particles in a sphere of radius R_c. For water, RDFs of particular interest are those for O-O, O-H and H-H ones. These quantities are compared with the experimental quantities to determine the extent to which the potential energy function and the calculational scheme yield a correct description of the solvent. Other quantities usually calculated are the velocity correlation function, density profiles at various places within the simulation volume, and the orientational distribution functions. In some studies it has also been attempted to obtain the dipole correlation function $\langle M(0)M(t)\rangle$ and the dielectric dispersion curve from such calculations[13, 15]. The dipole correlation function is usually the most difficult quantity to obtain accurately through simulations.

5.4.3 Solvent Dynamics from MD trajectories

Once the system of solute and solvent molecules has been equilibrated and once the structural and dynamical quantities have been calculated to show that the system is a good approximation to that being simulated, the solvent dynamics quantities can be calculated with more confidence. Starting from the calculation for an equilibrated system, two methods may be used to obtain the computational approximation to the solvent response function $S(t)$ described in equation 5.5. Using the fluctuation-dissipation theorem, it can be shown[15, 30] that, in the linear response regime, the

correlation of the fluctuations in the electrostatic potential $V(t)$ created by the solvent at the solute,

$$C(t) = \frac{\langle \delta V(0) \delta V(t) \rangle}{\langle \delta V(0) \delta V(0) \rangle}, \tag{5.9}$$

is equal to the solvent response function $S(t)$ that would be obtained from the result of a sudden change in the charge of the solute. It is assumed here that the non-polar interaction between the solute and the solvent is the same regardless of the solute's net charge. Similar relationships exist between other equilibrium correlation functions and solvent response functions obtained from other step function changes of the electrical properties of the solute. $V(t)$ is simply the electrostatic potential created by the solvent at the solute that can be calculated at every time-step in the trajectory and

$$\delta V(t) = \langle V(t) \rangle - V(t). \tag{5.10}$$

It is also possible to directly obtain $S(t)$ from MD calculations by simulating the step function change in the electronic property of the solute that is analogous to the experimental change in the solute that would be caused by the interaction of the laser with the solute. This step function change can be simulated by suddenly changing, in an equilibrated system, the electrical property whose effect is being probed. Some of the changes usually probed include the change in the charge distribution (e. g., dipole) in the solute that occurs when the solute is electronically excited or a change in the total charge of the solute that would occur upon photo-ionization. Upon this change, the solvent molecules are no longer in equilibrium with the new electrostatic state of the solute since they were in equilibrium with the ground (or other initial) state of the solute. The solvent molecules change their orientational and translational positions to return to thermal equilibrium with the solute. It is this change that is monitored and analyzed via equation 5.5 to obtain the response function. Computationally, after changing the electrical property in question the MD calculation is continued to obtain the time-dependent solute-solvent interaction energy. The solvent response function

is calculated analogously to experiment,

$$S(t) = \frac{E_{int}(t) - E_{int}(\infty)}{E_{int}(0) - E_{int}(\infty)}. \tag{5.11}$$

$E_{int}(t)$ includes the above defined $V(t)$ along with $E_{LJ}(t)$, the Lennard-Jones (or van der Waals) contribution to the solute-solvent interaction energy. Rigorously, the equality between $C(t)$ and $S(t)$ is correct only when $V(t)$ is used in equation 5.11 instead of $E_{int}(t)$. As a practical matter, for the solute used, $E_{LJ}(t)$ is less than 5% of the total solute-solvent interaction energy and its inclusion in the above equation does not change the resulting solvent response function. This calculation is performed for several different initial configurations of the equilibrated ground state to obtain a representative collection of initial configurations and to compare with $C(t)$ that is, by definition, a configurational average. Comparison of $C(t)$ with $\langle S(t) \rangle$ also provides a test of the linear response approximation. It is important to note that as the perturbed system returns to thermal equilibrium, there is some increase of kinetic energy and in the temperature of the system (this phenomenon has been referred to as "local heating.") The system should be large enough to absorb this increase without any change in the observables or the lifetime of the observables should be short enough such that the "local heating" has no effect on it.

Having obtained all the analytical machinery for the propagation of the dynamical equations and for data analysis, we now define the potential function we use to govern the dynamics. A good potential is, of course, essential to obtain good dynamical information from the MD trajectories.

5.5 Intermolecular Potential

The intermolecular potential may be written, schematically, as

$$V = V_{LJ} + V_e, \tag{5.12}$$

where, V_{LJ} is the Lennard-Jones potential between oxygen atoms,

$$V_{LJ} = \epsilon \left[\left(\frac{\sigma}{r}\right)^{12} - \left(\frac{\sigma}{r}\right)^{6} \right] \tag{5.13}$$

and V_e is the electrostatic potential which, for PBC, is written as an Ewald sum,

$$\begin{aligned} V_e \;=\; & \frac{1}{4\pi\epsilon_0} \sum_{\boldsymbol{n}} \sum_{i=1}^{N} \sum_{j=i+1}^{N} q_i q_j \frac{\operatorname{erfc}(\alpha|\boldsymbol{r}_{ij}+\boldsymbol{n}|)}{|\boldsymbol{r}_{ij}+\boldsymbol{n}|} + \\ & \frac{1}{2\epsilon_0 V} \sum_{\boldsymbol{k}\neq 0} \frac{1}{k^2} e^{-\frac{k^2}{4\alpha^2}} \left\{ \left| \sum_{i=1}^{N} q_i \cos(\boldsymbol{k}.\boldsymbol{r}_i) \right|^2 + \left| \sum_{i=1}^{N} q_i \sin(\boldsymbol{k}.\boldsymbol{r}_i) \right|^2 \right\}. \end{aligned} \tag{5.14}$$

The Lennard-Jones potential, being short-ranged, is simple to calculate. In the PBC formulation, the L-J term is calculated up-to some critical distance r_c. For a system of charges, the electrostatic potential is written as a sum of short-range and long-range contributions, as in equation 13, where the former are written in real space and the latter in reciprocal space, where the periodicity of the MD cell is used.

The rigid four-center, TIP4P water model[31] was used for the calculations. This model has been used for a variety of simulations of liquid water and has been well tested[32, 33]. The parameters that define this potential are specified in Table 1. Since this model is rigid, the vibrational motion of the water molecules is ignored.

Table 5.1: Parameters defining the TIP4P potential

r(OH) (Å)	∠HOH (deg)	ϵ_{OO} (kcal/mol)	σ_{OO} (Å)
0.9572	104.52	0.6201667	3.1536
q_O	q_H	q_M	r(OM) (Å)
0.0	0.52e	-1.04e	0.15

So, for a particle in a MD cell, part of its electrostatic potential is calculated directly as interactions with other charged particles upto some r_c and the long-range part is calculated from $r = r_c$ to ∞ but in the reciprocal space. The Ewald sum has been extensively used for simulations of polar liquids. Here, only a brief description of the potential has been provided. Allen and Tildesley[20] and Refson[28] give a detailed

explanation of the Ewald sum and its use in MD simulations. The periodic boundary conditions are imposed in the program MolDy through the link cell method[28].

For the PBC calculations reported in this chapter, the parameters used to define the LJ interaction between the solute (X) and the solvent molecules were $\epsilon_{OX} = 0.1$ (kcal/mol), $\sigma_{OX} = 3.0$ Å, $\epsilon_{HX} = 0.1$ (kcal/mol) and $\sigma_{HX} = 3.0$ Å.

This set of interactions between the "atomic" solute and the solvent molecules is similar to the small solute designated "S0" by Maroncelli and Fleming[15]. This choice of the solute-solvent interaction allows for a comparison between the present results and the ones obtained earlier by them. However, it should be stressed that there are significant differences in the two approaches to solvent dynamics. In the earlier calculations a large spherical cluster of water molecules was used with a solute constrained to be at the center of the cluster to model the solute-solvent system. In the calculations described here periodic boundary conditions are used without any constraint on the position of the solute. Here, the potential energy function governing the dynamics is the Lennard-Jones potential and the Ewald sum for the long ranged polar terms. In the earlier study the Lennard-Jones potential and only $V_e = \sum q_i q_j / r_{ij}$ term for the electrostatic part were used. Also, whereas, here, we use the TIP4P potential to model the individual water molecules, in the earlier work the ST2 model was used. However, despite these differences, the two simulation, without being identical, should provide similar results and trends for the dynamical simulations.

5.6 Results and Discussion

In this section results from MD simulations of pure solvent and solute-solvent systems are described. In both cases 256 TIP4P water molecules were confined to a cubic box of side $\approx$ 20 Å. A single "atomic" solute, with the LJ parameters given in section 5.5 was used in the solute-solvent system. For each simulation, the initial configuration was brought to equilibrium using periodic kinetic energy rescaling for $10 - 30ps$ and then trajectories were followed for $50 - 100ps$ for data collection.

Kinetic and potential energies were monitored during the data collection period to ensure that such energies were well conserved. Radial distribution functions were calculated from the instantaneous configurations of the molecules at different times during each trajectory.

5.6.1 Energy Conservation

Since we are attempting to follow an MD simulation within the NVE ensemble, it is important to confirm that the kinetic and potential energy are conserved during the simulation. In some earlier attempts at simulations periodic rescaling of the kinetic energy has been used even after equilibrium had been reached[15]. We avoid rescaling the energies after equilibrium is reached to ensure that the ensemble being used is always microcanonical. The temperature of the system was set at $300K$ during the equilibration period. In Figure 5.2 the temperature of the system monitored during a 50 *ps* simulation with 256 solvent molecules and one solute is shown.

We find that there is a slight upward increase in the total kinetic energy (or temperature) as a function of time but even with a $50ps$ trajectory, the kinetic energy is conserved to within 5% of the total.

The conservation of the total potential energy is even better than that for the kinetic energy. In Figure 5.3 the total potential energy of the system, monitored during the $50ps$ simulation is shown.

Since the number of water molecules in this simulation is 256, it can be calculated from Figure 5.3 that the potential energy per molecule (V/N, the total solvational energy per molecule) is $\approx$ -41 kJ/mol $\approx$ -10 kcal/mol, which compares very well with previously determined values of -9.9 kcal/mol to -10.4 kcal/mol, as calculated by Maroncelli and Fleming[15]. The total energy is conserved to better that 1% of the total.

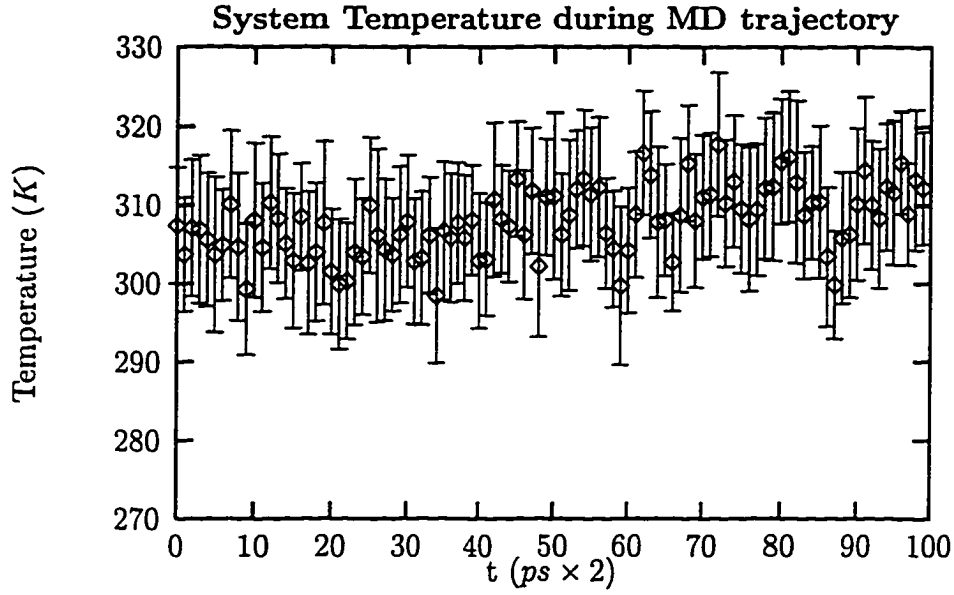

Figure 5.2: Conservation of Kinetic Energy during an Equilibrated Simulation

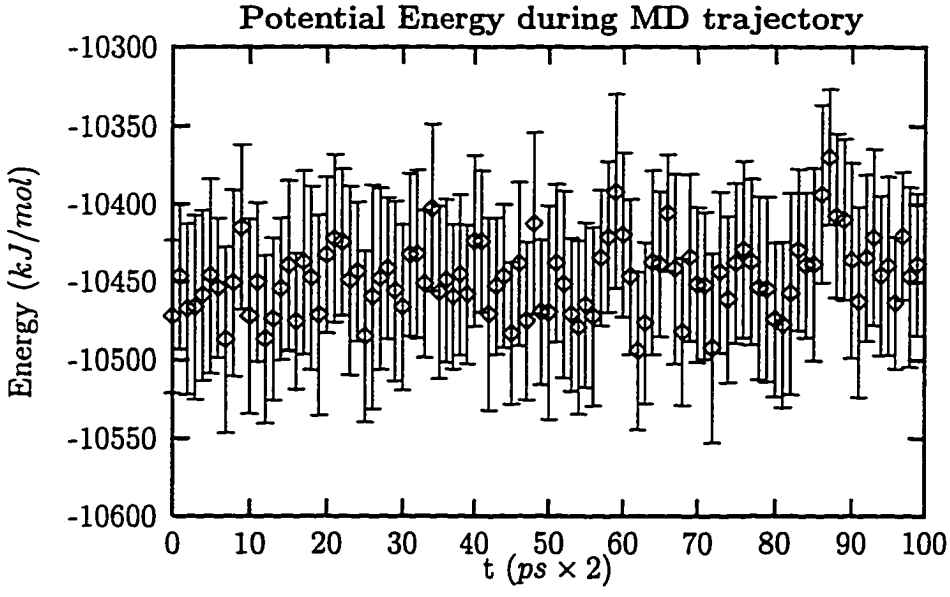

Figure 5.3: Conservation of Potential Energy during an Equilibrated Simulation

5.6.2 Radial Distribution functions

Since a major goal for the present study is to obtain a new and useful method of MD calculations, one that is particularly relevant to solvent dynamics calculations, it is imperative to see if the model gives a good description of the solvent. One well recognized prerequisite for ensuring that a liquid is well described by the simulation is to obtain the radial distribution function from a list of pair-distances. Normalization of a histogram of these pair distances yields the RDF. Since the TIP4P potential has been extensively used and tested, RDFs from MD and Monte Carlo simulations of liquid water are available in the literature[31, 34].

In Figure 5.4, the O-O RDF is shown. This figure compares very favorably with the oxygen-oxygen radial distribution function given by Jorgensen and coworkers[31], where they used Monte Carlo simulations, as well as the one given by Klein and Watanabe[34] where MD simulations were utilized. The RDFs obtained by Jorgensen and coworkers are shown in Figures 5.5 and 5.7. In these two references it is also shown that the RDFs from the TIP4P potential are close to the experimental data obtained from x-ray techniques[35]. The O-H and the H-H distribution functions calculated from the simulations, shown in Figure 5.6 also compare well with same previously published results.

5.6.3 Solvent Dynamics

As described earlier, the main quantity of interest for solvent dynamics is the solvent response function $S(t)$ that may be obtained from MD trajectories in two ways. From the equilibrium MD trajectories, the electrostatic potential at the solute may be calculated at each time step to obtain $C(t)$ as defined earlier, which, under linear response, is the same as the solvent response function, $S(t)$. It is also possible to obtain the $S(t)$ directly from the non-equilibrium MD trajectories by calculating the solute-solvent interaction energy at every time step.

Both sets of calculations were performed for a solute-solvent system with one "atomic" solute and 256 TIP4P water molecules in a cubic cell, $\approx$ 20 Å on a side,

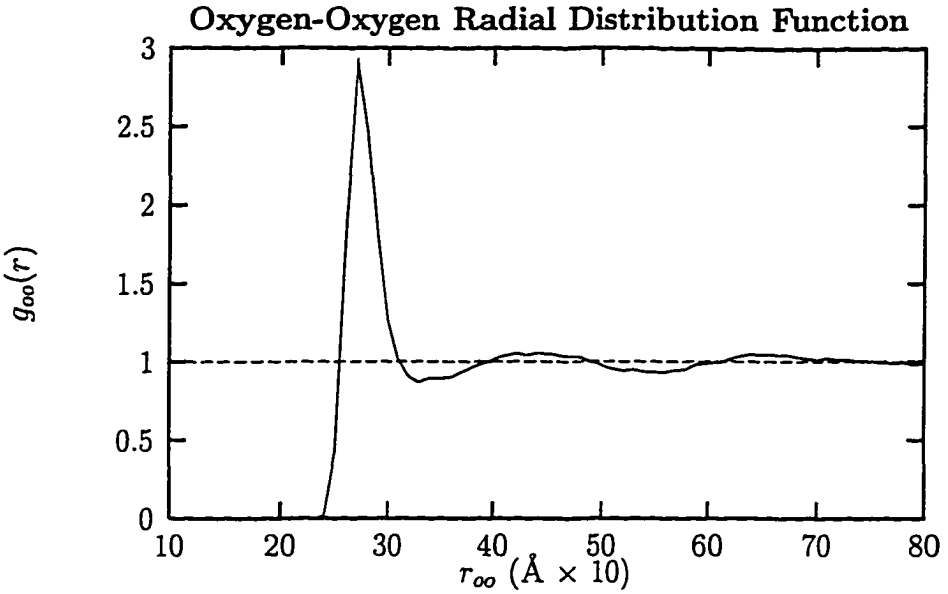

Figure 5.4: The O-O Radial Distribution Function

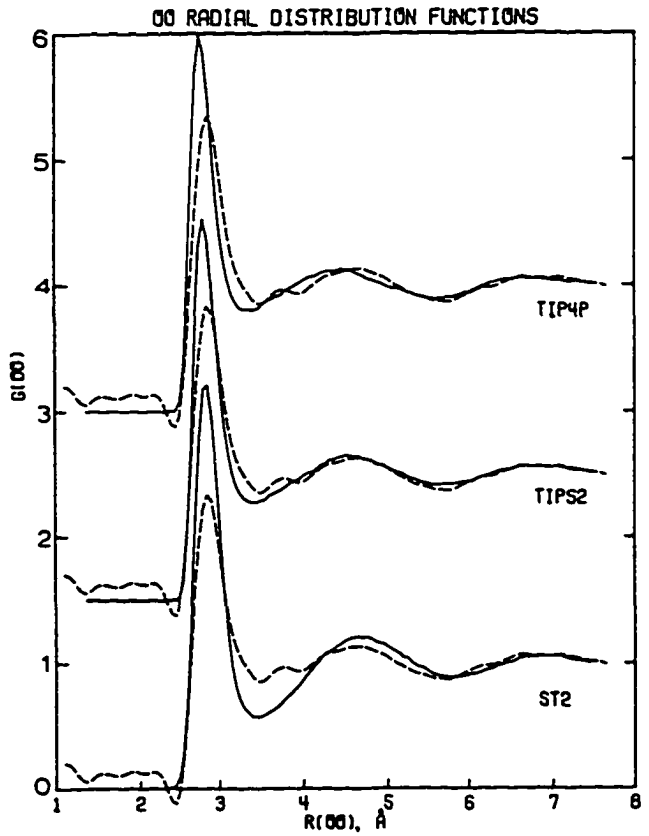

Figure 5.5:
The O-O Radial Distribution Function from Reference [31]

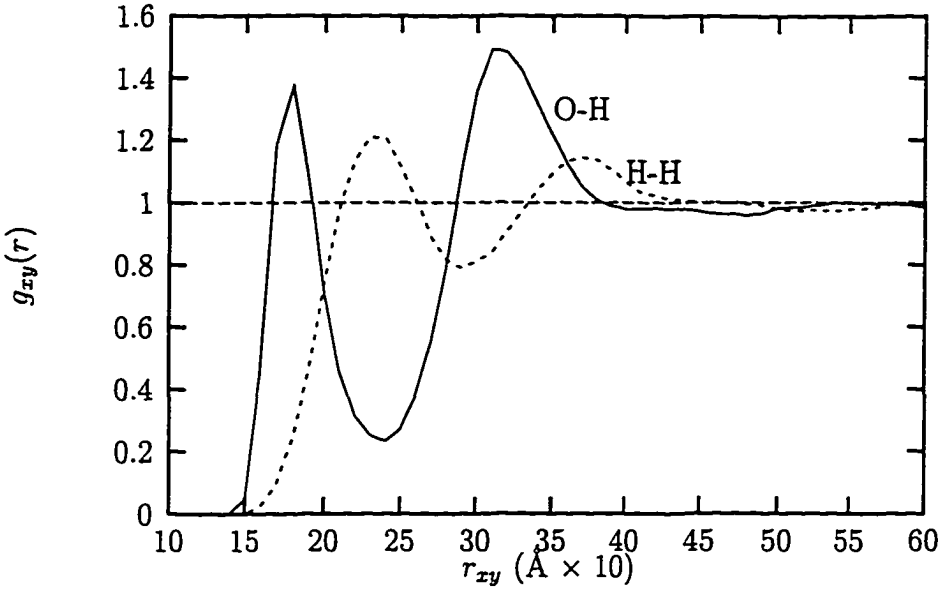

Figure 5.6: The O-H and H-H Radial Distribution Functions. $r_{xy} = r_{OH}$ or r_{HH}

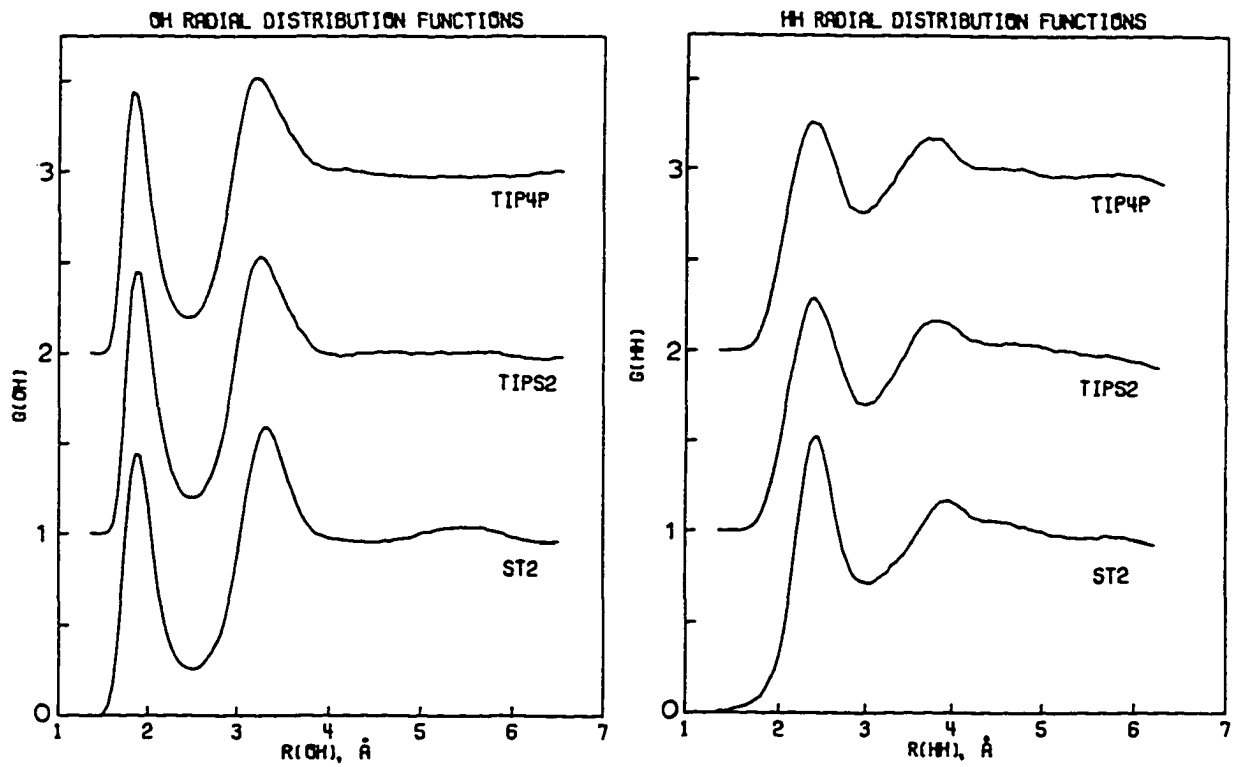

Figure 5.7:
The O-H and H-H Radial Distribution Functions from Reference [31]

with periodic boundary conditions and the potential at the solute was calculated at each time-step. The potential correlation function, $C(t)$ was obtained from this calculated potential. In Figure 5.8 the $C(t)$ is shown for an uncharged solute.

In this figure some of the defining characteristics of the solvent dynamics around a small, uncharged solute are clearly seen. The sharp initial decay followed by a slower and oscillatory decay has been a hallmark of such solutes [7, 15]. The initial part of decay represents the "inertial" or rotational ("librational") motion of the solvent molecules around the solute and the latter part represents the diffusive motion. For small uncharged solutes, the fast initial decay is a dominant component of the total decay. Comparing Figures 5.8 and 5.9, it is clear that the $C(t)$ correlation function for an uncharged solute differs appreciably from the charged solute.

In Figure 5.9 the correlation function for a small solute with a unit positive charge is shown. When compared with the correlation function for the neutral solute, shown in Figure 5.8, we find that this $C(t)$ is much less oscillatory and slower. Once again we find that this results is similar to the ones obtained earlier[15]. The less sharp initial decay and the recurrence at $\sim 150fs$ are well recognized characteristics of the solvent dynamics of water for small charged solutes.

It was argued earlier that the initial decay of $C(t)$ is caused by the rapid "inertial" or orientational motion of the solvent molecules, and the slower long time decay is due to the translational motion of the solvent molecules. The charged solute is quite effective in ordering the polar water molecules around itself. This causes the rotational motion of the such solvent molecules to be hindered, since the polar solvent molecules surrounding a charge have a preferred direction, unlike the case for uncharged solute. As the rotational freedom of the initial solvational shells is curtailed, it is the slower translational motion of the solvent molecules that plays the more important part in the solvent relaxation. The induced polarization curtailing of the rotational motion causes the response function to decay at a slower rate. The recurrence seen at $\sim 150fs$ in Figure 5.9 is postulated as being caused by the coherent "breathing" mode of the initial solvation shell.

Compared to previous work[15], it is found that these characteristics of the time-

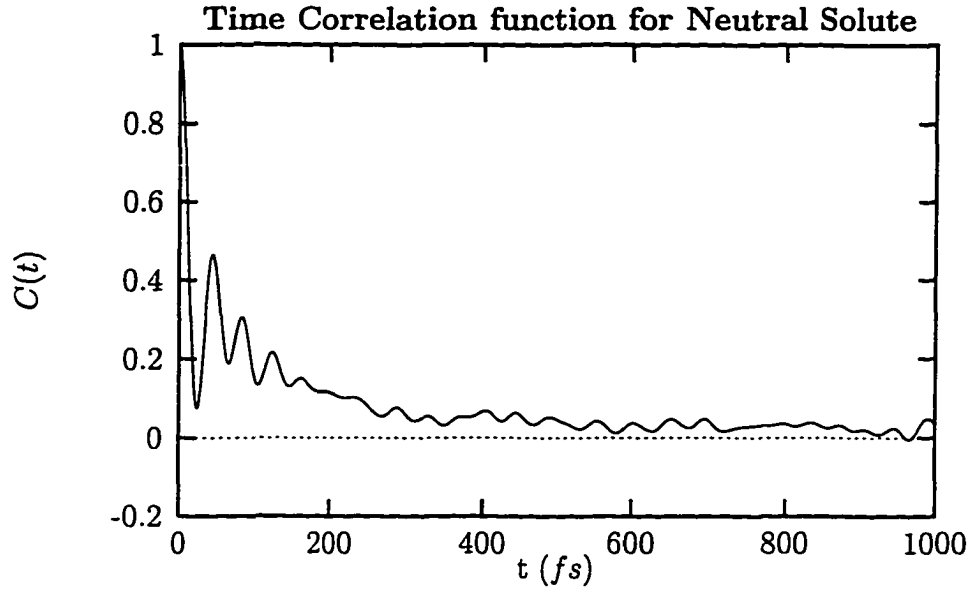

Figure 5.8: tcf $C(t)$ for a "small" Neutral Solute

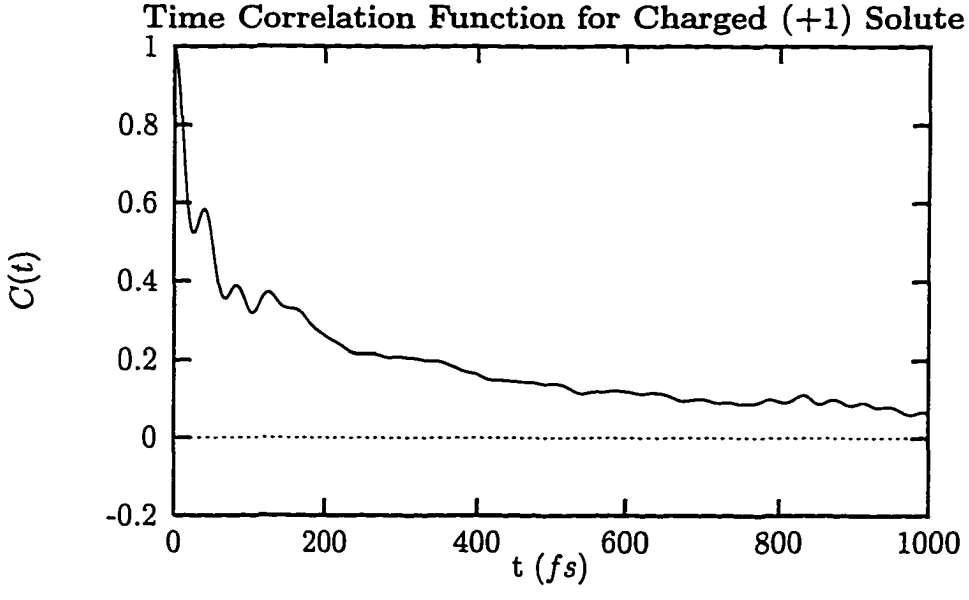

Figure 5.9: tcf $C(t)$ for a "small" Charged (+1) Solute

correlation function $C(t)$ in Figure 5.8 are representative of the small ("S0") charged solute. The adjective "small" depends upon the magnitude of the LJ parameters σ and ϵ. Values close to the ones for the oxygen atom merit such an adjective. Comparing the $tcfs$ for charged solutes, it is observed that the $tcfs$ of the two works are similar. It is also observed that the time-correlation functions for charged solutes are not very sensitive to the size of the solute[15].

Hsu *et al.*[36] have recently obtained the solvent response function through an analytical, reaction field, "cavity in continuum" model of the solute-solvent system. The positively charged sherical solute is embedded in a solvent described exclusively by its dielectric dispersion curve $\epsilon(\omega)$. In Figure 5.10 the results of Hsu and the experimental results of Fleming[7] are shown together with the present results for comparison. Since the actual experimental $\epsilon(\omega)$ is used, Hsu *et al.* can associate charateristics of the tcf with individual $\epsilon(\omega)$ peaks. They share our belief that the recurrence at 150-200fs is caused by the intermolecular "breathing" type of motion of the solvent molecules and that the initial sharp decay is mainly due to the high-frequency "librational" motion of the solvent. The Debye part of the $\epsilon(\omega)$ contributes, although not exclusively, to the long time decay of the tcf. In brief, it is determined that the short time behavior of the solvent response function is dominated by the "librational" motion of the solvent, the slower components arise due to the "diffusive" motion of the solvent caused mainly by the translational (with contribution from rotational) movement of solvent molecules.

In Figure 5.11 the $S(t)$, obtained from non-equilibrium simulations, is shown. As described earlier, this function is obtained by suddenly changing the charge (from neutral to $+1e$) of the solute in an equilibrated system. Then the solute-solvent interaction energy is calculated as the system returns to a new equilibrium. The solute-solvent interaction energy, here, provides the solvent-response function directly. To simulate the fact that in the experiment there is an ensemble of initial configurations (all consisting of the solute ground state being in equilibrium with the solvent) that is averaged over in a pump-probe experiment, a number of different initial equilibrium configurations with neutral solute are used. In Figure 5.11, five such ground state

equilibrium configurations were used and individual $S(t)$ curves were then averaged.

Five simulations provide a rough idea of the $S(t)$ and a larger number of such simulations should be used for a more refined result. In particular, the oscillations seen in Figure 5.11 after $\sim 400fs$ are an artifact of the small number of individual non-equilibrium simulations. With more simulations added to the average, the late oscillations should be averaged out. Maroncelli and coworkers, in their aqueous solvation dynamics study[15], used forty simulations to obtain the $S(t)$ from non-equilibrium simulations. The main characteristics of this curve are its initial resemblence to the neutral solute tcf followed by its resemblence to the charged solute tcf for $t > 200fs$.

In general, we find that we are able to reproduce the previously obtained major results[15] of aqueous solvation dynamics with a PBC simulation of ~ 250 solute and solvent molecules. These results are a stepping stone to our major goal of replacing the PBC method with a reaction field method that is non-periodic.

5.7 Conclusion

In this chapter, a periodic boundary conditions implementations of solvent dynamics is described. This research was implemented as a first step towards obtaining an understanding of solvent dynamics by developing a non-periodic reaction field method. Results obtained using this PBC scheme within a ≈ 20Å sided cubic cell are consistent with previous simulations. These results are useful as a benchmark with which future calculations can be compared. Also, a successful conclusion of such calculations provide confidence in tackling the next part of this project, which is to do MD calculations for solvent-solute systems in a spherical cavity surrounded by a dielectric continuum without the use of periodic boundary conditions.

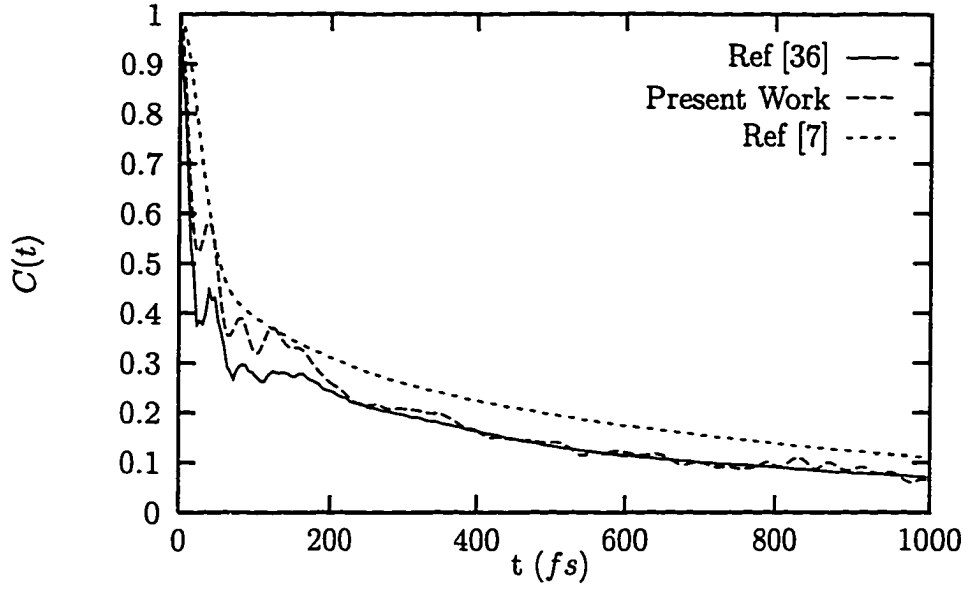

Figure 5.10: Comparison of Charged Solute tcfs obtained from simulation (Present Work), analytical model and experiment.

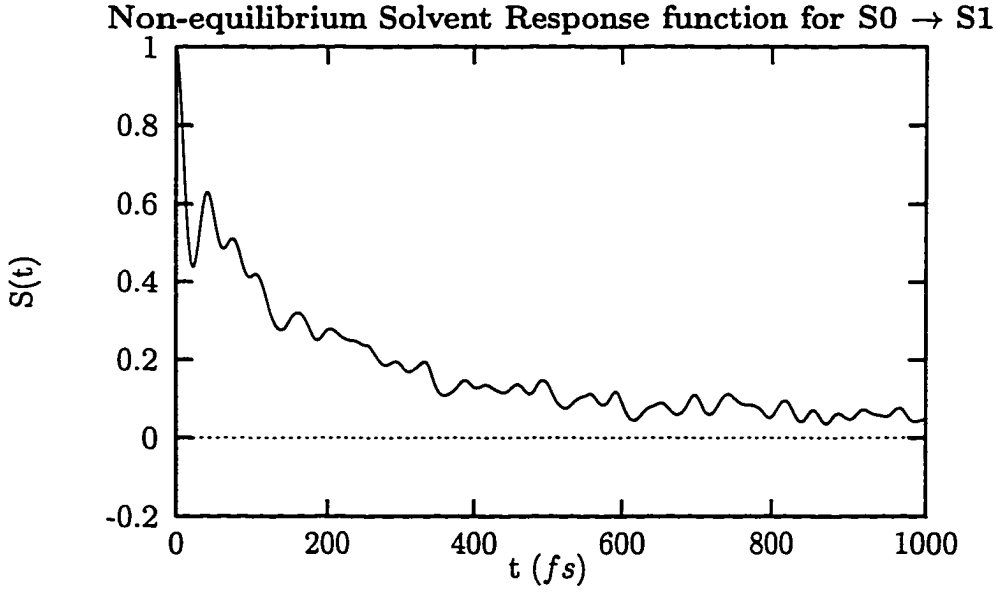

Figure 5.11: Directly Simulated Solvent Response Function

Bibliography

[1] Heikal, A. A.; Chong, S. H.; Baskin, J. S.; Zewail, A. H. *Chem. Phys. Lett.* **1995**, *242*, 380.

[2] Marcus, R. A. *Chem. Phys. Lett.* **1995**, *244*, 10.

[3] Leite, V. B. P.; Onuchic, J. N. *J. Phys. Chem.* **1996**, *100*, 7680.

[4] Gayathri, N.; Bagchi, B. *J. Phys. Chem.* **1996**, *100*, 3056.

[5] Yoshihara, K.; Tominaga, K.; Nagasawa, Y. *Bull. Chem. Soc. Japan* **1995**, *68*, 696.

[6] Marcus, R. A.; Sutin, N. *Biochim. Biophys. Acta* **1985**, *811*, 265-322.

[7] Jimenez, R.; Fleming, G. R.; Kumar, P. V.; Maroncelli, M. *Nature* **1994**, *369*, 471.

[8] Okamura, T.; Sumitani, M.; Yoshihara, K. *Chem. Phys. Lett.* **1983**, *94*, 339.

[9] Horng, M. L.; Gardecki, J. A.; Papazyan, A.; Maroncelli, M. *J. Phys. Chem.* **1995**, *99*, 17311.

[10] a) Jarzęba, W.; Walker, G. C.; Johnson, A. E.; Kahlow, M. A.; Barbara, P. F. *J. Phys. Chem.* **1988**, *92*, 7039; b) Jarzęba, W.; Walker, G. C.; Johnson, A. E.; Barbara, P. F. *Chem. Phys.* **1991**, *152*, 57;

[11] Wolynes, P. G. *J. Chem. Phys.* **1987**, *86*, 5133.

[12] Bagchi, B; Chandra, A. *J. Chem. Phys.* **1989**, *90*, 7338.

[13] King, G.; Warshel, A. *J. Chem. Phys.* **1989**, *91*, 3647.

[14] Carter, E. A.; Hynes, J. T *J. Chem. Phys.* **1991**, *94*, 5961.

[15] a) Maroncelli, M.; Fleming, G. R. *J. Chem. Phys.* **1988**, *89*, 5044; b) Maroncelli, M. *J. Chem. Phys.* **1991**, *94*, 2084.

[16] a) Carlson, H. A.; Jorgensen, W. L. *J. Phys. Chem.* **1995**, *99*, 10667; b) Tiradorives, J.; Maxwell, D. S.; Jorgensen, W. L. *J. Am. Chem. Soc.* **1993**, *115*, 11590.

[17] Sheu, W. S.; Rossky, P. J. *J. Phys. Chem.* **1996**, *100*, 1295.

[18] Aguilar, M. A.; Hidalgo, A. *J. Phys. Chem.* **1995**, *99*, 4293.

[19] Stratt, R. M.; Cho, M. H. *J. Chem. Phys.* **1994**, *100*, 6700.

[20] Allen, M. P.; Tildesley, D. J. *Computer Simulation of Liquids* (Clarendon Press, Oxford, 1987).

[21] Berkowitz, M.; McCammon, J. A. *Chem. Phys. Lett.* **1982**, *90*, 215.

[22] Blech, A. C.; Berkowitz, M. *Chem. Phys. Lett.* **1985**, *113*, 278.

[23] Brünger, A.; Brooks III, C. L.; Karplus, M. *Chem. Phys. Lett.* **1984**, *105*, 495.

[24] Wallqvist, A. *Molecular Simulation* **1993**, *10*, 13.

[25] Wang, L.; Hermans, J. *J. Phys. Chem.* **1995**, *99*, 12001.

[26] Mehta, A; Song, X.; Marcus, R. A. *In preparation.*

[27] Refson, K.; Pawley, G. S. *Mol. Phys.* **1987**, *61*, 669.

[28] Refson, K. *Moldy User's Manual* Rev. : 2.6.

[29] McQuarrie, D. A. *Statistical Mechanics* (HarperCollins Publishers, Inc., New York, 1976).

[30] Bernard, W.; Callen, H. B. *Rev. Mod. Phys.* **1959**, *31*, 1017.

[31] Jorgensen, W. L.; Chandrasekhar J.; Madura, J. D.; Impey, R. W.; Klein, M. L. *J. Chem. Phys.* **1983**, *79*, 926.

[32] Song, X.; Marcus, R. A. *J. Chem. Phys.* **1993**, *99*, 7768.

[33] Neumann, M *J. Chem. Phys.* **1986**, *85*, 1567.

[34] Watanabe, K.; Klein, M. L. *Chem. Phys.* **1989**, *131*, 157.

[35] Narten, A. H.; Levy, H. A. *J. Chem. Phys.* **1971**, *55*, 2263.

[36] Hsu, C.-P.; Song, X.; Marcus, R. A. *Submitted for Publication.*

Chapter 6

A Reaction Field Formulation of Solvent Dynamics

A Reaction Field Formulation of Solvent Dynamics

Aseem Mehta, Xueyu Song and R. A. Marcus

Arthur Amos Noyes Laboratory of Chemical Physics,
California Institute of Technology,
Pasadena, CA, 91125

Abstract

A reaction field (RF) formulation of the solvent dynamics problem is described. The solvent in a solute-solvent system is described by individual molecules to some distance r_c and beyond that by a dielectric continuum. Molecular dynamics calculations have been performed for an "oxygen-like" atomic solute with the TIP4P water solvent. Structural (radial and angular distribution functions) and solvational (equilibrium correlation and non-equilibrium response functions) results are presented that show the applicability of this method for solvent dynamics calculations. Comparison of results from the reaction field formalism with results from the periodic boundary conditions (PBC) and pure cluster formalisms are made to show the applicability of the RF formulation.

6.1 Introduction

With the experience obtained from MD simulations of solute-solvent systems with PBC that were presented in the previous chapter, we now present results from solvent dynamics simulation of a spherical cluster of the solute, fixed at the center of a spherical cavity, and solvent molecules surrounded by a dielectric continuum. This type of simulation has been referred to in the literature as the simulation of a water "droplet." The radius of the individual water clusters simulated is $7 - 10$Å.

The advantages of this type of simulation were outlined in chapter 5. First, use of a non-periodic system may be better for the solvation dynamics, particularly for charged solutes, since, unlike in PBC simulations, there is no unphysical change in the sign in the polarization of the solvent molecules at the cell edge. Also, this method is more physically intuitive since it allows for the separation of the solvent into the nearby molecular part and the distant dielectric part. This separation may make the understanding of the solvent dynamics possible by simulating using a much smaller number of molecules, and so this method may prove to be computationally less intensive. Finally, with future advances in theory, the use of actual complete dielectric dispersion curves, $\epsilon(\omega)$, for the continuum part of the solvent in MD simulations may be possible with this formulation. Use of the total dielectric dispersion curve $\epsilon(\omega)$ of the continuum part, together with molecular dynamics simulation of actual molecules describing the solvent to some distance, is probably the best approach to solvent dynamics since it would combine the most accurate formulation of the distant continuum type of solvent response together with a molecular description of the nearby solvent molecules.

From a technical point of view, the reaction field simulations have a number of similarities with the usual PBC calculations, as well as a number of differences that have to resolved before the simulations may be attempted. Some of these differences are in the potential energy function for the cluster, the boundary conditions to be imposed, methodology to calculate the radial distribution functions, and the position of the solute within the cluster. An issue of particular importance here concerns how

best to define the interface between the molecular cavity and the continuum. This topic arises because at the surface, as anywhere else, the charged particles are not in reality point charges but have an excluded volume associated with them. This surface of interaction requires special consideration in adapting the reaction field potential that is originally derived for point charges in a sphere.

These differences have necessitated a number of changes in the MolDy code that was used for the PBC calculations. It was advantageous to use MolDy since it was written in a modular format, thereby, helping considerably in the reprogramming. A number of modules were not altered since they required no change, whereas a number of modules were completely rewritten. In particular, the Ewald sum method that was used for the calculation of the long-range coulombic potential was replaced by the reaction field potential. Rather than periodic boundary condition, reflecting or 'LJ confining' boundary conditions (defined below) were used to confine the molecules in the cavity.

For solvent dynamics calculations, the reaction field method for a cavity in a dielectric continuum has not been applied as extensively as the PBC method. Wallqvist[1] has applied this method to simulate pure water clusters and obtained good agreement of the total solvational energy per molecule ($V/N = -41.5$ to $-41.7 kJ/mol$) with previous PBC calculations (-41.1 to $-41.9 kJ/mol$). Wang and Hermans[2] applied this method to a solute-solvent system. They focused on calculating the hydration free energy and did not report any correlation or solvent response functions that are central to comparison of simulations with experimental results.

The reaction field method has been utilized for some recent simulations of polar liquids. Lee and Warshel[3] report the use of the 'local reaction field' method where the reaction field potential, when written as an infinite series, is truncated after a few terms for evaluation of electrostatic energies in biomolecules such as proteins in water. Shang and Head-Gordon[4] have used a very simplified reaction-field treatment to study glycine and alanine dipeptides. In this study, only the dipole moment at the center of a spherical cavity of the solute charge distribution is used and all higher multipole terms are neglected. Tironi *et al.*[5] use a generalized reaction field method

to calculate the long-range electrostatic forces for their simulation of water-NaCl solution with periodic boundary conditions. This implementation of the reaction-field method is different from the one reported here because we have elected to avoid the use of periodic boundary conditions.

In the following sections, the various attempts to properly define the potential, the new boundary conditions, and the structural and dynamical results from these calculations are described.

6.2 Reaction Field Potential

For a system of charges $\{q_i\}$, $i = 1, \ldots, n$, in a spherical cavity surrounded by a dielectric continuum with a static dielectric constant ϵ, the electrostatic potential at any point within the cavity may be written as[6]

$$V = V_q + V_{rxn} \tag{6.1}$$

where, at any point $\vec{r}$, defined by r, θ, ϕ, within a cavity of radius a,

$$V_q(r) = \sum_{i=1}^{n} \frac{q_i}{|\vec{r} - \vec{r_i}|}, \tag{6.2}$$

$$V_{rxn}(r) = -\sum_{i=1}^{n} \frac{q_i}{a} \sum_{l=0}^{\infty} \frac{(\epsilon - 1)(l+1)}{l + \epsilon(l+1)} \left(\frac{r r_i}{a^2}\right)^l P_l(\cos\gamma_i), \tag{6.3}$$

with the P_ls being the Legendre Polynomials with arguments

$$\cos\gamma_i = \cos\theta\cos\theta_i + \sin\theta\sin\theta_i\cos(\phi - \phi_i). \tag{6.4}$$

This result is well known from electrostatics and is obtained from the solution of the Poisson equation such that the total potential and its derivative behaves appropriately as $r \to \infty$ and at the interface of the cavity and the continuum. In brief, this result may be obtained by proceeding, as Kirkwood did[7], to solve Laplace's equation for the potential at any point in space due to a set of point charges in a cavity surrounded

by a continuum. The above solution is obtained by writing the potential in spherical coordinates and imposing the required boundary conditions to the potential and its gradient at $r = \infty$ and at the cavity-continuum boundary $r = a$.

However, a potential written as an infinite series is not appropriate for molecular dynamics, since the infinite series has to be summed continuously to obtain the potential energy and the forces that act on the individual charges. There is no closed form solution for the above V_{rxn} and our first approach was to use a Pade approximation[8] to the infinite series by explicitly calculating the first few (≈ 8) terms. The accuracy of the approximation was tested and was found lacking.

It is useful to note that the above formulation of V_{rxn} is simply the generating function for the Legendre polynomials except for the multiplicative term that is a function of ϵ and l. To take advantage of the generating function for Legendre polynomials, the multiplicative term was simplified by expansion. For large ϵ (such is the case with water $\epsilon \approx 78$), we may expand, as Friedman did[9], $\frac{(\epsilon-1)(l+1)}{l+\epsilon(l+1)}$ in a Taylor series about $\frac{1}{\epsilon+1} = x \approx 0$.

$$\frac{(\epsilon-1)(l+1)}{l+\epsilon(l+1)} = \frac{(\epsilon-1)}{(\epsilon+1)} \cdot \frac{1}{1-\frac{x}{l+1}} = \frac{(\epsilon-1)}{(\epsilon+1)} \sum_{i=0}^{\infty} \left(\frac{x}{l+1}\right)^i \tag{6.5}$$

Retaining upto and including quadratic terms in $\frac{1}{\epsilon+1}$ and simplifying, we have

$$\frac{(\epsilon-1)(l+1)}{l+\epsilon(l+1)} \approx \frac{\epsilon-1}{\epsilon+1} + \frac{\epsilon-1}{(\epsilon+1)^2(l+1)}. \tag{6.6}$$

In Figure 6.1 the left side of equation 6.6 and its approximation by the Taylors expansion are shown together for comparison. This approximation is critical, since it permits V_{rxn} to be written in closed form because with this simplification, we have

$$V_{rxn}(r,\theta,\phi) = -\sum_{i=1}^{n} \frac{q_i}{a} \frac{\epsilon-1}{\epsilon+1} \left[\sum_{l=0}^{\infty} \left(\frac{rr_i}{a^2}\right)^l P_l(\cos\gamma_i) + \frac{1}{\epsilon+1} \sum_{l=0}^{\infty} \frac{1}{l+1} \left(\frac{rr_i}{a^2}\right)^l P_l(\cos\gamma_i) \right]. \tag{6.7}$$

An analytic expression can be obtained for the two infinite sums in the previous equa-

tion by using the definition of the generating function of the Legendre Polynomials[10]

$$g(t,s) = \sum_{l=0}^{\infty} t^l P_l(s) = (1 - 2st + t^2)^{-\frac{1}{2}}, |t| < 1. \tag{6.8}$$

After some straightforward mathematical manipulation we obtain

$$\begin{aligned} V_{rxn}(r,\theta,\phi) &= -\sum_{i=1}^{n} \frac{q_i}{a}\frac{\epsilon-1}{\epsilon+1}\left(1 - 2\left(\frac{rr_i}{a^2}\right)\cos\gamma_i + \left(\frac{rr_i}{a^2}\right)^2\right)^{-\frac{1}{2}} \\ &-\sum_{i=1}^{n} \frac{q_i}{a}\frac{\epsilon-1}{(\epsilon+1)^2}\left(\frac{rr_i}{a^2}\right)^{-1} \ln\left|\frac{\left(\frac{rr_i}{a^2}\right) - \cos\gamma_i + \left(1 - 2\left(\frac{rr_i}{a^2}\right)\cos\gamma_i + \left(\frac{rr_i}{a^2}\right)^2\right)^{\frac{1}{2}}}{1 - \cos\gamma_i}\right| . \end{aligned} \tag{6.9}$$

It is useful to note that in Cartesian coordinates

$$rr_i \cos\gamma_i = xx_i + yy_i + zz_i = \vec{r}\cdot\vec{r_i}. \tag{6.10}$$

Molecular dynamics simulations require the forces on each particle at every time step such that Newton's equations of motion can be integrated. The electrostatic forces at site j with charge q_j are obtained directly from the potential by using

$$\vec{F_j} = (F_x, F_y, F_z)_j = -q_j \nabla V(x_j, y_j, z_j). \tag{6.11}$$

6.3 Lennard-Jones Potential

The L-J part, V_{LJ}, of the potential energy function is also important for a correct characterization of the liquid. V_{LJ} is particularly important at small distances, where it is used to incorporate the molecular nature (excluded volume) of the particles through the repulsive part of V_{LJ}. The structure of the liquid as determined by the radial distribution function (RDF) defined in chapter 5 is strongly dependent upon the parameters in V_{LJ}. The parameters used for these calculations for the water molecules are the same as they were for the PBC systems. The total V_{LJ} experienced

by any particle in the cavity may be written as

$$V_{LJ}(\vec{r}_i) = V_{LJ}^{cont}(\vec{r}_i) + V_{LJ}^{d}(\vec{r}_i) \tag{6.12}$$

where $V_{LJ}^{d}(\vec{r}_i)$, the direct L-J potential is simply

$$V_{LJ}^{d}(\vec{r}_i) = \sum_j \epsilon \left[\left(\frac{\sigma}{|\vec{r}_i - \vec{r}_j|} \right)^{12} - \left(\frac{\sigma}{|\vec{r}_i - \vec{r}_j|} \right)^{6} \right] \tag{6.13}$$

and $V_{LJ}^{cont}(\vec{r}_i)$ denotes the contribution from the continuum enclosing the cavity.

To incorporate the molecular nature of the continuum, the L-J potential from the continuum, $V_{LJ}^{cont}(\vec{r}_i)$, was also included by assuming a uniform distribution of L-J particles outside the cavity, with ρ being the density,

$$\begin{aligned} V_{LJ}^{cont}(\vec{r}_i) &= \sum_{j|r_j>a} V_{LJ}^{ij}(\vec{r}_i) \\ &\approx \int_{|r|>a} \rho d\vec{r} V_{LJ}(\vec{r}) \\ &= \epsilon\rho \int_{|r|>a} d\vec{r} \left[\left(\frac{\sigma}{|\vec{r}_i - \vec{r}|} \right)^{12} - \left(\frac{\sigma}{|\vec{r}_i - \vec{r}|} \right)^{6} \right]. \end{aligned} \tag{6.14}$$

Using $|\vec{r}_i - \vec{r}| = \sqrt{r^2 + r_i^2 - 2rr_i cos\gamma}$ and $d\vec{r} = r^2 \sin\theta dr d\theta d\phi$, we integrate over ϕ, θ and r to obtain for a L-J particle at a distance of r_i from the center of the cavity

$$\begin{aligned} V_{LJ}^{cont}(r_i) = \frac{\pi\epsilon\rho\sigma^3}{4r_i} \Bigg[& \left(a - \frac{r_i}{9}\right) \left(\frac{\sigma}{a - r_i}\right)^9 \frac{1}{10} - \left(a + \frac{r_i}{9}\right) \left(\frac{\sigma}{a + r_i}\right)^9 \frac{1}{10} - \\ & \left(a - \frac{r_i}{3}\right) \left(\frac{\sigma}{a - r_i}\right)^3 + \left(a + \frac{r_i}{3}\right) \left(\frac{\sigma}{a + r_i}\right)^3 \Bigg]. \end{aligned} \tag{6.15}$$

In Figure 6.2, $V_{LJ}^{cont}(r_i)$ is shown as a function of r_i for the values of ϵ, σ and ρ that are appropriate for TIP4P water. Later, we explain how an appropriate value for a is obtained for a given cluster. In Figure 6.2, $a = 9.0$ Å was used.

The forces are obtained from the gradient of the potential.

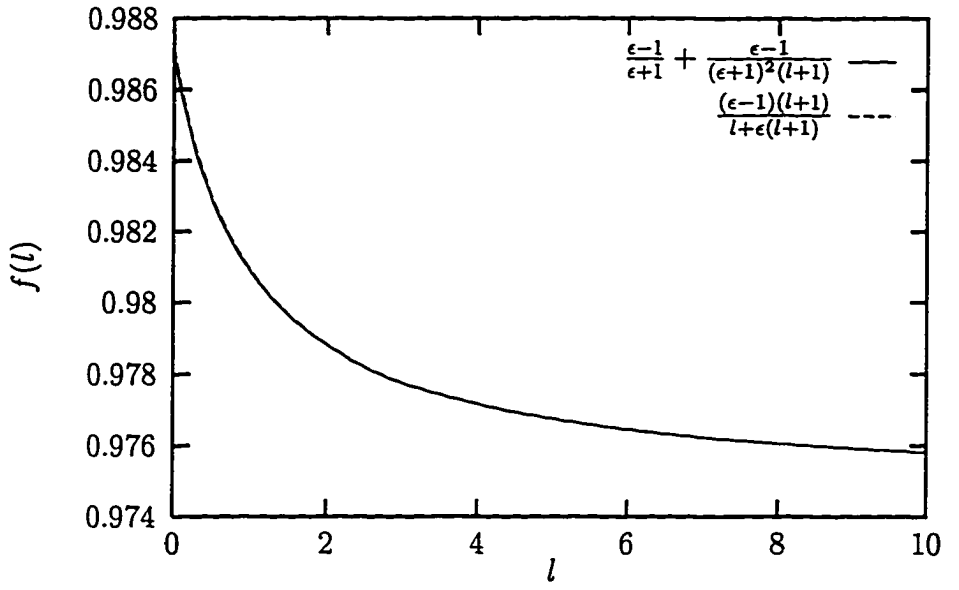

Figure 6.1: $\frac{(\epsilon-1)(l+1)}{l+\epsilon(l+1)}$ and its approximation by a taylor's expansion

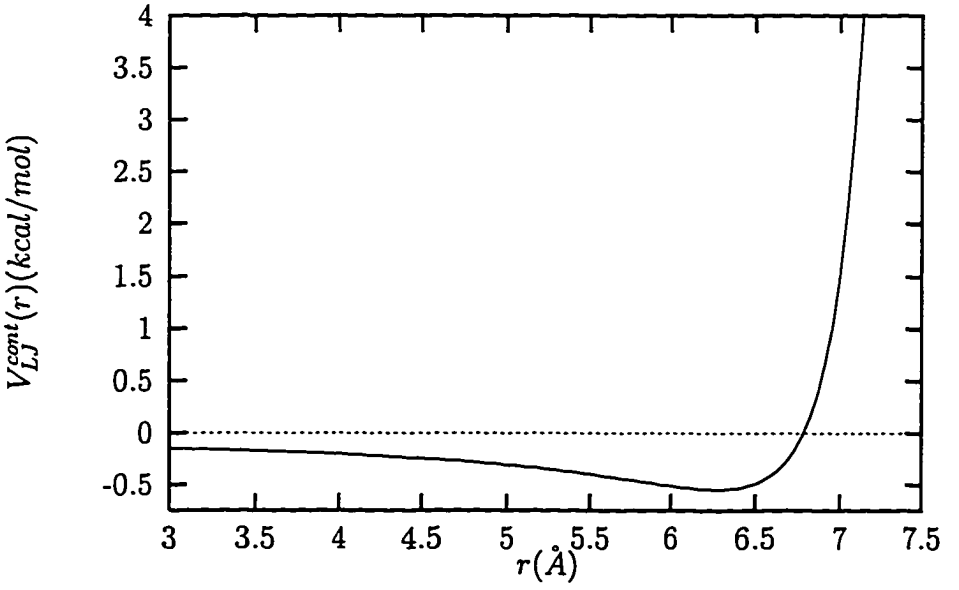

Figure 6.2: Lennard-Jones contribution of the continuum

6.4 Boundary Conditions

Unlike the PBC system, a cavity embedded in a continuum formalism requires that there be a transition in properties at the interface. A simple formulation of this method would be to use a spherical cavity with reflecting boundary conditions, with the continuum beginning immediately outside the cavity. However, the particles inside the cavity are not point charges and so it is unphysical for them to approach the cavity-continuum surface. There are two reasons why this formalism represents an unphysical situation. First, if the continuum is considered to represent a uniform distribution of water molecules outside the cavity, the molecular nature of the solvent should disallow the water molecules in the cavity to come too close to the cavity surface due to excluded volume of the continuum particles. From a technical standpoint, if the continuum starts at the point upto which the charged particles are allowed to come, then the reaction field potential becomes singular when the rr_i/a^2 term in the electrostatic potential function approaches 1. This singularity precludes the successful propagation of the equations of motion by making the forces diverge at the boundary.

Two different methods were tried for solving this problem. In the first method the cavity with the water molecules was further surrounded by a shell of water molecules that were frozen at their positions. The shell prevented the particles inside the cavity from approaching the continuum boundary and, therefore, allowed for a successful propagation of the equations of motion for the non-frozen particles. The frozen shell, however, is physically quite artificial and created new problems, particularly with respect to the conservation of kinetic energy. We describe the frozen shell method and results in the next section.

The second method used for ensuring a correct description of the molecules near the surface was based upon the use of $V_{LJ}^{cont}(r)$, described earlier. This method allowed for a natural and self-consistent determination of an appropriate value for a such that the reaction field potential was well behaved at the surface. This approach was based upon exploiting the excluded volume of the molecules in the continuum that prevents

the cavity molecules from approaching the continuum too closely.

6.4.1 'Frozen Shell' Scheme

With the above described potential energy function, without V_{LJ}^{cont}, molecular dynamics simulations were executed within the spherical cavity. As shown below, space was divided into three parts : region A : a $7-9$ Å radius cavity filled with solute molecule and the solvent molecules at the appropriate density ; region B : a $2-3$ Å shell that surrounds the above cavity with frozen solvent molecules to characterize the surface of interaction between the cavity and region C : a dielectric continuum.

A 9 Å cavity has approximately 100 molecules of water in it and a 2 Å shell that surrounds it has about 80 more. For the molecules within the inner cavity, the potential $V = V_{LJ}^{d} + V_q + V_{rxn}$ is used to obtain the forces at each timestep and to then propagate the equations of motion.

The RF term of the potential energy function in equations 6.7 and 6.9 diverges as $r \rightarrow a$, and the forces on the particles near the surface $r_i \approx a$ may become quite large. The reaction field, to a first approximation, acts as an image charge of the opposite sign in the continuum. Near the surface, the interaction of a charge with its image, an attractive term, dominates the potential and it diverges. Since a rigid model is used for water, these large forces impose large torques on the individual molecules near the surface, and make the propagation of the equations of motion difficult. By requiring that there be 2 Å shell of frozen molecules between the cavity and the continuum, r is constrained to be less that a and these large impulsive forces due to the singularity of the potential near the surface are avoided. The molecules in the shell are kept frozen during the calculation by setting all the forces acting on them and their velocities to zero.

In this type of calculation, the boundary of the cavity was kept rigid. If the center of mass of any molecule attempted to escape the cavity, then the center of mass was reflected back into the cavity and its translational velocity $v_{old} = v_{\parallel} + v_{\perp}$ was changed to $v_{new} = v_{\parallel} - v_{\perp}$. This method of confinement is similar to the one used

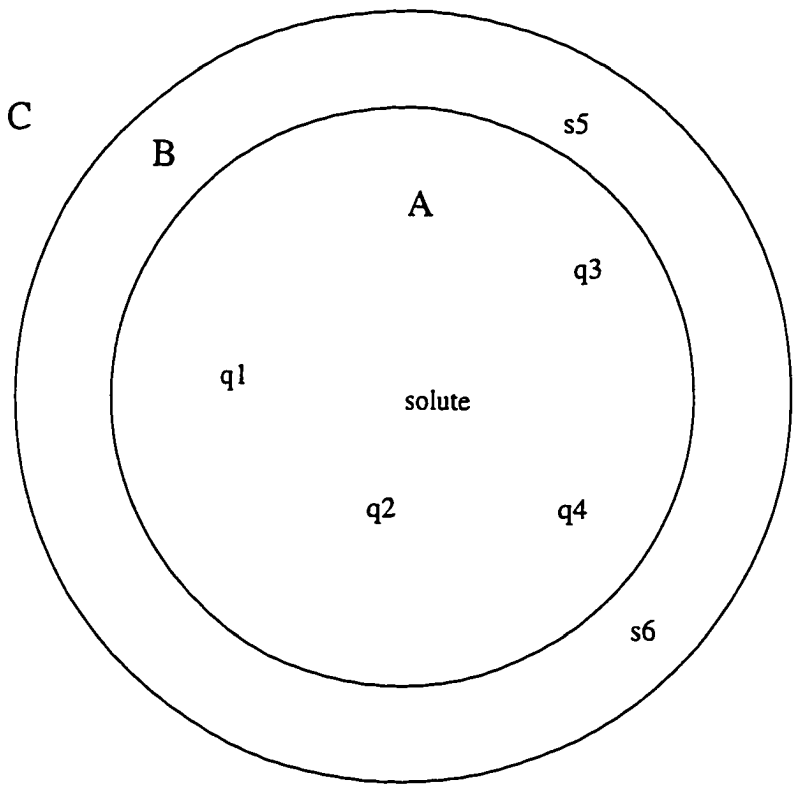

Figure 6.3: Division of space into cavity, shell and continuum in the 'Frozen Shell' scheme

by Maroncelli[11] where a large cluster was used to simulate the liquid with similar confinement to prevent evaporation.

6.4.2 'LJ confinement' scheme

As described later, the frozen shell method has unintended physical effects on the particles inside the cavity, such as the gradual freezing of the liquid. To mitigate such effects the repulsive wall of the continuum LJ potential ($V_{LJ}^{cont}(r)$) was used to confine the particles inside the cavity. This scheme is similar to the one used by Wang and Hermans[2] and by Wallqvist[1] in their study of water with reaction field boundary conditions. Briefly, the implementation is as follows: A cluster of solute molecule and the solvent molecules are governed by the potential $V = V_{LJ}^{d} + V_{LJ}^{cont} + V_{rxn} + V_{q}$. Given that we wish to simulate some n molecules, it is not transparent as to where this wall should be located such that a correct description of the solution is obtained. The position of the wall is uniquely determined by the parameter a in equation 15. We determined the value of a is a self-consistent fashion. The simulation was started from a PBC simulation, from which a cavity of size a' was carved out. The simulations were executed for a variety of values of x, where $a = a' + x$. In Figure 6.3, the radius of region A has radius of a', and region A + B has radius of a. Unlike the frozen shell scheme, in the 'LJ confinement' scheme the region B is not filled with frozen solvent molecules. For small values of x, the V_{LJ}^{cont} compressed the fluid too much. The value was systematically changed until the RDF obtained was of good quality. The availability of the RDF for the TIP4P potential from a variety of good quality calculations allowed this comparison to be made. This self-consistent scheme may be seen as an empirical way of obtaining the excluded volume of the cavity water molecules that keeps the continuum some distance away. The value of x required for a good description of the solution was ~ 2.25Å.

6.5 Results

6.5.1 Solvational and Structural Quantities Calculated

The main output of the simulation is the time dependent electrostatic potential acting on the solute due to the solvent, $V(t) \equiv V^e_{int}(t)$, or the solute-solvent interaction energy ($E_{int}(t) = E^e_{int}(t) + E^{LJ}_{int}(t)$). They are used to calculate the equilibrium time correlation function (tcf) and the non-equilibrium response function, respectively :

$$C(t) = \frac{\langle \delta V(t) \delta V(0) \rangle}{\langle \delta V(0) \delta V(0) \rangle} \tag{6.16}$$

$$S(t) = \frac{E_{int}(t) - E_{int}(\infty)}{E_{int}(0) - E_{int}(\infty)}, \tag{6.17}$$

quantities that are related to each other by linear-response theory and may be directly compared to experimental results. As discussed in Chapter 5, equation 6.17 is rigorously correct only when $E_{int}(t)$ is replaced by $V(t)$[11] or by $E^e_{int}(t) = q_{solute} V^e_{int}(t)$. However, $E^{LJ}_{int}(t)$, the other component of $E_{int}(t)$, is only a small part of $E_{int}(t)$ and is relatively constant throughout the trajectory which removes it from the numerator and denominator of equation 6.17.

Molecular positions were obtained for calculating the radial distribution functions. The radial distribution functions are key quantities since they allow for an unambiguous determination of whether the liquid being simulated has the correct structural properties. The calculational method used was similar to the one described for the PBC system, slightly modified[12] due to the spherical nature of the cavity. Also, the angular distribution function,

$$h(cos\theta) = \left\langle \sum_i \delta \left(\cos\theta - \cos\theta_i \right) \right\rangle, \tag{6.18}$$

where θ_i is the angle between $\vec{\mu}_i$, the dipole vector, and $\vec{r}_i$, the vector joining the origin of the dipole to the center of the cavity, was calculated to determine whether the solvent molecules had any preferential orientation.

6.5.2 Frozen Shell Results

As previously mentioned, an unintended effect of keeping the shell molecules fixed is that the shell acts as an infinite energy sink. As $t \rightarrow \infty$ the frozen shell would completely arrest all molecular motion by forcing orientational order upon the polar solvent molecules. For the $\approx$ 100ps timescale calculations that we perform, the degree to which the frozen shell decreases the total kinetic energy of the system depends solely on the actual configuration of the shell molecules and in the calculations that have been performed, the effect of this frozen shell has varied considerably. The magnitude of the effect is determined by following the total kinetic energy of the system as a function of time. A particularly egregious example of this behavior is shown in Figure 6.4 for a 75ps trajectory.

This decay of kinetic energy (or freezing of the solution) causes the RDF to show a solid structure rather than being appropriate for a liquid. It also has an effect on the correlation function $C(t)$. The effect on the correlation function can be best understood in the limit when there is no solvent motion. In that case E_{int} and $V(t)$ are constant and $C(t)$ is completely correlated at all times. Similarly, slowing of the solvent molecules due to the frozen shell increases the extent of $\delta V(t)$ correlation and is shown clearly in Figure 6.5, where the comparison between correlation functions from different parts of the trajectory is made. It is clear that with the decay in total kinetic energy of the system, $C(t)$ becomes more and more correlated.

Such untrustworthy results, caused by the unphysical frozen shell approximation, necessitated a more robust description of the cavity-continuum interface, which is described in sections 6.4.2 and 6.5.3.

6.5.3 Structural Results from 'LJ confinement' simulations

Clearly, the frozen shell scheme is faulty. A remedy for this predicament is either to make the frozen shell dynamic (*i.e.*, not frozen) or to remove it. Making the frozen shell dynamic would require a new force field for the molecules in the shell. Use of a new force field for the shell molecules would simply cause further parameterization

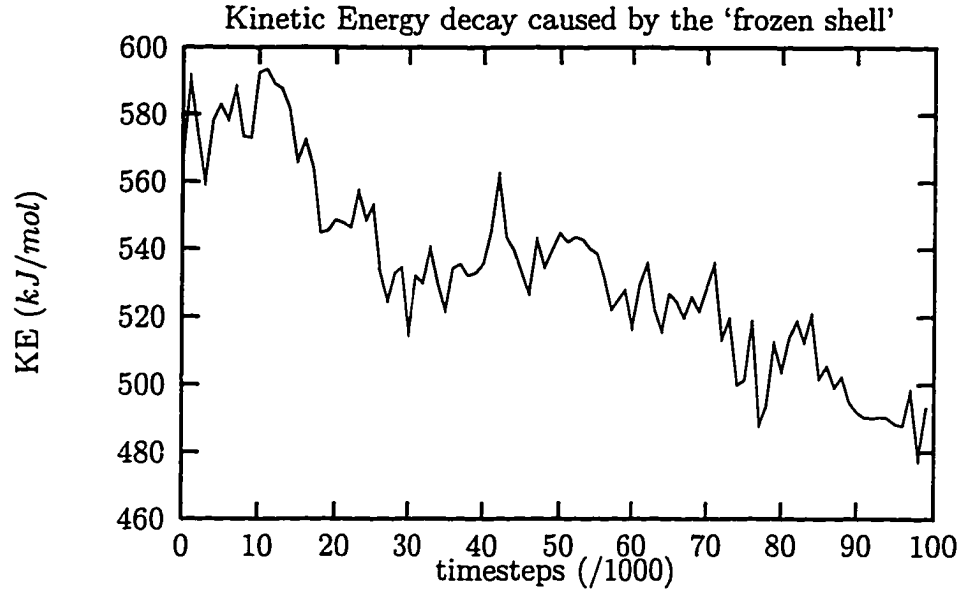

Figure 6.4: Kinetic Energy decay of particles in cavity caused by the 'frozen shell'

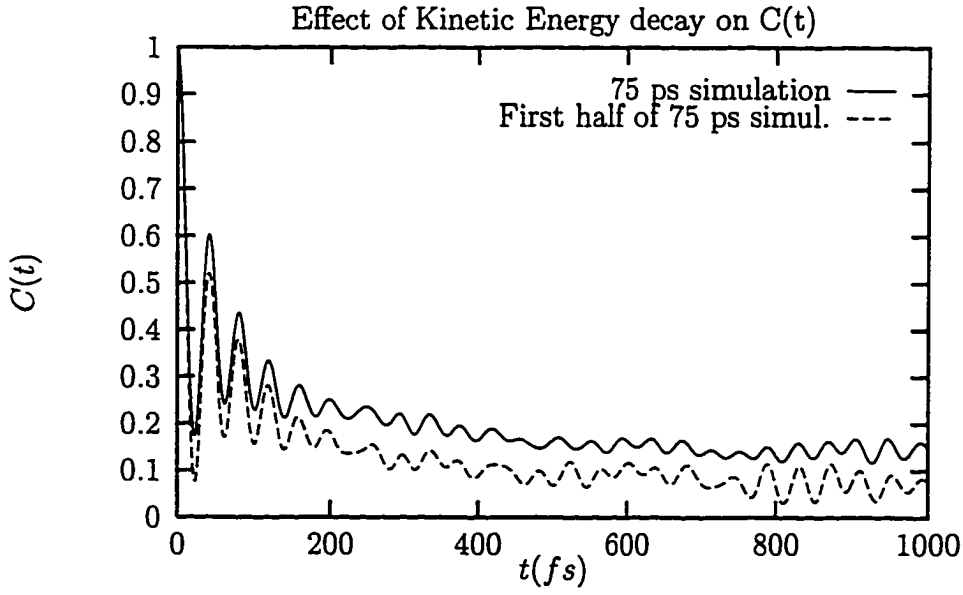

Figure 6.5: Increase in correlation of solvent response function caused by the Kinetic Energy decay

of the problem without giving any substantial benefit.

We decided to remove the shell and confine the cavity particles using V_{LJ}^{cont}. The excluded volume of the surface particles forces the continuum to begin some distance away from the surface particles, thereby automatically solving the problems that arise when the particles come too close to the surface and cause $V_q^{cont}(r)$ to become unphysically large. It obviates the need of solutions such as the frozen shell.

In presenting the results with this LJ method for avoiding the singularities, the various radial distribution functions (RDFs) are presented first, since they provide a sensitive probe of the solvent structure. In Figure 6.6, the O-O RDFs are shown for TIP4P water molecules confined in three different cavity sizes.

This result shown in Figure 6.6 has two noteworthy features. First, the results from the three different sized simulations are quite similar. This shows that our calculations have converged and are no longer dependent upon the size of the cavity. Secondly, the distribution functions are close to the ones obtained through the PBC simulations and by other researchers in previous work. Upon close comparison, shown in Figure 6.7 of the RF RDFs with the PBC RDF, it is found that while the curves are almost identical for $r \geq 3$Å, the initial peak of the RF RDF is slightly more pronounced and is broader, even though its position is correct. The stronger initial peak for the RF calculation may be due to slight excessive compression from V_{LJ}^{cont}. Fine tuning of the parameter a (defined earlier) should remove this effect by making the position of the L-J wall approximately 2.3-2.4 Å, rather than 2.25 Å that was used here. The L-J wall that arises from V_{LJ}^{cont} (see Figure 6.2) confines the water molecules in the cavity and has to be carefully calibrated to avoid confining the water molecules to too small a volume.

Shown in Figure 6.8, is the H-H RDF for a variety of cavity sizes that also displays the characteristics of a converged quantity. The H-H RDF does not approach 1 for $r = 4-6$Å because of a technicality with the RDF calculational method[12] that arises due to the difficulty in estimating the volume of the region in which the hydrogen molecules are confined.

The angular distribution function $h(\cos\theta)$, as defined above, of the solvent molecules

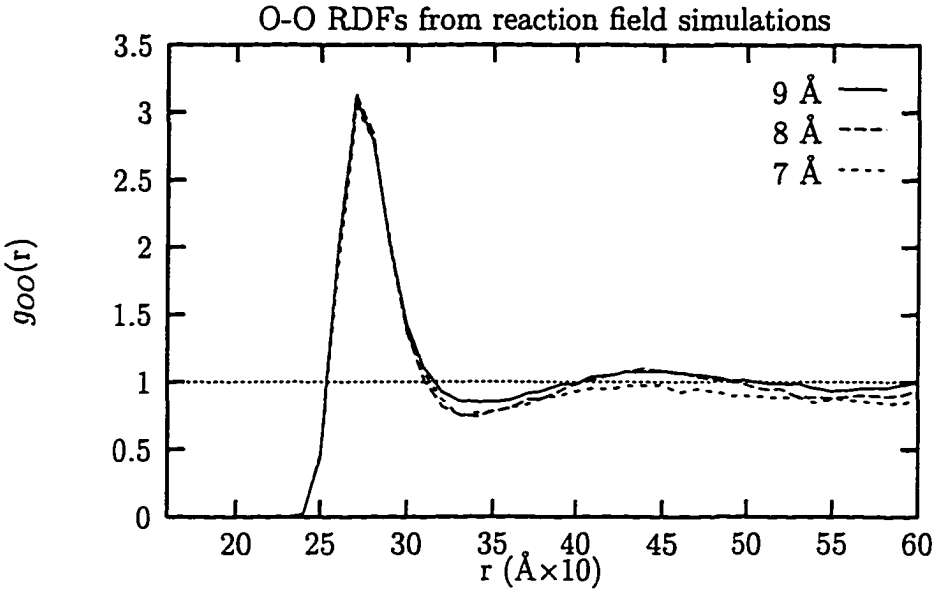

Figure 6.6: Convergence of the O-O RDF as a function of cavity radius

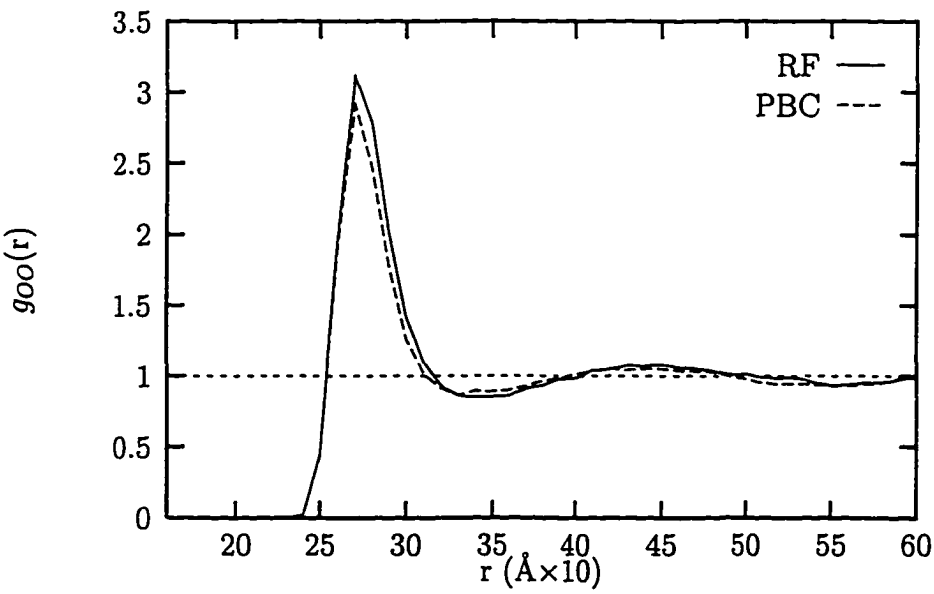

Figure 6.7: Comparison of the O-O RDF obtained from a RF and PBC calculations

around a neutral solute is shown in Figure 6.9.

In Figure 6.9 the convergence of the results as a function of cavity size is still evident. The plot shows that the solvent molecules, even in the presence of a neutral solute, show a slight orientational preference in a cavity. The individual dipoles, approximating the solvent molecules, are more likely to line up perpendicular to the line joining the position of the dipole to the center of the cavity ($\cos\theta = 0$) than lining up parallel to it ($\cos\theta = \pm 1$). Maroncelli et al.[11] in their work also report and cite this phenomenon concerning orientational preference of polar molecules near the surface of spherical cavities in the absence of a solute. They also observe similar orientational behavior for the nearest solvational shells in the presence of a neutral solute. We speculate that the presence of the solute molecule at the center of the sphere disturbs the hydrogen bonding structure for those dipoles that point directly to and away from the center. This phenomenon would favor the solvent dipoles to lie perpendicular to the vetor joining the dipole to the center of the cavity and together with the preference of the dipoles near the surface to lie parallel to the surface to also maximize the total hydrogen bonding interaction with other molecules, probably causes this orientational behavior. For water, when the dipoles lie parallel to the surface the hydrogen bonding with other molecules in the cavity is maximaized.

It is encouraging to see that the structural results that may be inferred from the RDFs from relatively small cavities are quite similar to each other. Cavities of radii 7, 8 and 9 Å have approximately 50, 75 and 110 water molecules respectively. This consistency provides the hope that it would be possible to obtain reliable and reproducible solvent dynamical results by using small cavities to provide the molecular nature of the solvent and with the reaction field providing the long-range coulombic potential. Use of the RF formalism may, in the future, significantly reduce the computational time of solvent dynamical quantities for a variety of solvent-solute systems.

Finally, three results that show the effects of a charged or uncharged solute on solvent structure are presented. First, the O-O RDF (g_{oo}(r)) is shown when there is a neutral or positively charged solute at the center of the cavity.

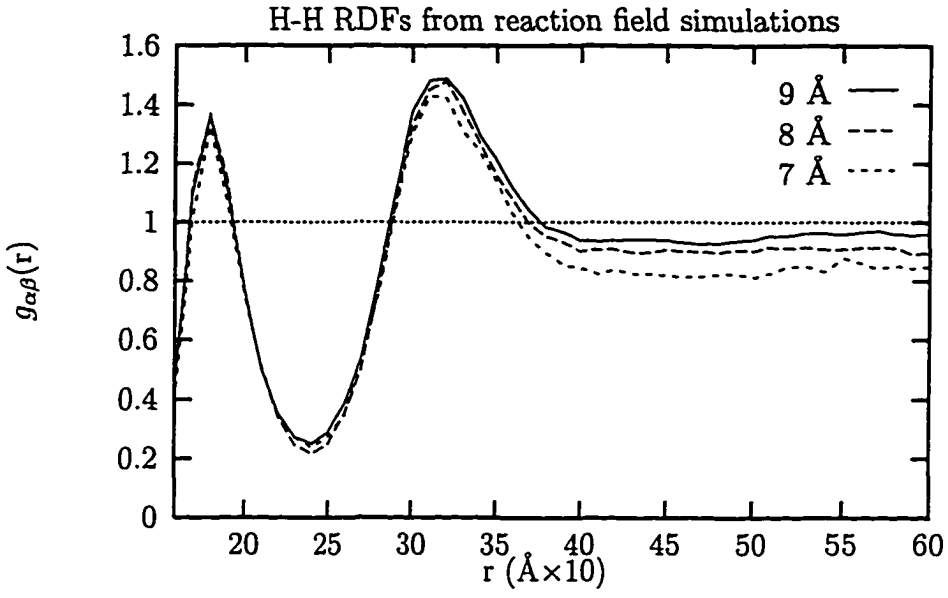

Figure 6.8: Convergence of the H-H RDF as a function of cavity radius

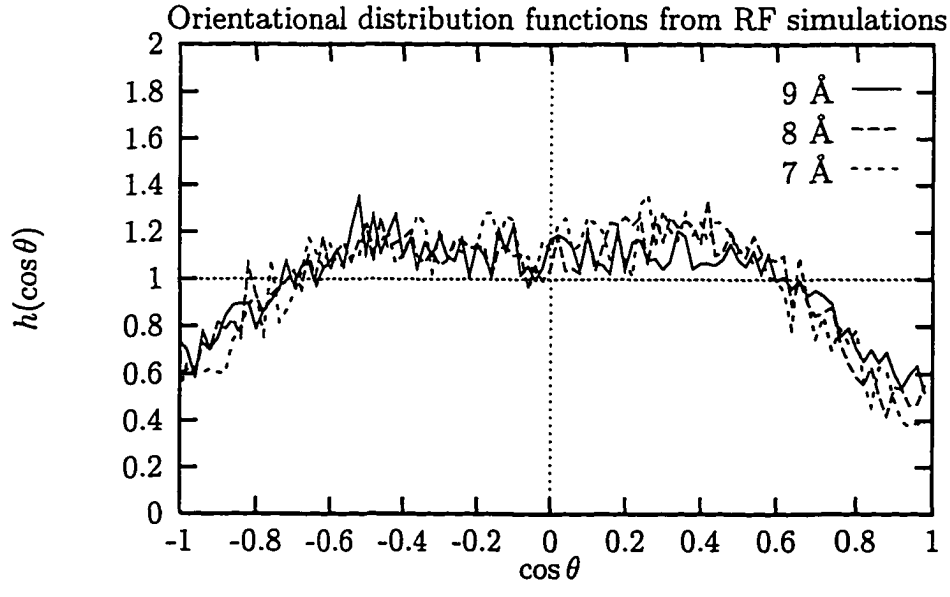

Figure 6.9: Convergence of $h(\cos\theta)$ as a function of cavity size

Figure 6.10 shows that a charge on the solute has no effect on $g_{oo}(r)$. The $g_{oo}(r)$ is a bulk quantity that depends on *all* the pair distances between individual oxygen atoms in the solvent molecules and should be negligibly affected by the presence of a single solute particle. The fact that these two curves shown above are almost identical shows that, at least for cavities of size 9 Å or more, the bulk properties of the solvent are not influenced by the solutes.

However, the presence of a charged solute in a polar solvent does polarize the solvent. Figures 6.11 and 6.12 show the extent to which a charged solute changes the orientational distribution function of the solvent ($h(\cos\theta)$, defined above) and the oxygen-solute (O-X) RDF when these quantities are compared with those from arising from a neutral solute.

Figure 6.11 clearly shows the expected result that the positively charged solute attracts the negetively charged oxygen of the solvent molecules closer to itself. The first solvational shell is significantly more prominent and well defined for the charged solute when compared to the uncharged one.

The orientational sturcture of the solvent molecules around the solute is made non-symmetrical by the positively charged solute. Unlike the $h(\cos\theta)$ around the neutral solute, which is almost symmetric about $\cos\theta = 0$ or $\theta = 90°$, the orientational DF for the positively charged solute is non-symmetrical. The positive charge causes the individual solvent dipoles to point away from the solute. Taking a larger configurational average during the calculation of $h(\cos\theta)$ should smoothen the jaggedness of the curves in Figure 6.12 and more clearly show the symmetrical nature of the $h(\cos\theta)$ curve for the neutral solute.

6.5.4 Solvational Results

With all the preliminary calculations providing confidence in the reaction field approach to the simulation of polar solvents, the main solvent dynamical results are now presented. All the results presented here are from the simulations that have used the 'LJ confinement' boundary conditions with a solute that has the LJ parameters

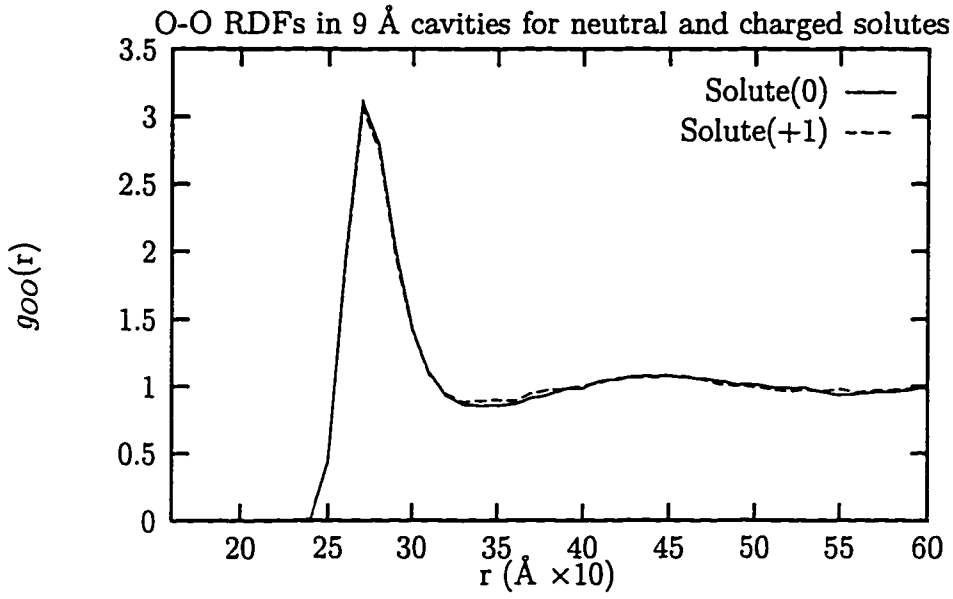

Figure 6.10: Independence of O-O RDF on the charge of the solute

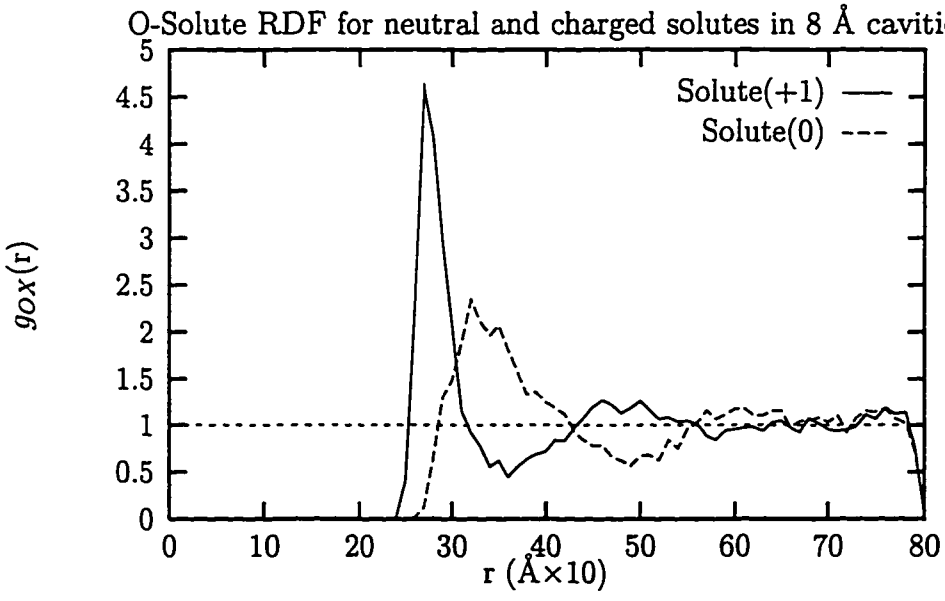

Figure 6.11: Attraction of oxygen atoms by a positively charged solute compared to a neutral solute

of a TIP4P oxygen atom.

The first results presented are for the time-correlation functions tcfs, $C(t)$, that provide the solvation response due to change in the solute's charge when linear response approximation is applicable. To calculate a "$V(t)$," the electrostatic interaction energy between solute and solvent, for neutral solutes, a fictitious unit test charge is placed on the solute and the interaction energy is calculated at every timestep while performing the dynamics for a neutral solute.

In Figure 6.13 the tcf for a neutral solute fixed at the center of the cavity is shown. The results for 7, 8 and 9 Å cavity sizes show remarkable similarity, indicating that the reuslts obtained are independent of cavity size and have converged for $t \leq 200fs$. Averaging the correlation function $C(t)$ over longer trajectories should smooth out the $t > 200fs$ oscillations. It is evident that a limited cavity size does not appear to cause systematic errors in our simulations. The tcf shows all the characteristics of the solvent response function of a "atomic" type solute. The fast initial decay of $C(t)$ to ~ 0.2 is followed by a slower and oscillatory decay of $C(t)$ to 0 in $\sim 500 - 700fs$. The fast component has been ascribed to the "inertial" motion of the solvent molecules that occurs due to the instantaneous change in the electrical property of the solute and has been uncovered only recently through realistic MD simulations[13] and also experimentally[14] through the availability of fast lasers. In an equilibrium simulation, this fast response occurs in the tcf due to the rotational motion of the solvent at $ca.300K$, the temperature at which the simulation is executed. This fast response is less dominant for larger solutes such as large dye molecules usually used in experiments because the solvent coordination shell are less well defined for them. But even for larger solutes the fast decay component is responsible for decreasing the C(t) to 0.5. The later, slower and oscillatory decay of $C(t)$ to 0 in $\sim 500 - 700fs$ corresponds to the diffusive (or translational) motion of the solvent. This result shows unambiguously that solvation response of $\sim$ 50fs timescale is a dominant feature of aqueous solvent dynamics. This fact is expected to have implications for charge transfer[15] and other types of chemical reactions that occur in the condensed phase and involve considerable solvent reorganization.

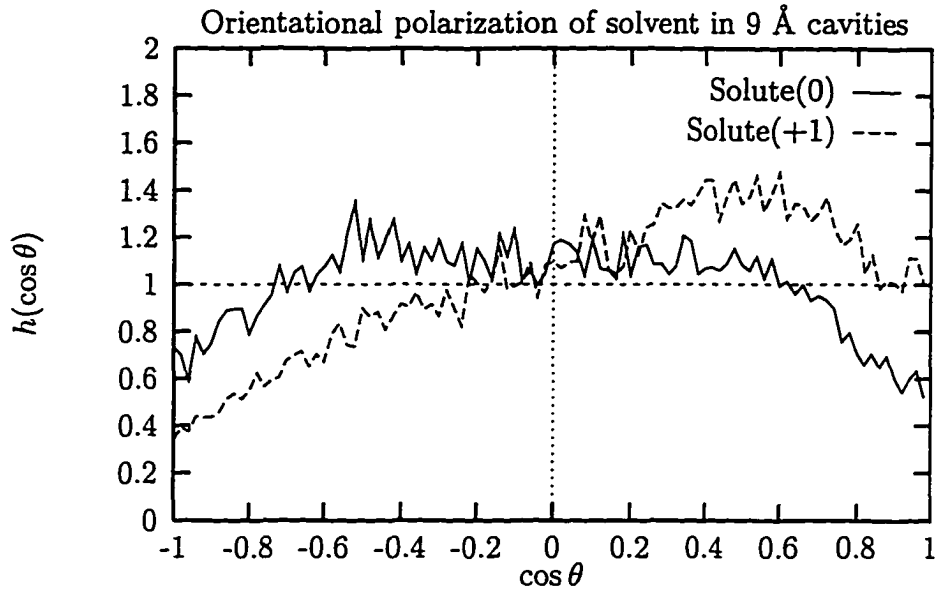

Figure 6.12: Polarization of water molecules by a positively charged solute

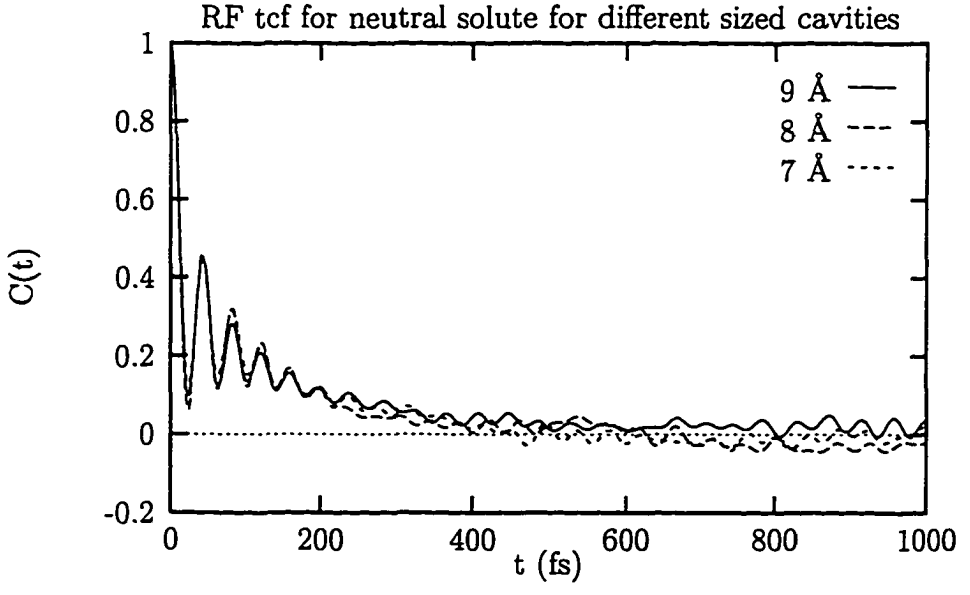

Figure 6.13: $C(t)$ for neutral solute calculated with the reaction field formalism

The *tcf* for the charged solute, shown in Figure 6.14, shows slower decay than that of the neutral solute. We have argued that the fast, initial decay of the neutral solute *tcf* was due to the inertial (or rotational) motion of the solvent molecules and the slower (> 0.1ps) decay was due to the diffusive (translational) motion of the solvent molecules. The rotational motion occurs without substantial change in the position of the solvent molecules' center of mass while the translational motion causes the solvational shells to break and reform. Comparing the charged and the neutral solvent *tcf*s, it is evident that the faster decay has been curtailed in the former case. For polar solvents, the charged solute is much more efficient at ordering the solvent molecules by imposing an orientational preference on the solvent as already shown by the angular distribution function. This charge-dipole attraction limits the rotational freedom of the solvent molecules. Therefore, proportionally, the fast component of the total decay of the $C(t)$ is smaller and the slower translational component is larger for the charged solute when compared with the neutral solute. Also, the slight recurrence in the *tcf* of the charged solute at $\sim 0.15 - 0.2$ps has been noticed earlier in PBC calcualations in Chapter 5 and by other researchers[11]. It has been argued that this recurrence is caused by the collective breathing motion of the innermost solvational shell of the charged solute.

In Figure 6.15 we show the solvation response function, averaged over five individual simulations, $\langle S(t) \rangle$ using the method described earlier in chapter 5. In brief, the solute charge in an equilibrated trajectory is suddenly changed from zero to $+1$. The total solute-solvent interaction energy is calculated at every time-step as the solvent rearranges itself to return to equilibrium with the charged solute. The time-dependent solute-solvent interaction energy is used to calculated $S(t)$ as in equation 6.17. The value of $E_{int}(\infty)$ used in the calculation of $S(t)$ is $\langle E_{int}(t) \rangle$ obtained from an equilibrated trajectory of a charged solute and solvent molecules.

Some noteworthy features of the above figure are the similarity between the response and the neutral correlation functions in the sub 0.2ps time domain. The later behavior of the response function $S(t)$, in particular the long time decay, is more like the behavior of the charged solute's $C(t)$. It appears that the linear response

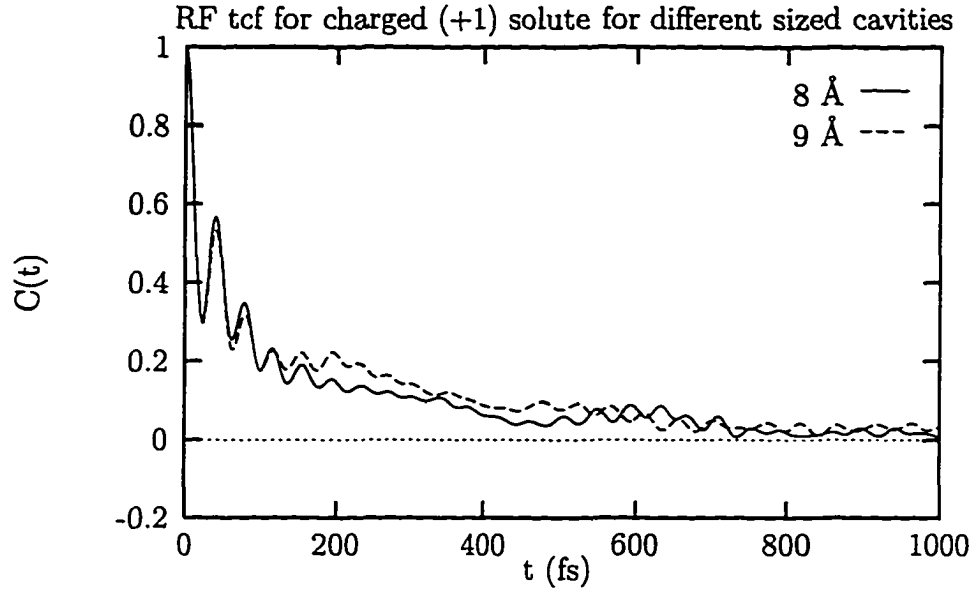

Figure 6.14: $C(t)$ for positively charged solute calculated with the reaction field formalism

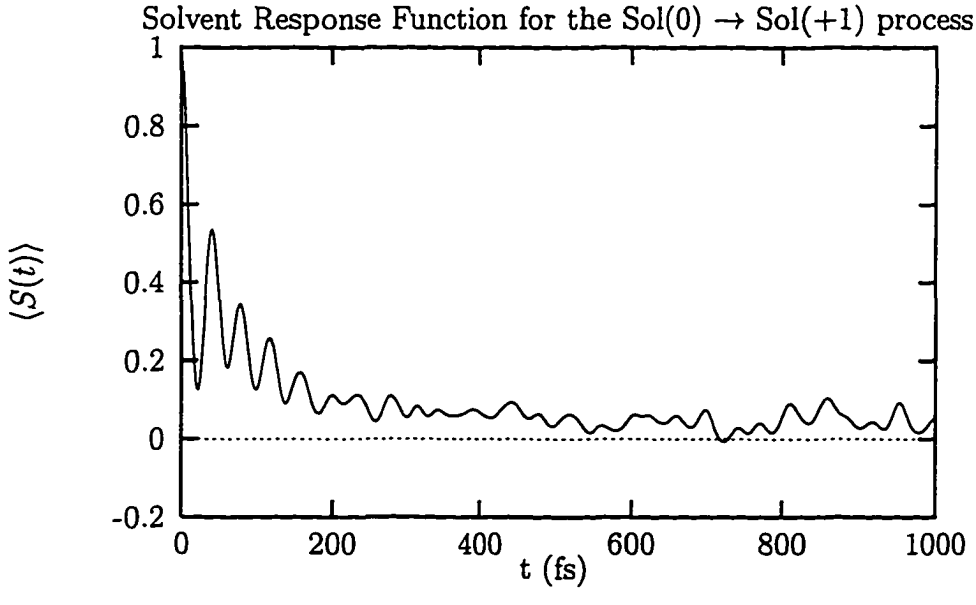

Figure 6.15: Solvent Response function calculated directly from a nonequilibrium simulation

approximation that allows for the use of $C(t)$ to estimate $S(t)$ is a reasonable one.

6.6 Comparison of RF Results with Other results

The results presented in the previous sections are discussed here through comparisons with results obtained by the use of the same solute and solvent models but with different formalisms. In particular, solvational results obtained through PBC and pure cluster (no reaction field) formalisms are next compared with the reaction field results.

First, in Figure 6.16 the *tcfs*, $C(t)$, are shown for a 9 Å cavity neutral solute simulation confined using the L-J confining potential with and without the dielectric continuum surrounding the cavity. All other parameters, such as the 'LJ confinement' potential, are same for the two curves shown in Figure 6.16.

In Figure 6.16 the importance of the molecular nature of the solvent and the degree to which this molecular nature dominates the total relaxation of the solvent is shown. The surrounding continuum is, therefore, only a small perturbation to the overall solvent dynamics. This result also indicates that truncating the Taylor's approximation in equation 6.6 after the first term is expected to have only a miniscule effect on the dynamics while making the computation much less expensive. It is also, therefore, quite possible that a large cluster of molecules may well simulate the total solvent without the use of the continuum. It is also clear that for the cluster size used here, disregarding the reaction field slightly but systematically decreases the $C(t)$ *tcf*. It appears that with the neglect of the RF the dominant, faster, "inertial" component of the *tcf* is exaggerated somewhat at the expense of the slower "diffusive" component. In Figure 6.16 it is seen that the molecular interaction between the solvent and the solute that governs, to an almost overwhelming degree, the solvent-solute interaction and the resulting solvent dynamics.

Next, in Figure 6.17 the solvation results using the RF formalism are compared and constrasted with results obtained from simulations using the PBC formalism. *tcfs* from the two formalisms for neutral and charged solutes are presented.

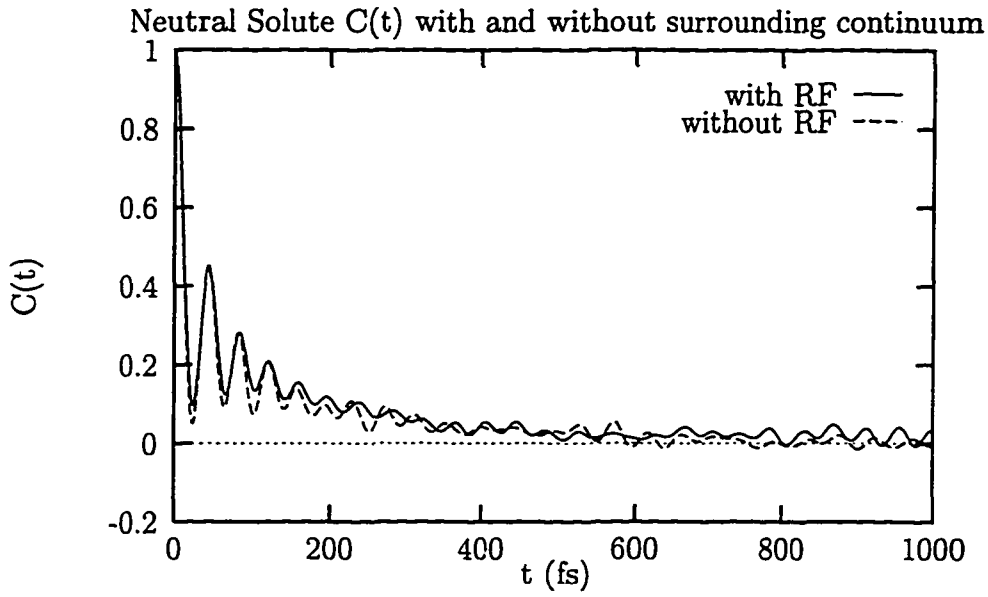

Figure 6.16: Impact of the Reaction Field on the neutral solute *tcf*

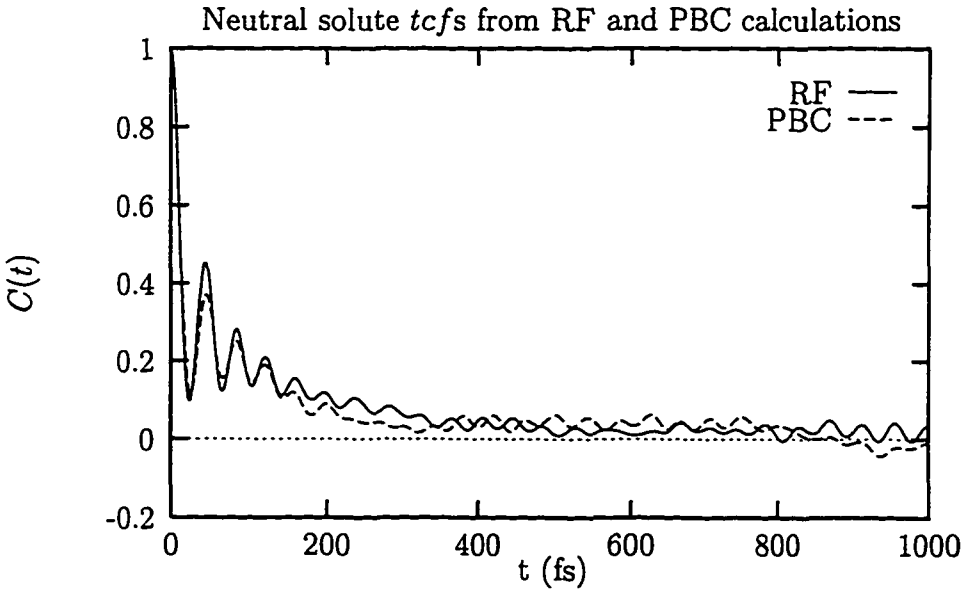

Figure 6.17: Neutral solute *tcf*s calculated using the RF and the PBC formalisms

In this figure the $C(t)$ *tcfs* for a neutral solute are compared for the RF and the PBC calculations. The oscillations for the *tcfs* are very well correlated and overall the two curves are similar. The oscillations in the PBC curve appear to be damped to a slightly greater extent than the RF curve. These oscillations are caused by the "collective librational"[11] (rotational) motion of the closest solvation shells around the solute. For the RF calculations, the solute is confined to stay at the center of the spherical cavity while there is no such constraint on the PBC solute. We speculate that this constraint may assist in the formation of the solvation shells around the RF solute leading to a greater contribution from the rotational motion of the surrounding solvation shells. A freely moving solute would be preferable to a fixed one because the latter is physically artificial. However, a moving solute may spend a considerable amount of time near the surface of the cavity at which time it would not surrounded by molecular solvent. The solvational quantities, in that case, are no longer of a solute surrounded by molecular solvent that in turn is surrounded by a dielectric continuum. We have shown that the molecular nature of the solvent is critical to a correct description of solvent dynamics and a freely moving solute is not always surrounded by molecular solvent particles. The analysis of the solvent dynamics for a moving solute in a limited sized cavity is not transparent.

In Figure 6.18 the $C(t)$ *tcfs* for a charged solute are compared for the RF and the PBC systems. The two curves are rather similar for $t > 0.2$ps, but there is a systematic difference between them for $t < 0.2$ps. This difference is quite intriguing, since it is with charged solutes that the PBC formalism is most suspect. It is possible that the fixed solute at the center of the cavity in the RF formalism assists in the formation of the solvational shells and, therefore, exaggerates the the rotational oscillatory decay of the *tcf*. On the other hand, the PBC formalism (for 256 solvent and 1 solute molecule in a *ca.* 20 Å on a side cubic box) may treat the solvent molecules erroneously near the cell edge due to the unphysical change in the polarization at the cell edge. This difference in the two curves shown above is important and a closer look at the causes of this discrepancy may yield useful clues about the limitation of either of the two formalisms in treating solvent dynamics.

6.7 Conclusion

In this thesis, a reaction field formulation of solvent dynamics with a cluster of solvent molecules and a solute molecule in a cavity confined by a L-J wall is presented. The structure of the solute-solvent system was probed as a function of the cavity size and solute charge. We have shown that using a 9 Å sized cavity that contained about 110 water molecules, the structural and solvational results are nearly independent of cavity size. A careful placement of the LJ confining wall allows for a correct structural description of the system. The importance of the molecular nature of the solvent to the solvent dynamics was demonstrated in a comparison of solvent dynamics of particles in a cavity with and without the dielectric continuum.

This formalism should make the determination of solvent-dynamical properties for a variety of solvent-solute systems computationally easier and conceptually simpler. Incorporation of the complete dielectric response function, $\epsilon(\omega)$, for the solvent studied in the MD equations should improve the accuracy of the results. The difference in the time-correlation functions for the charged solute between the PBC and the RF formalisms has to be further studied to determine whether the difference is accidental or systematic. A careful study of this difference may yield useful clues about the limitations of the PBC simulations for charged systems with polar solvents.

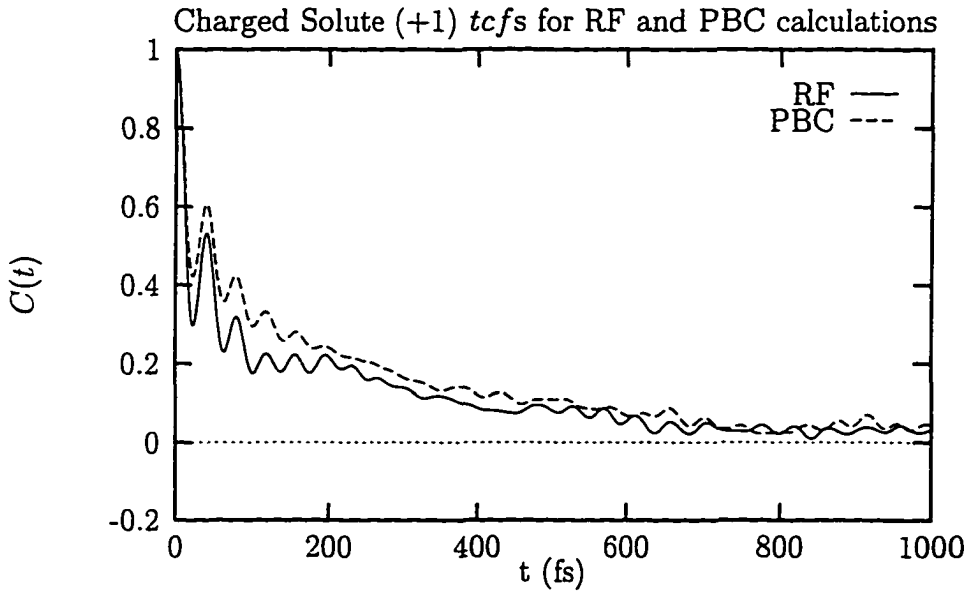

Figure 6.18: Charged solute $tcfs$ calculated using the RF and the PBC formalisms

Bibliography

[1] Wallqvist, A. *Molecular Simulation* **1993**, *10*, 13.

[2] Wang, L.; Hermans, J. *J. Phys. Chem.* **1995**, *99*, 12001.

[3] Lee, F. S.; Warshel, A. *J. Chem. Phys.* **1992**, *97*, 3100.

[4] Shang, H. S.; Head-Gordon, T. *J. Am. Chem. Soc.* **1994**, *116*, 1528.

[5] Tironi, I. G.; Sperb, R.; Smith, P. E.; van Gunsteren, W. F. *J. Chem. Phys.* **1995**, *102*, 5451.

[6] Jackson, J. D. *Classical Electrodynamics* (Wiley, New York, 1975).

[7] Kirkwood, J. G., *J. Chem. Phys.* **1934**, *2*, 351.

[8] Press, W. H.; Teukolsky, S. A.; Vetterling, W. T.; Flannery, B. P. *Numerical Recipes in C, 2nd Ed.* (Cambridge University Press, 1992).

[9] Friedman, H. L. *Mol. Phys.* **1975**, *29*, 1533.

[10] Arfken, G. B. *Mathematical Methods for Physicists, 4th Ed.* (Academic Press, San Diego, 1995).

[11] a) Maroncelli, M.; Fleming, G. R. *J. Chem. Phys.* **1988**, *89*, 5044; b) Maroncelli, M. *J. Chem. Phys.* **1991**, *94*, 2084.

[12] Mason, G. *Nature* **1968**, *217*, 733.

[13] Carter, E. A.; Hynes, J. T *J. Chem. Phys.* **1991**, *94*, 5961.

[14] Jimenez, R.; Fleming, G. R.; Kumar, P. V.; Maroncelli, M. *Nature* **1994**, *369*, 471.

[15] Marcus, R. A.; Sutin, N. *Biochim. Biophys. Acta* **1985**, *811*, 265-322.